Investigating the Scalability of Quantum Repeater Protocols Based on Atomic Ensembles

David Maier

MASTER THESIS

Faculty of Physics
at Ludwig-Maximilians-Universität
Munich
and
QuTech, Delft

submitted by

David Maier

Munich, 11.03.2020

Supervisor:
Prof. Dr. Belén Paredes (LMU),
Prof. Dr. Stephanie Wehner (QuTech)

Untersuchung der Skalierbarkeit von Quantum Repeater Protokollen basierend auf Atomensembles

David Maier

MASTERARBEIT

Fakultät für Physik
an der Ludwig-Maximilians-Universität
München
und
QuTech, Delft

vorgelegt von

David Maier

München, 11.03.2020

Betreuer:
Prof. Dr. Belén Paredes (LMU),
Prof. Dr. Stephanie Wehner (QuTech)

Abstract

A Quantum Internet will enable new applications that are provably impossible with classical communication alone. However, the optical fibers used to carry the quantum information are inherently lossy. To overcome the exponential losses over distance so-called quantum repeaters are needed to amplify the signal.

In this thesis we investigate the performance of different repeater architectures within the European Quantum Internet Alliance which are based on atomic ensemble technology. For each of the groups from Barcelona, Delft, Geneva and Paris we simulate different sets of current and future performance parameters.

In contrast to previous simulations and analytical models we present the first simulation that includes important sources of error for these types of architectures, such as multi-pair emission, time-dependent memory efficiency and photon distinguishability. Key to this is our new approach using discrete event simulation never used before for atomic ensemble based quantum repeater protocols.

We find that previous models do not accurately describe the performance of such repeater architectures and provide an analysis of how each of these noise parameters impacts performance. This allows us to assess the potential of different component technologies, such as photon sources and quantum memories, and quantify what improvements are necessary to bridge long distances in the future.

With our simulation we provide a crucial stepping stone towards a blueprint for a pan-European Quantum Internet.

Acknowledgments

This thesis is the product of a whole year of research and would not have been possible without the invaluable contributions of the many wonderful people surrounding me.

First and foremost I would like to express my deepest gratitude to my supervisors Prof. Stephanie Wehner and Prof. Belén Paredes for giving me the amazing and unique opportunity to perform my project outside of my home university at QuTech. Both of you are brilliant scientists, have inspired me deeply and given me the motivation to pursue my future in quantum information research.

Secondly I would like to thank my daily supervisors Filip and Guus. You helped me take my first steps in the field of quantum communications and always had an open ear for my countless questions. Your great feedback and advice helped shape me from a physics student to an independent researcher.

Next I would like to highlight the great cooperation with my fellow master student Julian who was on the quest to simulate atomic ensembles with me from the start. Our great discussions and code-reviews solved countless bugs and made writing the code behind this thesis really enjoyable.

Further I would like to express my appreciation of all my fellow office mates in B205 Axel, Tim and Francisco. You made the time inside and outside the office a real joy and always had an open ear for my problems. This of course also extends to the rest of the group who have been most welcoming, warm and kind people.

I would also like to thank all the other members of the Blueprint team Ariana , Loek, Rob and Walter for helping me with all my various programming issues. From buggy print statements to crashing the Supercomputer no problem was to stupid or to difficult to solve for you. Without your help I would no doubt have been much closer to total frustration and insanity. I deeply appreciate the many hours you invested in fixing my problems.

Next I would like to thank Helena for just being the most wonderful person and making all the formalities surrounding my project an absolute breeze.

I want to also thank the American Physics Society for giving me the opportunity to finish my thesis in the scenic landscapes of the Rocky Mountains by last-minute canceling the March Meeting and getting me stuck in Colorado for a week.

Finally I would like to express my deepest gratitude to my lovely parents who always support me whatever I do, even though that might not always be easy.

Contents

Chapter 1

Introduction

Recent advances in Quantum Information Technology such as Google's quantum supremacy experiment [1] have drawn large public attention to this particular field of Quantum Physics. The enormous advancements in the ability to detect and manipulate single quantum objects has led the European Union to announce that a "Second Quantum Revolution is unfolding" and invest one billion Euro in the Quantum Flagship Project [2] as part of Horizon 2020 [3].

While the whole world is talking about quantum computers, there is one very unique project within the Quantum Flagship called the **Quantum Internet Alliance (QIA)** [4]. Its goal is to *develop a Blueprint for a pan-European entanglement-based* **Quantum Internet***, by developing, integrating and demonstrating all the functional hardware and software subsystems* [5]. Such a Quantum Internet will use fundamentally quantum mechanical properties such as **entanglement** and **superposition** to allow for features that are impossible using the current classical Internet. It would thus act as a supplement to the classical Internet enabling e.g. provably secure communication using Quantum Key Distribution (QKD) [6], secure access to remote quantum computers (blind quantum computing) [7], extension of telescope baselines [8] or a global 4-dimensional quantum positioning system [9].

Central to all of the applications is sharing an entangled state between end nodes over long distances. Similar to the classical Internet, to overcome the exponential losses over distance the signal needs to be amplified. However, quantum information can not be copied [10], [11] and therefore our usual approaches for signal amplification do not work here. We have to employ a more sophisticated method called **Quantum Repeaters** [12]. There are many experimental efforts going on around the world trying to improve the hardware used for such a device but in order to develop the blueprint for a Quantum Internet mentioned above a significant amount of theoretical analysis will be required to guide those experimental efforts.

As a first stepping stone towards the QIA goal, a team of scientists with various backgrounds under the direction of Prof. Wehner is working on simulating a Quantum Internet for the Netherlands. **Simulation** allows us to effectively study the behavior of different classes of repeater protocols under various parameters. This will enable us to define further design and research goals and to develop a realistic blueprint for a large scale Quantum Internet. It also makes a wide variety of other applications possible, such as analyzing future networking protocols [13], parameter optimization, comparing different hard- or software components and analyzing the scalability of various proposals. To permit this the simulation model however needs to be as realistic as possible. The knowledge that will be gathered from this smaller scale analysis will provide invaluable input for any larger scale quantum network.

One particular class of repeater protocols is based on using **Atomic Ensembles** and

linear optics [14]. This approach utilizes the collective effects of atoms in ensembles to reliably generate and distribute entanglement between end nodes. The greatest advantage over other protocols comes from their ability to use multiple photon modes in parallel to greatly improve the rate of entanglement distribution. They therefore offer great promise for future application [15] and are under active experimental development within QIA.

In this thesis we provide two major contributions:

- We **develop a more realistic and highly modular simulation of atomic ensemble based quantum repeater architectures.** By including various noise parameters that are analytically hard to investigate such as multi-photon emission, time-dependent memory noise or photon distinguishability we offer a model that allows for analysis beyond any currently existing models.

- We **compare current experimental efforts within QIA to realize atomic ensemble based quantum repeaters**, demonstrating the capabilities of our simulations to assess the scalability of different repeater protocols. The modularity, efficiency and scalability of our simulation makes it possible to simulate many different hardware components in large quantum network topologies. Thus we compare the repeater protocols developed in Barcelona, Delft, Geneva and Paris in a simulated QKD experiment.

To approach these tasks this work starts out by introducing the basic background knowledge and building blocks of quantum repeaters in Chapter 2. After introducing the more theoretical aspects the chapter will close with a current proposal of a real physical implementation of a repeater protocol including a discussion of the necessary devices.
In Chapter 3 we will first give a basic introduction in the functionality of the components we had to design for our simulation. Then we go into a detailed discussion of how we implemented multi-photon emission, which was especially challenging.
Once we have elaborated our model we will then verify it against various existing analytical and numerical models in Chapter 4 to convince ourselves of its validity.
In the following Chapter 5 we will then move beyond previously existing models and investigate the effects of various more sophisticated noise parameters. Key to this analysis is the simulation we developed especially for atomic ensembles.
We then demonstrate the capabilities of our model by comparing the four different experimental efforts to realize atomic ensemble based repeaters within QIA in Chapter 6. This is enabled by our simulation's focus on keeping things modular, thus making it easy to compare different component technologies.
Finally we will give an idea of how our model can be used to optimize real experiments in Chapter 7. To conclude we will propose future research topics in Chapter 8.

Chapter 2

Background

2.1 Introduction

To be able to understand and appreciate the work presented in this thesis it is necessary to give some theoretical background information. In this chapter we will approach this in a step-by-step manner. We will start by introducing the fundamental problem of quantum communication thus motivating and explaining the concept of quantum repeaters. Then we will go over necessary requirements for a quantum repeater architecture to then introduce atomic ensembles and show how they can meet all of those requirements. The result is the most fundamental atomic ensemble based repeater protocol. From there we will compare various improved protocols to then identify the crucial concept of multiplexing. We introduce various forms of multiplexing and finally arrive at a current implementation of quantum repeaters using real and imperfect components. We finish the theoretical discussion by a detailed description of those components to explain the main sources of noise they introduce.

2.2 Quantum Repeaters

The very definition of the purpose of a Quantum Internet is the ability to distribute a quantum state over a long distance. In order to do this, the state needs to be sent through a quantum channel such as optical fibers or free space. Currently the only feasible candidate to carry such a state are photons.
The distance over which any information can be sent over a channel is limited by loss and in the case of quantum information also decoherence. In practice however, the most dominant problem is photon loss which (just like decoherence) scales exponentially with distance L. This is reflected by the probability of transmitting a photon, the so called **transmittance** τ which scales with length L as

$$\tau(L) = \tau(0) \times 10^{-\alpha L/10}, \tag{2.1}$$

where α is the so called **attenuation**, which is the parameter characterizing the loss of a channel. The same scaling holds for other figures of merit as for example the **rate** or the **fidelity**, which characterizes how close to a target state the end-to-end transmitted state is. For typical optical fibers used for telecommunication α is roughly 0.2 dB/km in the optimal wavelength range around $1.5\mu m$. While this is impressively low for short distances (95% transmission over a distance of 1 km) it quickly becomes very significant when looking at distances relevant for a large scale quantum network [15]. As an example we can insert some more distances in eq. (2.1): For a distance of 500km the rate gets damped by a factor of 10^{10} and for 1000km even by 10^{20}. That would dampen a 10 GHz source (equal to 10 Billion photons per second) down to a rate of just 10^{-10} Hz (corresponding to roughly 1

photon every 300 years).
As the distances in telecommunication networks are typically of the order of hundreds or thousands of kilometers, the signal therefore needs to be boosted somehow.
In classical telecommunication this can simply be done by inserting amplifiers at certain intermediate distances, but unfortunately this is impossible for quantum communication due to the **no-cloning theorem** [10], [11]. It was discovered already in the 1980s and states that noiseless amplification of a quantum state is impossible for non-orthogonal states.
The theorem is fairly quick to proof (see box below), but feel free to skip this box and continue reading.

Proof: No-Cloning theorem
Say we have an unknown quantum state $|\phi\rangle$ that we wish to copy and a second pure state $|s\rangle$. Now we would like to have some unitary U that copies $|\phi\rangle$ onto $|s\rangle$, i.e.

$$U_{copy}(|\phi\rangle \otimes |s\rangle) = |\phi\rangle \otimes |\phi\rangle \,. \tag{2.2}$$

Suppose this copying procedure works for any state, specifically also for two different states $|a\rangle$ and $|b\rangle$, then

$$U_{copy}(|a\rangle \otimes |s\rangle) = |a\rangle \otimes |a\rangle \tag{2.3}$$
$$U_{copy}(|b\rangle \otimes |s\rangle) = |b\rangle \otimes |b\rangle \,. \tag{2.4}$$

If we now take the inner product of the two equations above we get

$$\langle a|b\rangle = \langle a|b\rangle^2 \,. \tag{2.5}$$

It is obvious that $x = x^2$ only has two solutions $x \in \{0, 1\}$. This means $|a\rangle$ and $|b\rangle$ are either equal or orthogonal. Therefore, any cloning device can only clone states which are orthogonal to one another. If one allows for mixed-states or a non-unitary cloning device the same statement holds unless one also allows for a finite loss of fidelity in the copied state, which would defy the purpose of amplification [16]. Since the advantage of quantum protocols comes precisely from the existence of non-orthogonal states one needs to come up with a more sophisticated method of distributing quantum information over long distances [15].

The solution to this fundamental problem of quantum communication was proposed by Briegel et al. in 1998 where they introduce intermediate connection points [12], which are now know as **quantum repeaters**.

At this point it is crucial to mention that quantum states have a property known as **entanglement**, which is of fundamental importance to entanglement-based quantum networks. It is a profoundly non-classical, counter-intuitive property which lies at the heart of quantum non-locality [17]. To understand the approach proposed in [12] one needs to know that entanglement can be "swapped" [18].

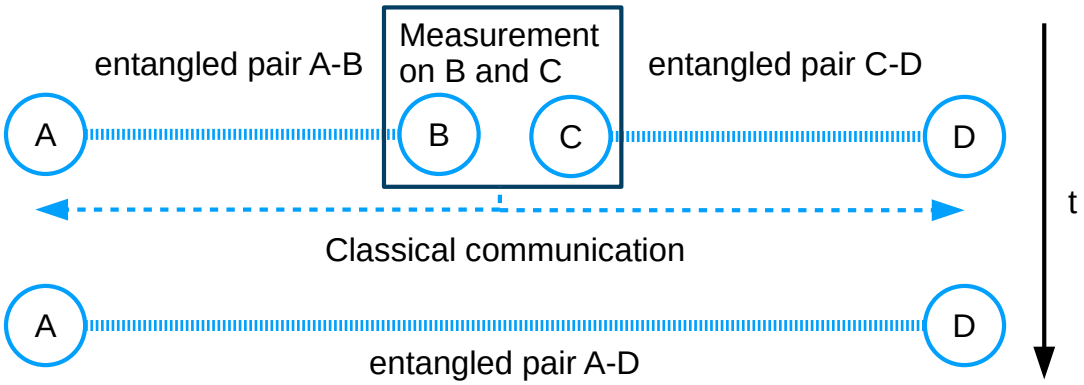

Figure 2.1: Principle of **Entanglement Swapping** [18]. Given two entangled states, e.g. one between A and B and one between C and D, it is possible to "swap" the entanglement to generate an entangled pair between A and D. This is done by performing a joint measurement on systems B and C in a basis of entangled states, followed by classical communication of the result to the location of systems A and D. This can be used to create remote entanglement between systems that have never directly interacted.

The principle of **entanglement swapping** is explained in Fig. 2.1. The measurement performed on $B-C$ is called a **Bell State Measurement (BSM)** as it projects the state of $A-B$ onto a maximally entangled state or **Bell state**. This forms the basis of many interesting applications, such as quantum teleportation [19] and most importantly for this thesis: quantum repeaters. The basic idea brought forward in [12] is to - just as in classical networks - divide the channel into N segments with repeaters at the connection points. A Bell state is then distributed over each of those N segments called **elementary links**. At the connecting repeater nodes one then performs a Bell state measurement and classically communicates the measurement results to adjacent nodes. In this way entanglement is swapped at each intermediate node until the two end nodes share an entangled state, see Fig. 2.2. We will show later that this protocol scales much better than direct transmission for longer distances.

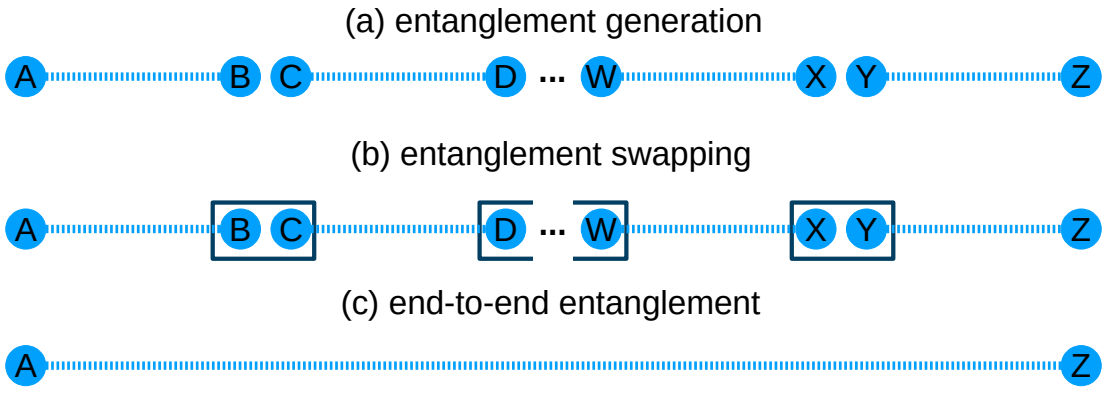

Figure 2.2: Principle of quantum repeaters [15]. To distribute entanglement between two remote locations A and Z over a long distance one first generates entanglement over shorter elementary links, e.g. A-B, C-D, ..., W-X, Y-Z as shown in (a). As detailed in Fig. 2.1 entanglement is then swapped at all the intermediate nodes (b) until nodes A and Z share entanglement (c). The blue circles represent quantum memories, while the dashed connections symbolize entanglement and the dark blue boxes indicate Bell state measurements.

2.3 Requirements for Quantum Repeaters

From the above description of the quantum repeater scheme, we can now identify three core requirements for the protocols we will discuss in this thesis:

1. The ability to **generate heralded entanglement** over the elementary links.
2. The ability to **store created entanglement** long enough to enable swapping.
3. The ability to **perform the swap** operation.

In the following we will explain these three in detail and then in the next section present possible solutions.

The first step detailed in Fig. 2.2 is entanglement creation. We therefore need to be able to create entanglement between two nodes and we want to know when it has been established successfully. This is called **"heralded" entanglement generation** over the elementary links. As the most basic approach one might suggest to create an entangled pair of photons locally and then send one of the photons to the other node in the link. This would indeed be a possibility, but it comes with two major drawbacks: In a realistic repeater protocol, the elementary links still have lengths of the order of a hundred kilometers [15], corresponding to a transmission of order 10^{-2}, see Eq. (2.1). Additionally, to herald the success one would need to be able to detect the arrival of the photon without destroying the entanglement, which is difficult to do in practice. In the next chapter we will present a possibility how heralded entanglement can be generated remotely, by sending photons to a middle station, where entanglement will we swapped by a measurement to herald entanglement between the nodes of the elementary link.

The second step detailed in Fig. 2.2 is entanglement swapping. In order to be able to swap the entanglement, one needs to be able to store the entanglement for long enough until the neighboring links have also generated heralded entanglement. Only then can the joint measurement be done and the entanglement swapped. If not all repeater nodes swap at the same time, but the higher-level entanglement is swapped step by step, then the storage requirements are even higher. Therefore, quantum repeater protocols require **quantum memories** [20] which we will discuss in Section 2.8.2.

Finally, to actually execute step (b) in Fig. 2.2 one needs to be able to perform the entanglement swapping operation between the quantum memories. This means that one needs a way to perform a local joint measurement projecting onto entangled states between the two memories. If one has the possibility to perform general quantum gates between the memories, this is easy to do. However, for the sake of feasibility it is worth considering a simpler approach, e.g. measurements which only succeed with certain a probability, as general quantum gates are challenging to realize experimentally. Again the following chapter will present a proposal for a simple solution to this requirement.

For completeness it is necessary to mention that the original proposal [12] also requires **entanglement purification** [21]. This is a process where multiple pairs of lower fidelity with respect to the target Bell state are used to generate a single pair of higher fidelity in order to overcome effects of decoherence on a noisy channel. Since multiple pairs are used to generate a single higher fidelity pair this will decrease the maximum rate. In this work we will focus on simpler protocols which do not require purification, as they are the most realistic candidate for near-term repeater experiments with the goal of outperforming direct transmission [15].

2.4 A simple approach - the DLCZ protocol

With all the requirements for a quantum repeater mapped out, we now proceed to propose a first actual implementation of such a protocol. In doing so we want to explain why

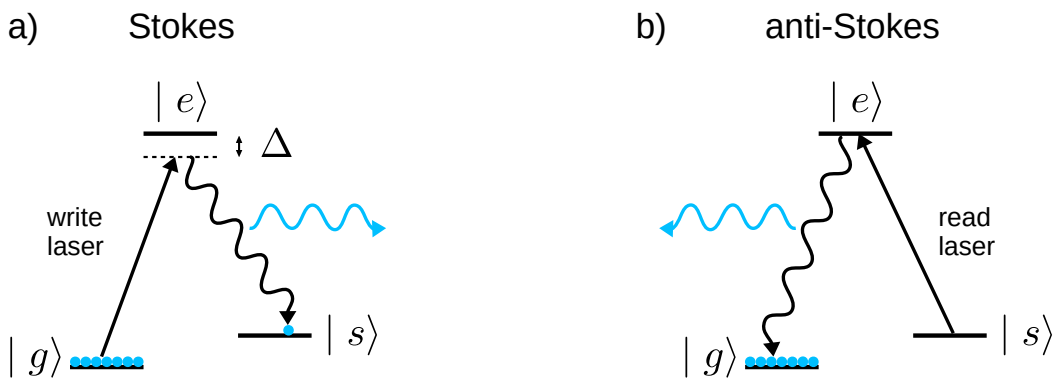

Figure 2.3: Basic energy level scheme of spontaneous Raman emission. $|g\rangle$ denotes the ground state, $|e\rangle$ the excited state and $|s\rangle$ the meta-stable state used to store the atomic excitation. **a) Write process:** When a laser off-resonantly pumps the $e-g$ transition a **Stokes photon** (blue wiggly line) will be emitted on the $e-s$ transition and an atomic excitation (blue dot) stored on $|s\rangle$. Δ denotes the detuning of the laser pulse. **b) Read process:** When a laser pumps the $s-e$ transition any atomic excitation will be converted back to an **anti-Stokes photon** (blue wiggly line) emitted on the $e-g$ transition which will be collectively enhanced [14].

atomic ensembles are a promising candidate for such an architecture and also explain one of the most basic quantum repeater protocols.

In 2001 **D**uan, **L**ukin, **C**irac and **Z**oller published a seminal paper detailing how to meet all of the above requirements using atomic ensembles as quantum memories, now known as the **DLCZ protocol** [14]. All Bell state measurements, both at the midpoint of the elementary links (as we will explain in the following section) and the repeater nodes (as explained above) are done using simple linear optics in combination with photon counting detectors. This makes it a simple approach very much within reach for near-term experiments. The main process the scheme is based on is **spontaneous Raman emission**. In this process a single photon is spontaneously emitted while simultaneously creating a spin-excitation in the atomic ensemble memory entangled to the photon. The resulting repeater protocol will be described in detail in the next sections of this chapter.

Given that spontaneous Raman emission is a probabilistic effect it is easy to see why one would like to use an ensemble instead of a single emitter: The collective effects of the large number of atoms in an ensemble make it much easier to achieve strong and controllable coupling between the emitted photon and the memory.

We will now go through all the requirements of a repeater scheme mentioned before and explain in detail how the DLCZ protocol approaches them.

2.4.1 Heralded Entanglement Generation

The fundamental building block of the DLCZ scheme is an ensemble of N identical atoms with a three-level structure as shown in Fig. 2.3. It contains two metastable ground states $|g\rangle$ and $|s\rangle$, e.g. hyperfine or Zeeman sublevels, and one exited state $|e\rangle$. All atoms in the ensemble are initially prepared in the ground state $|g\rangle$. To emit a photon from the ensemble it is illuminated with a short, off-resonant[1] laser pulse (the write pulse) on the $g-e$ transition. This leads to the spontaneous emission of a Raman photon on the $e-s$ transition. Following the usual terminology of Raman scattering and provided that the energy of $|s\rangle$ is slightly higher than the energy of $|g\rangle$, this will be called the **Stokes photon**.

[1]Resonant excitation would introduce fast inhomogeneous dephasing of the generated spin excitation leading to low read-out efficiency [22].

If one now detects this photon in such a way that no information is revealed about which atom it came from, e.g. by detecting it in the far field, the state of the ensemble is [15]

$$|\psi\rangle_{ensemble} = \frac{1}{\sqrt{N}} \sum_{n=1}^{N} e^{i(\mathbf{k_w}-\mathbf{k_S})\mathbf{x_n}} |g\rangle_1 \cdots |g\rangle_{n-1} |s\rangle_n |g\rangle_{n+1} \cdots |g\rangle_N , \tag{2.6}$$

where $\mathbf{k_w}$ is the $\mathbf{k}$-vector of the write laser, $\mathbf{k_S}$ is the $\mathbf{k}$-vector of the detected Stokes photon and $\mathbf{x_n}$ is the position of the nth atom of the ensemble. This is a coherent superposition of all possible terms with $N-1$ atoms in $|g\rangle$ and one in $|s\rangle$. In practice, the different terms may have varying amplitudes depending on the profile of the laser and the shape of the atomic ensemble. It is clear that in an ensemble of atoms where we have certain probability p_e of emitting a single Stokes photon we will also have the possibility for the same event happening two or more times [15].

We can assign bosonic operators a and s_a to the Stokes photon and the atomic excitation respectively to write the total state of the atomic ensemble and the Stokes mode as

$$|\phi\rangle = |0\rangle_a |0\rangle_s + \sqrt{p_e} a^\dagger s_a^\dagger |0\rangle_a |0\rangle_s + \mathcal{O}(p_e), \tag{2.7}$$

where $|0\rangle_a , |0\rangle_s$ are the ground state of the atomic ensemble and the vacuum state of the Stokes pulse respectively and $p_e < 1$ is the small probability that an atom is excited to $|s\rangle$ and a Stokes photon is emitted. $\mathcal{O}(p_e)$ represents all terms with more than one excitation and therefore probabilities $\leq p_e^2$. The time evolution of such a system can be described by the following Hamiltonian with coupling constant χ [15]

$$H = \chi(a^\dagger s_a^\dagger + a s_a), \tag{2.8}$$

which is formally equivalent to the non-linear process of parametric down-conversion. This equivalence will become important when we introduce more advanced protocols such as the one described in section 2.7 where this equivalence allows us to use the same description. The coupling χ depends on the intensity of the read laser, the number of atoms in the ensemble, the detuning of the laser and the transition strengths of the $g-e$ and $e-s$ transitions.

We now have a way of emitting a photon which is entangled to an atomic excitation in the atomic ensemble, so let's now use this to generate heralded entanglement over an elementary link as shown in Figure 2.4.

Say we have two remote atomic ensembles A and B with both their states described by (2.7), then the total state of A and B is [15]

$$|\phi\rangle = \left(1 + \sqrt{\frac{p_e}{2}}(s_a^\dagger a^\dagger e^{i\phi_a} + s_b^\dagger b^\dagger e^{i\phi_b}) + \mathcal{O}(p_e)\right) |0\rangle , \tag{2.9}$$

where a/b, s_a/s_b and ϕ_a/ϕ_b are the bosonic operators of the Stokes photon and the atomic ensemble and the phases of the pump lasers of locations A and B respectively.

The Stokes photons from both sides are now coupled into optical fibers and sent to a central detection station containing a beam splitter and two photon counting detectors d and $\tilde{d}$. Detection of a single photon in d or $\tilde{d}$ projects the state of the two ensembles onto [15]

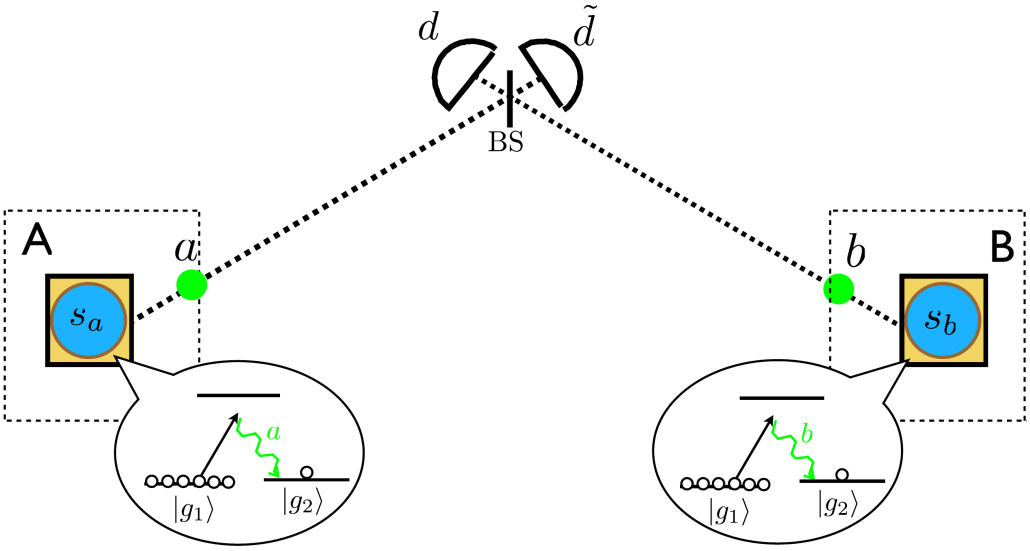

Figure 2.4: Heralded entanglement generation between two atomic ensembles at A and B within the DLCZ protocol. DLCZ-type atomic ensembles (blue circles) can probabilistically emit Stokes photons (green dots) entangled to atomic excitations within the ensemble (see (2.7)). These photons are then coupled into optical fibers (dotted black lines) and sent to a central station consisting of a beam splitter (vertical bar, BS) and two photon counting detectors (semi-circles) d and $\tilde{d}$. Detection of of a single Stoked photon that could have come from either A or B, heralds the storage of a single atomic excitation [15].

$$
\begin{aligned}
|\psi_d\rangle_{AB} &= \frac{1}{\sqrt{2}}(s_a^\dagger e^{i(\phi_a+\xi_a)} + s_b^\dagger e^{i(\phi_b+\xi_b)})\,|0\rangle_{AB} \\
&= \frac{1}{\sqrt{2}}(|10\rangle_{AB} + |01\rangle_{AB}\, e^{i\theta_{AB}}) \qquad (2.10) \\
|\psi_{\tilde{d}}\rangle_{AB} &= \frac{1}{\sqrt{2}}(s_a^\dagger e^{i(\phi_a+\xi_a)} - s_b^\dagger e^{i(\phi_b+\xi_b)})\,|0\rangle_{AB} \\
&= \frac{1}{\sqrt{2}}(|10\rangle_{AB} - |01\rangle_{AB}\, e^{i\theta_{AB}}), \qquad (2.11)
\end{aligned}
$$

where ξ_a/ξ_b is the phase a photon picks up on its way to the central station from A/B respectively and we defined $\theta_{AB} \equiv \phi_b - \phi_a + \xi_b - \xi_a$. We see that both these states are entangled states of a single atomic excitation delocalized between A and B. Therefore a single click on either detector heralds entanglement between the two remote atomic ensembles.
Note that this too can be seen as a form of entanglement swapping:
We started out with two entangled pairs of Stokes-photon and atomic excitation. The single-photon detection at the midpoint is a Bell state measurement projecting the photonic modes on one of two maximally entangled states, thereby creating heralded entanglement between the two atomic ensembles [15].

2.4.2 Entanglement Storage and Swap

The next requirement for a quantum repeater is the ability to store entanglement long enough to enable a swap operation between neighboring elementary links. Improving storage times is the object of active research, however current experimental setups already report storage times for atomic excitations which are long enough to enable swapping [23], [24].

So we will quickly move on to the third requirement, namely being able to perform the swap operation. We will now go into detail how an atomic excitation in a three-level system as described in 2.3 can fulfill this requirement as well.

What makes the DLCZ approach a very interesting candidate for a quantum repeater setup is the fact that the atomic excitation can be read out very efficiently. This can be achieved by illuminating the ensemble with a resonant laser pulse on the $s-e$ transition leading to the emission of a single photon propagating in a well-defined direction, thanks to collective interference [14]. The ensemble will then be in a state analogous to (2.6) with $N-1$ atoms in $|g\rangle$, one delocalized excitation in $|e\rangle$ and an additional phase $e^{i\mathbf{k_r}\mathbf{x'_n}}$, where $\mathbf{k_r}$ is the $\mathbf{k}$-vector of the read out laser and $\mathbf{x'_n}$ is the position of the nth atom at the time of the readout. All terms of such a state can decay to the initial ground state $|0\rangle_a = |g\rangle^{\otimes N}$ while emitting a photon on the $e-g$ transition. Again following the standard nomenclature of Raman scattering this would be the **anti-Stokes** photon.
The total amplitude for this process is then proportional to

$$\sum_{n=1}^{N} e^{i(\mathbf{k_w}-\mathbf{k_S})\mathbf{x_n}} e^{i(\mathbf{k_r}-\mathbf{k_{AS}})\mathbf{x'_n}}, \tag{2.12}$$

where $\mathbf{k_{AS}}$ is the $\mathbf{k}$-vector of the anti-Stokes photon. To achieve constructive interference of all N terms we can differentiate between two cases:

1. **Case 1**: $\mathbf{x_n} = \mathbf{x'_n}$, atoms are at rest.
   Constructive interference for $\mathbf{k_w} + \mathbf{k_r} = \mathbf{k_S} + \mathbf{k_{AS}}$ leads to a very large probability amplitude of emitting an anti-Stokes photon along $\mathbf{k_{AS}} = \mathbf{k_w} + \mathbf{k_r} - \mathbf{k_S}$.

2. **Case 2**: $\mathbf{x_n} \neq \mathbf{x'_n}$, atoms are moving.
   Constructive interference only for $\mathbf{k_w} = \mathbf{k_S}$ and $\mathbf{k_r} = \mathbf{k_{AS}}$. For all other configurations the motion of the atoms will cause a dephasing that ultimately limits the storage time [15].

The strong emission into one direction caused by Case 1 allows for a very efficient collection of the anti-Stokes photon. Note that the collective interference is specific to the anti-Stokes photon as for the Stokes photon all the terms in (2.6) correspond to orthogonal final states and therefore full which-way information is stored in the atomic ensemble, making interference impossible [15].

Fig. 2.5 shows the procedure used to swap entanglement in the DLCZ protocol. We start out with two elementary links (see Fig. 2.4) AB and CD where the two atomic ensembles in each link are in a state $\left|\psi_{d/\tilde{d}}\right\rangle_{NM}$ as described in (2.10). The total state of the two links is therefore

$$|\psi\rangle_{ABCD} = \left|\psi_{d/\tilde{d}}\right\rangle_{AB} \otimes \left|\psi_{d/\tilde{d}}\right\rangle_{CD}. \tag{2.13}$$

To swap the entanglement the two atomic ensembles at B and C are now read out as described above by illuminating them with a strong resonant laser pulse. Any atomic excitation in B or C will thus be emitted very efficiently, thanks to the collective interference, as an anti-Stokes photon in a well-defined mode.

Just like at the midpoint of the elementary link, the two photonic modes b' and c' will then be combined at a beam splitter. Once again detection of a single photon on one of the detectors will herald success and the ensembles A and D will now be projected onto the state

$$\begin{aligned}\left|\psi_{d/\tilde{d}}\right\rangle_{AD} &= \frac{1}{\sqrt{2}}(s_a^\dagger \pm s_d^\dagger e^{i(\theta_{AB}+\theta_{CD})})\,|0\rangle_{AD} \\ &= \frac{1}{\sqrt{2}}(|10\rangle \pm |01\rangle\, e^{i(\theta_{AB}+\theta_{CD})})_{AD}.\end{aligned} \tag{2.14}$$

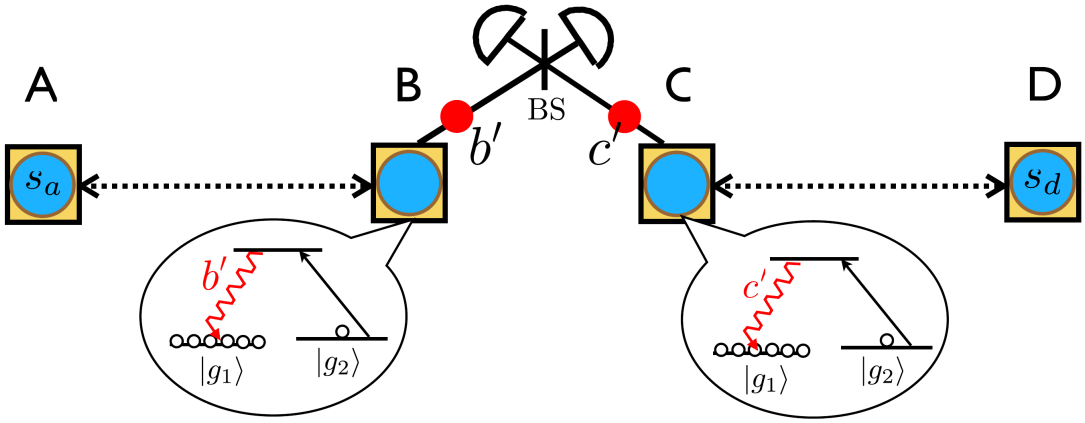

Figure 2.5: Entanglement swapping between two elementary links AB and CD both sharing an entangled state (2.10). The quantum memories (blue circles) B and C are read out with a laser pulse and the emitted anti-Stokes photons are combined at a beam splitter (BS). Detection of a single photon on the detectors (semi-circles) heralds a successful entanglement swap to create an entangled state (2.10) between A and D [15].

By successfully executing such a swap operation at every repeater node along a chain it is possible to connect two remote ensembles over long distances. It is worth noting at this point that the linear optical Bell state measurements proposed in the DLCZ protocol are probabilistic. While a complete BSM allows projecting any two-photon state deterministically onto the set of four Bell-states, it has been shown, that a complete BSM is impossible when using linear optics and no auxiliary photons. The maximum success probability of the linear optical BSM used here is $p_{succ} \leq 50\%$ [25].
This probability is further reduced when we also consider imperfections in the setup. Let us therefore now investigate the effects of an imperfect memory with a probability $\eta_m \neq 1$ of converting an atomic excitation into an anti-Stokes photon and imperfect detectors with a probability of $\eta_d \neq 1$ of detecting a photon that enters the detector. Both of these inefficiencies allow for the case where there is an atomic excitation at both B and C but only one photon is detected behind the beam splitter.

This can either happen if both excitations where read out correctly and only one was detected because of an imperfect detector or one of the two excitations was not read out and the only emitted anti-Stokes photon was correctly detected. The state of AD after the BSM now contains a vacuum component, since we heralded a successful measurement while there is actually no atomic excitation in A or D as described by (2.10). Their density matrix is thus

$$\rho_{AD} = \alpha \left|\psi_{d/\tilde{d}}\right\rangle\!\!\left\langle\psi_{d/\tilde{d}}\right|_{AB} + \beta \left|0\right\rangle\!\!\left\langle 0\right|_{AD}, \tag{2.15}$$

where $\alpha = 1/(2-\eta)$, $\beta = (1-\eta)/(2-\eta)$ and $\eta \equiv \eta_d \eta_m$. It is now possible to show that the relative weight of the vacuum component scales as

$$\frac{\beta}{\alpha} = (1-\eta)(n-1), \tag{2.16}$$

so linearly with the number of elementary links n in the repeater chain [15]. This severely limits the performance of the DLCZ protocol. One way of keeping this vacuum component constant is switching to two-photon interference BSMs as will be discussed in section 2.7.

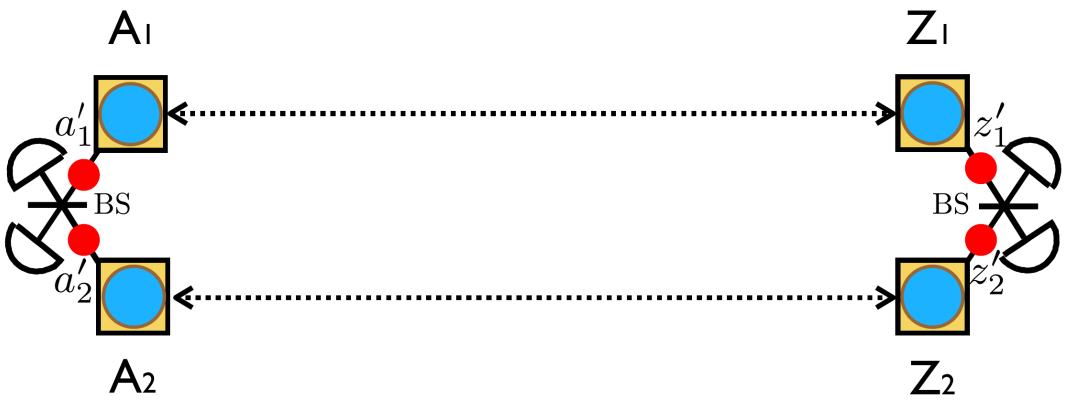

Figure 2.6: Postselection of two-photon entanglement in the DLCZ scheme. Entanglement between the end nodes A and Z is independently created within two repeater chains 1 and 2 such that A_1Z_1 and A_2Z_2 each share a state of the form (2.14). At each location the atomic excitations are read out and the emitted anti-Stokes photons (red) are combined at a beam splitter an then counted at the detectors (semi circles). Measurements in arbitrary basis can be done by adjusting the transmission coefficient and phase of the beam splitter at both locations [15].

2.4.3 Postselection

Before we take a look at the performance of the DLCZ protocol in the next section, we need to investigate one last step in the protocol: postselection.

Once we have established remote entanglement between two end nodes in a state of the form (2.14), one might point out that a single delocalized excitation is of limited use of its own, since it it difficult to perform measurements in any basis other than the Fock basis $\{|0\rangle, |1\rangle\}$. We therefore need a second entangled pair between the two end-nodes to combine the two states into more directly useful two-photon entanglement given by

$$|\phi\rangle_{AZ} = \frac{1}{2}(a_1^\dagger + e^{i\theta_1} z_1^\dagger)(a_2^\dagger + e^{i\theta_2} z_2^\dagger)\,|0\rangle_{AZ}\,. \tag{2.17}$$

This can be achieved with a setup as shown in Fig. 2.6, where we have two atomic ensembles at each location. One then projects onto the subspace with one excitation/photon in each location A, Z by reading out the ensembles and counting the number of photons in each location. The projection of the end-to-end state onto this subspace is

$$\begin{aligned} |\phi\rangle_{AZ} &= \frac{1}{\sqrt{2}}(a_1'^\dagger z_2'^\dagger + e^{i(\theta_2-\theta_1)} a_2'^\dagger z_1'^\dagger)\,|0\rangle_{AZ} \\ &= \frac{1}{\sqrt{2}}(|10,01\rangle + e^{i(\theta_2-\theta_1)}\,|01,10\rangle). \end{aligned} \tag{2.18}$$

In the second line we used the notation $|a_1a_2, z_1z_2\rangle$, where a_i, z_i denotes the number of anti-Stokes photons in that mode, to highlight the analogy of the state to conventional polarization or time-bin entangled states.
Measurement in arbitrary basis are possible by once again combining the two photonic modes on a beam splitter with appropriate transmission coefficient and phase and then detecting a single photon at one of the detectors as shown in Fig. 2.6.

2.4.4 Separation of Source and Memory

A DLCZ like ensemble as described in the previous sections can be emulated by a setup of a quantum memory dedicated solely to storing the photon and a photon pair source

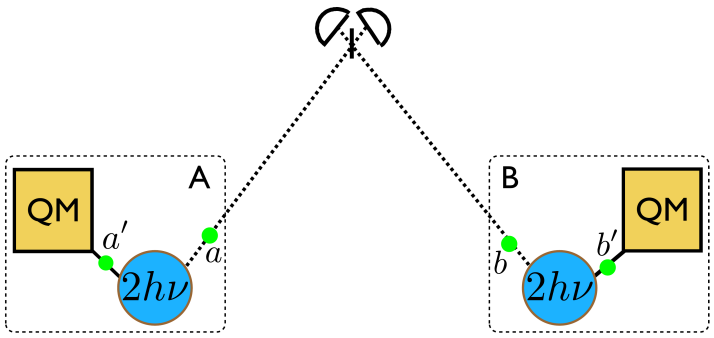

Figure 2.7: Separation of entanglement storage and creation using absorptive quantum memories (yellow squares) and photon-pair sources (blue) emitting pairs of entangled photons i, i'. The primed modes are stored in adjacent memories, while the non-primed modes are sent to the central measurement station. Detection of a single photon in one of the output modes heralds successful entanglement between the quantum memories [15].

dedicated to emitting entangled photon pairs.
This separation comes with two major advantages. Firstly, it supplies greater flexibility for the allowed wavelength of the quantum memory. While the original DLCZ protocol requires the Stokes photon to be emitted in telecom wavelength, when the memory and the source are separated the source can emit a pair of entangled photons with different wavelengths. The modified setup of such an DLCZ-style elementary link is shown in Fig. 2.7.

The photon that is coupled into the fiber should ideally have telecom wavelength, while the photon that will be stored into the memory should have a wavelength suitable with the bandwidth of the memory. These two wavelength are typically quite different. Secondly, if the memory allows for the storage of many different photonic modes at the same time this approach promises greatly improved entanglement rates as will be discussed in detail in section 2.6.

The separation of source and memory only slightly changes the basic entanglement generation protocol of the DLCZ approach.
Instead of having just one atomic ensemble in each location, now there will be an absorptive quantum memory and a photon-pair source per location. The photon-pair sources are then simultaneously and coherently excited such that each source has a small probability $p_e/2$ of emitting an entangled photon pair corresponding to

$$|\psi\rangle_{PPS} = \left(1 + \frac{p_e}{2}(a^\dagger a'^\dagger + b^\dagger b'^\dagger) + \mathcal{O}(p_e)\right)|0\rangle_{AB}\,, \tag{2.19}$$

where a, b describe photonic modes from source A and B respectively, while the prime indicates a difference in modes, e.g. non-primed emitted towards measurement station and primed emitted towards memory. For simplicity the phases of the different photonic modes have been omitted. $\mathcal{O}(p_e)$ describes the possibility of emitting multiple pairs. Since this introduces error (see section 3.2) the emission probability should be kept small, analogously to the original DLCZ protocol. Similarly to the original protocol the detection of a single photon after the central beam splitter heralds the storage of a single photon in one of the quantum memories. The resulting state is once again represented by (2.10). To swap the entanglement one can then just follow the original DLCZ protocol again.

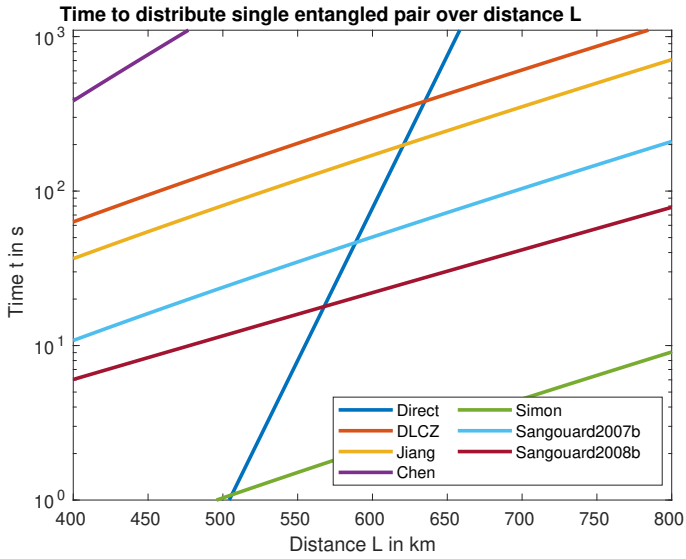

Figure 2.8: Comparison of different repeater protocols based on atomic ensembles and linear optics in terms of entanglement distribution time over total distance. The target end-to-end fidelity is $F = 0.9$ while we assume fiber losses of 0.2 dB/km corresponding to telecom fibers at 1.5μm and speed of light $c = 2 \times 10^5$m/s in the fiber. For **direct transmission** we assume a single-photon source emitting with a rate of 10 GHz. Furthermore in all approaches we set the efficiencies to $\eta_d = \eta_m = 0.9$. For the **DLCZ protocol** we set the emission probability to the value given in [15] $p_e = 0.010$. For the protocol presented by **Jiang et al.** [26] we used $p_e = 0.037$. For the approach of **Chen et al.** [27] we used a source repetition rate of $r = 10$MHz and an emission probability of $p_e = 0.01$. For the protocol proposed by **Simon et al.** [28] we used $m = 100$ modes and and $p_e = 0.009$. For the protocol introduced by **Sangouard et al. in 2007** [29] $p_e = 0.9$, while for **Sangouard et al., 2008** [30] we used $p_e = 0.013$ and again $r = 10$MHz. It is important to note here that, while for all the other protocols we set the number of elementary links used to bridge the total distance to $n = 4$, in this last approach we used $n = 8$ links, because this protocols favors a higher number of links [15].

2.5 Performance of different protocols

After having explained the DLCZ protocol in detail, we are now curious how it actually performs in comparison to direct transmission and other proposed repeater protocols. Specifically we want to analyze the rate at which each protocol can distribute end-to-end entangled states.
Sangouard et al. [15] list closed analytical expressions for a selection of protocols that are based on the original DLCZ protocol but try to improve on it in different ways and explains them in great detail. Here we are not interested in the analytical details but merely want to get an idea of how the protocols compare. A plot of the end-to-end entanglement times over different length L is shown in figure 2.8.

In the plot we picked different fixed values for the emission probability p_e from the literature as the optimal value varies for different protocols. See [15] for a detailed review of repeater protocols using atomic ensembles, including all of the ones shown in Fig. 2.8.

There are a number of things to point out about this figure.
Let's begin by comparing the DLCZ protocol to direct transmission. The choice of a source with repetition rate of 10GHz is both ambitious and somewhat arbitrary. However, for our comparison the exact choice of rate will not change the conclusions we draw since the scaling with distance is fundamentally different for direct transmission and quantum repeaters. Therefore the exact value will not change the fact that the curve for direct transmission will have a much steeper slope but will merely influence the exact position of where it

intersects the repeater curves.
For the DLCZ protocol the rate crosses the rate of direct transmission somewhere around $L = 630$km with an entanglement generation time of slightly above 300s for four elementary links. Above this distance the DLCZ protocol clearly outperforms direct transmission but the rate of roughly $1/300s \approx 3.3mHz$ at this point is pretty low. Most importantly it requires memories that can store the entanglement for times comparable to 300s. This is very challenging even with recent experimental advances [15], [23], [24]. This simple comparison using the analytical models given by Sangouard et al. [15] clearly shows the need for more sophisticated repeater protocols that can significantly improve the entanglement generation time.
Secondly Fig. 2.8 shows that this is indeed possible. There are numerous proposals of protocols based on the original DLCZ protocol that either try to improve the rate [26], [29], [30] or the robustness [27] of the protocol. The most notable improvement however is achieved by the protocol proposed by Simon et al. [28], clearly outperforming all others protocols. Therefore in the following we will investigate the reason for this drastic improvement in rate, called **multiplexing**. This will be a central concept in this work.

2.6 Multiplexing

To understand what multiplexing is and what it is for we need to take a look at two major limitations of the protocol.

Firstly, once a Stokes-photon has been generated by illuminating the atomic ensemble with a write laser pulse, one has to wait at least for the time $t_{wait} = L_0/c$ before one can try generating entanglement again. Here t_{wait} is the time it takes the photon to travel to the central station and the classical information about the measurement result to travel back. After every unsuccessful attempt the memory must be emptied before trying again [15]. This obviously puts a fundamental upper bound on the achievable entanglement rate of $r_{max} = L_0/c$.

Secondly, both the emission of the photon and the Bell state measurement at the midpoint are probabilistic processes. Thus the rate will usually be quite far below the above bound. In order to compensate for the probabilistic nature of the protocol one must therefore find a different approach.

We will discuss physical devices needed to enable such a multiplexed protocol in section 2.8, but it is worth noting here that separating source and memory as described previously is especially well suited for sending many modes. However, there are also other approaches to enable multiplexing for the DLCZ protocol as we will discuss in section 6.2.
There are many different possibilities for the degree of freedom that is used for multiplexing, but the three most common ones are time, frequency and location. No matter which degree of freedom is used the effect is always the same. The entanglement rate of an elementary link now scales as

$$p_{link} = 1 - (1 - p_{single})^M, \tag{2.20}$$

where p_{single} is the success probability of a single mode and M is the number of modes. It is therefore clear that since $(1 - p_{single}) \leq 1$ we get $\lim_{M\to\infty} p_{link} = 1$. For a more detailed analytical discussion see section 4.2.2. We will now give some examples to clarify the implementation of multiplexing.

2.6.1 Temporal multiplexing

If the quantum memory used allows for storage of not just one photon but a train of photons one can use it for temporal multiplexing. In this scenario one can trigger the source many times per waiting time t_{wait}, probabilistically generating entangled photon

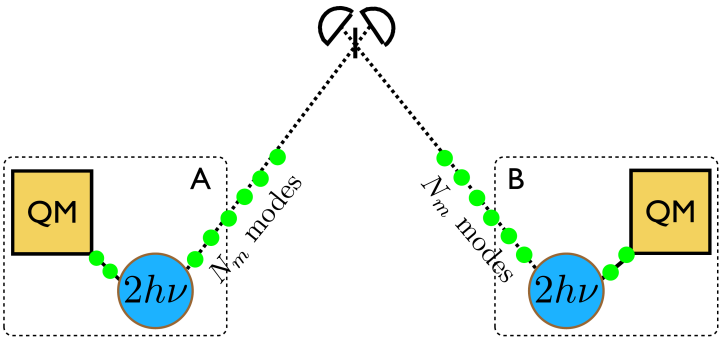

Figure 2.9: Entanglement generation using temporal multiplexing as proposed in [28]. The photon-pair source (blue) can be triggered many times N_m in each time interval L_0/c. One mode of each generated pair is saved in the adjacent multi-mode quantum memory (yellow square) while the other one is sent to a central Bell state measurement [15].

pairs in different time slots i. The modes a_i, a_i' are then referred to as different temporal modes, where $i = 1, ..., M$ with M the total number of temporal modes.

Fig. 2.9 shows such a setup, where all the primed modes a_i' and b_i' are stored in the adjacent quantum memories while the unprimed modes are sent to the central measurement station. At the central station Bell state measurements are performed on every temporal mode independently and therefore any of the modes a_i or b_i can now cause a successful measurement. This increases the entanglement generation probability of the elementary link P_{link} as described in (2.20).

In order to swap entanglement in such a protocol one has to be able to recombine exactly those modes, whose partners have taken part in a successful BSM. Say we have two elementary links AB and CD and mode 5 was successful in AB, while mode 1 was successful in CD. Then mode b_5' and c_1' must be simultaneously combined at the beam splitter of the swapping BSM. There are a number of promising approaches to realize a quantum memory with the required properties, e.g. based on photon-echo and we will discuss one particularly promising approach based on **atomic frequency combs** [31] in section 2.8.2.

2.6.2 Spectral multiplexing

Another popular approach is spectral multiplexing. Instead of triggering the source many times in one time interval L_0/c to create many different temporal modes, one now creates many modes with different frequency in the same pulse. As can be seen in Fig. 2.10 one half of each spectral mode created in this way will be stored in the adjacent memory while the other half is sent to the midpoint station. Every spectral mode is measured independently at the same time and can cause a successful measurement. The information of which spectral mode was successful is sent back classically so the correct spectral modes can be combined at the swap.

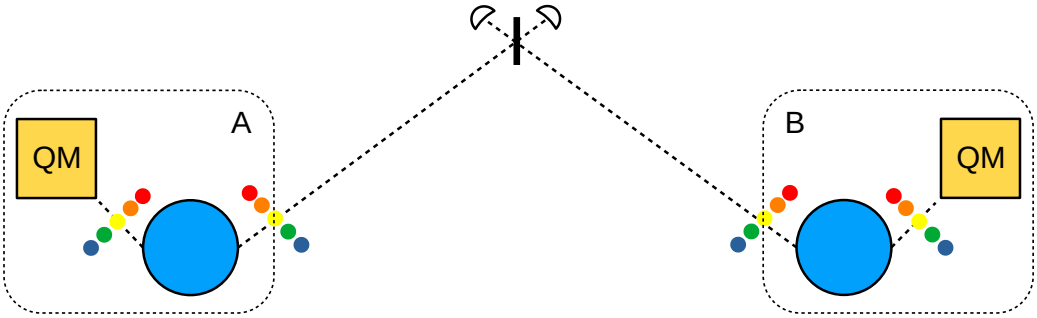

Figure 2.10: Entanglement generation using spectral multiplexing. The photon-pair source (blue) can generate many different spectral modes simultaneously. One mode of each generated pair is saved in the adjacent spectrally multi-mode quantum memory (yellow square) while the other one is sent to a central Bell state measurement station which simultaneously performs a BSM on all the different spectral modes.

This again gives the same fundamental increase in rate as the previous approach. For a more detailed analytical discussion, see section4.2.2.

This makes multiplexed protocols the most promising candidate for beating the rate of direct transmission. In the following section we will discuss a more recently proposed protocol using spectral multiplexing that uses imperfect physical components which can already be realized in experiments today.

2.7 A practical approach - Quantum Repeaters with Parametric Down-Conversion and Atomic Frequency combs

As multiplexing enables quasi-deterministic entanglement distribution over elementary links (see. (2.20)) it also significantly reduces requirements on the individual components used. Since the elementary link success probability can (in theory) be arbitrarily increased through the number of modes it allows the source to operate with very low emission probabilities, thus enabling the use of probabilistic photon sources such as **SPDC** sources. Similarly, since the links are deterministic, there is no need to store entanglement for multiple attempts. Therefore we can adapt the entanglement protocol and work with memories that are highly multi-mode but can have shorter storage times. Instead of storing the entanglement in elementary links until we have success in all links (potentially at different times) we now apply a round based approach. In every round we attempt to generate entanglement in all elementary links simultaneously. If all elementary links succeed in the same attempt we swap entanglement simultaneously at all repeater nodes. If one or more elementary links failed we discard the attempt, reset all of the memories and try again on all links. This reduces the necessary storage time on the memory to only one cycle time L_0/c.

In this section we will present in more detail the protocol that we will focus on for our simulation and justify why this is an interesting candidate.
The original DLCZ protocol as well as the protocol by Simon et al. [28] both rely on the use of single-photon interference to create entanglement over an elementary link. As we have seen in equation (2.16) the growing vacuum component limits the performance of such protocols. Also single-photon interference requires interferometic stability over great distances which is difficult to achieve experimentally.
This experimental challenge can be circumvented by creating elementary link entanglement based on two photon interference [30], [32]. In turn, this requires simultaneous single photon pair emission from both sources in a link, such that one photon from each pair

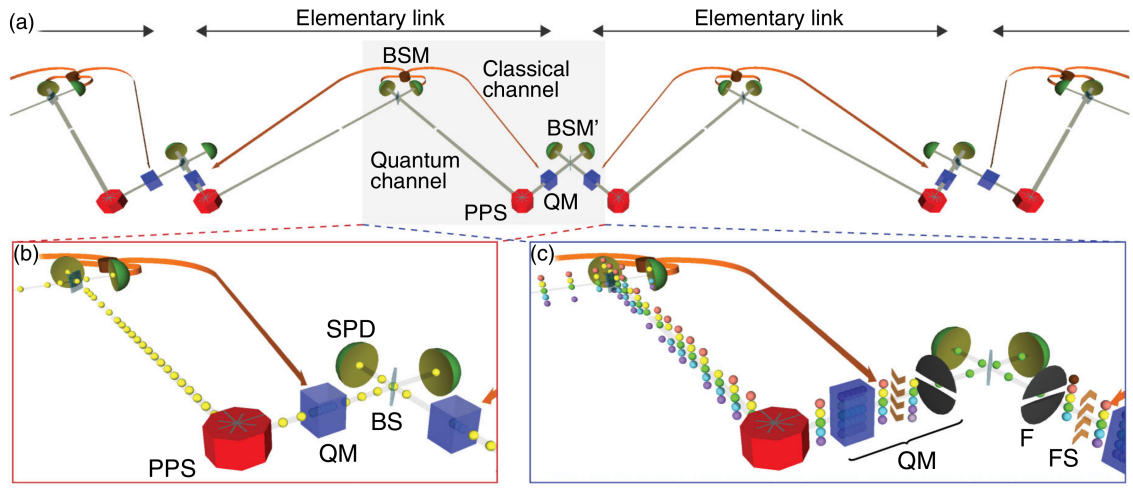

Figure 2.11: Illustration of the repeater protocol used by Sinclair et al. in [32]. Each elementary link contains two photon pair sources (red) and quantum memories (blue). Both sources emit a pair of photons in M different frequency modes. One half of the pair is stored in the quantum memory while the other half travels to the midpoint where each mode is measured independently. Photons are now in time-bin/polarization encoding, thus two-clicks in any mode (one click per time-bin/polarization) heralds successful entanglement generation. The projections on the Bell states resulting from the different possible click patterns of the detectors are shown in Fig. 2.12. Information about which mode was successful is then sent classically to the nodes where all spectral modes are shifted in frequency such that the successful mode ends up at a pre-agreed frequency. All other frequency modes are then filtered out, and the photons coming from adjacent links interfered at a swapping BSM, thus erasing any which way information. (a) shows the general setup of the setup, (b) shows the implementation of temporal multiplexing and (c) depicts the combination of temporal and spectral multiplexing including the filtering process at the swap.

can interfere at the midpoint measurement station. This also makes the protocol more sensitive to detector imperfections as two-photons now need to be detected correctly.

The protocol proposed in [32] is also used in the group of Wolfgang Tittel here in Delft. It is shown and described in Figure 2.11 and it will the protocol used throughout this thesis unless explicitly stated otherwise.

2.8 Physical Devices

The multiplexed nature of this protocol allows it to compensate for low emission probabilities of the photon pair source and allows for shorter memory times as long as both components are highly multi-mode. Therefore it uses a photon pair source based on spontaneous parametric down-conversion, or **SPDC source** for short. The basis of the quantum memory is a concept known as **Atomic Frequency Combs (AFC)**. In this section we will give a detailed description of how these real physical systems work and what imperfections they introduce.

2.8.1 SPDC Sources

For the protocol shown in Fig 2.11 we need a source component which can produce pairs of entangled photons. A very well known and understood physical process producing such as pair is spontaneous parametric down-conversion [34]. In this nonlinear instant optical process one photon of higher energy, the pump photon, is converted into a pair of photons of lower energy (signal and idler), according to laws of energy and momentum conservation

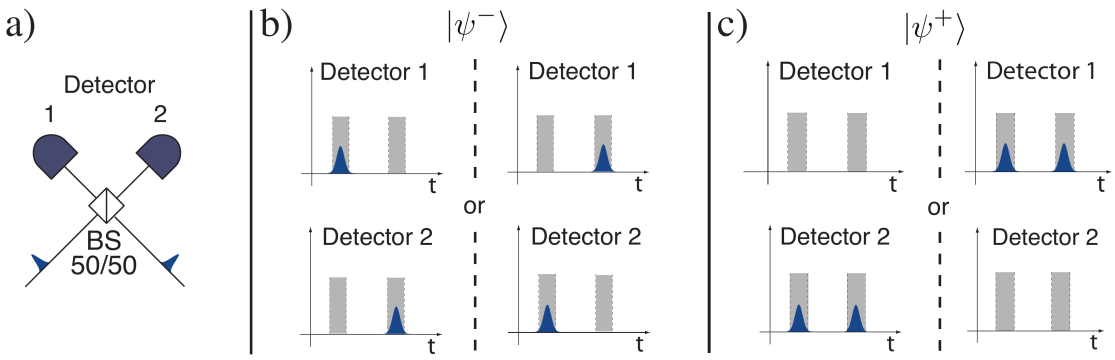

Figure 2.12: Projection on Bell states for time-bin encoded protocols [33]. **a)** General setup of the Bell state measurement for time-bin qubits using linear optics and photon counting detectors. **b)** Detector click patterns for projections onto $|\Psi^-\rangle$. **c)** Detector click patterns for projections onto $|\Psi^+\rangle$. All other click patterns are discarded as failure thus leading to a maximum success probability of the BSM of 50% (4 out of 8 possible patterns are successes). It is worth noting that these results can also be mapped to other double-click protocols such as ones using polarization encoding.

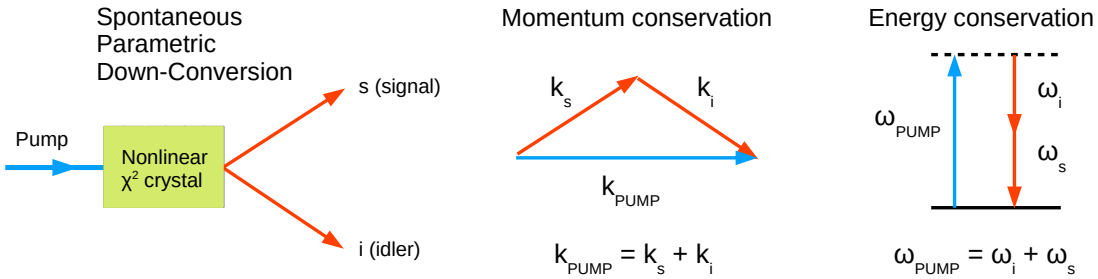

Figure 2.13: Schematic of the SPDC process and the concepts of energy and momentum conservation. A photon of higher energy (pump), is converted into a pair of photons of lower energy (signal and idler) in a non-linear process according to laws of energy and momentum conservation [35].

(see Fig. 2.13) [35].

To use this process in a component a non-linear crystal is combined with a pump laser, to produce entangled pairs of signal and idler photons [35]. A great benefit of using this process is that the wavelengths of the outcoming photons can be tuned within the limits of energy-momentum conservation and do not have to be the same. This way one of the photons can be at the optimal operation wavelength of the quantum memory while the other photon can be at telecom wavelength. This tuning is achieved by using a periodically poled lithium niobate (PPLN) crystal [36]. Using periodic poling we can change the momentum phase matching condition in Fig. 2.13 into the quasi-phase-matching condition $\mathbf{k_{Pump}} = \mathbf{k_s} + \mathbf{k_i} + \mathbf{k_p}$, where $\mathbf{k_p}$ is an additional momentum contribution corresponding to the wavevector of the periodic structure [37]. This way in principle any three-wave mixing process that satisfies energy conservation can be phase-matched thus allowing for perfect tuning of signal and idler frequency by simply changing the temperature of the crystal.

There are three different kinds of crystals in spontaneous parametric down-conversion differing by the polarization of the produced photons [35]. Some types of crystals produce pairs that are entangled in polarization however in the protocol of Tittel et al. the photon pairs are generated not in polarization but time-bin encoding. The type of crystal is therefore chosen such that both signal and and idler photon have the same polarization to

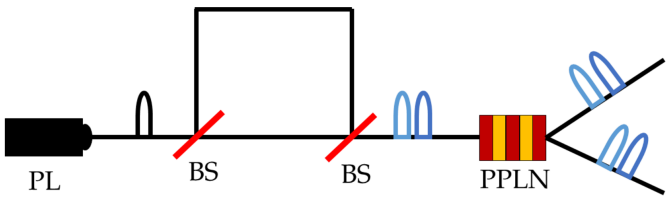

Figure 2.14: Creation of time-bin encoded entangled photon pairs with a PPLN crystal. A pump laser (PL) emits a photon, which travels through an unbalanced Mach-Zehnder interferometer with different arm lengths and two beam splitters (BS). This results in a photon that is in a superposition of being in the early and late time window which are generally separated by a few ns. These photon state then continues to the periodically poled lithium niobate (PPLN) crystal, which creates a time-bin encoded photon pair through spontaneous parametric down-conversion. Figure is taken from [38].

make them indistinguishable. The ideal output state is

$$|\phi\rangle_{SPDC} = \frac{1}{\sqrt{2}}(|e_s, e_i\rangle + |l_s, l_i\rangle) \tag{2.21}$$

$$= \frac{1}{\sqrt{2}}(|1,0;1,0\rangle + |0,1;0,1\rangle), \tag{2.22}$$

where $e/(l)$ symbols the presence of a photon in the early/(late) time-bin (subscript i, s for signal and idler). The second line is just a different representation of the same state where each ket is $|e_s, l_s; e_i, l_i\rangle$ and 1,0 represent presence or absence.

Obtaining such a state is achieved by pumping the crystal with photons that are in superposition of early and late time window $|\phi_{pump}\rangle = (|e\rangle + |l\rangle)/\sqrt{2}$. This can be achieved by first sending the laser light through an Mach-Zehnder interferometer with different arm lengths as shown in Fig. 2.14.

SPDC Sources are inherently highly multi-mode as many pairs of entangled photons can be created independently in different spectral modes.

However the process is by definition spontaneous and therefore probabilistic. This means that a single pair is emitted only with a probability of p_e, which depends on the pump power of the laser. It also means there is an intrinsic probability to emit more than one photon pair. In fact the photon number distribution can be derived from the two-mode squeezing Hamiltonian and is given by [34]

$$p_e^{SPDC}(n) = (n+1)\frac{\mu^n}{(\mu+1)^{(n+2)}}, \tag{2.23}$$

where n is the number of emitted photons and μ is the mean photon pair number. μ increases with the pump power of the laser and it is obvious that the probability of emitting multiple photon pairs grows with μ. This significantly limits the performance of the protocol as we investigate in sections 3.2 and 5.2. However choosing μ too low also reduces the entanglement generation rate as we then mostly produce vacuum. It is therefore clear that μ is an important parameter to optimize over. However without a model that correctly implements multi-pair emissions no accurate analysis is possible. Especially if one wants to optimize μ for e.g. large repeater chains an efficient simulation framework is needed. Offering such a framework is one of the main contribution of this work and will be discussed in later chapters.

2.8.2 AFC Memories

For any scalable quantum repeater protocol we need to store entangled qubits for long enough to be able to perform further operations on them. For example, we need to store

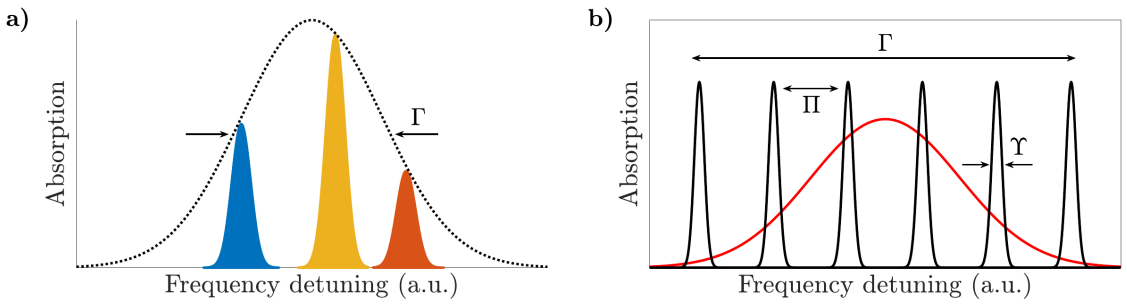

Figure 2.15: Illustration of the setup for the AFC protocol. a) An inhomogeneously broadened medium with a FWHM of Γ is created by a combination of homogeneously broadened absorption peaks, which are shifted due to changes in their local environment. b) Delocalized storage in which a probe photon (red envelope) is absorbed by an inhomogeneously broadened medium with spectral width Γ, which is split up into equidistant peaks with spacing Π that have a FWHM of Υ. Both figures are from [38].

the qubits at a repeater node sufficiently long to have successful entanglement generation in both adjacent elementary links before we perform the swapping operation on them. Since most protocols include one or more probabilistic operations, such as optical Bell state measurements or entanglement purification, the availability of quantum memories is essential to any long distance entanglement protocol.
It is worth noting that for applications requiring short storage times a low-loss optical fiber could be sufficient to delay photons until a classical signal arrives. However, for applications where storage times exceed around 10 μs, fiber transmission drops below 90% (2.1) and quantum storage based on light-matter interaction will be necessary [32]. Different types of such memories based on atomic ensembles have been proposed like EIT (electromagnetically induced transparency) [20], [39] or AFC (atomic frequency comb) [31], [40] based memories. Here we will focus on AFC memories which are also used in the protocol by Sinclair et al [32]. For a comparison of the two types of memories see [38].

Atomic frequency comb memories consist of an ensemble of atoms with at least one exited state $|e\rangle$ and one ground state $|g\rangle$. The optical transition $|g\rangle - |e\rangle$ is assumed to have a narrow homogeneous linewidth but a large inhomogeneous broadening [31]. Rare-earth doped crystals such as thulium or erbium, which are commonly used for AFC memories, are a good example of such a material [41]. The ions of the dopant have a narrow linewidth, but each individual ion has a slightly different local environment in the crystal, e.g. with different stress/strain on the lattice and different local fields. It is therefore intuitive that the transition will have large inhomogeneous broadening due to the contributions of the many individual ions.

Furthermore the atomic density function of the transition is designed to be a series of narrow peaks spanning a large range in frequency space resembling the shape of a comb, such giving the memory its characteristic name . This profile can be produced by optically pumping atoms of certain frequencies from the ground state $|g\rangle$ to a meta-stable auxiliary state $|aux\rangle$, e.g. an additional hyperfine state of $|g\rangle$.

An absorbed photon will be stored in the AFC as a single excitation de-localized over all atoms in the ensemble that are in resonance with the photon. This process is shown in Figure 2.15. The resulting state can be written as a collective Dicke state [42]

$$|\Psi\rangle = \sum_{j=1}^{N} c_j e^{i\delta_j t} e^{-ikz_j} |g_1 \dots e_j \dots g_N\rangle, \tag{2.24}$$

where z_j is the position of the atom j, k the wave-number of the light field, δ_j the detuning

of the atom with respect to the laser frequency and the c_j the amplitude. c_j depends on the frequency and position of the particular atom j.

This state is reminiscent of the state of the stored Stokes-photon (2.6) in the original DLCZ protocol. However the stored state in the AFC memory will now rapidly dephase due to the relative detuning $e^{i\delta_j t}$ of the different modes. After a fixed time $t_{rephase} = 2\pi/\delta_j$ the system will rephase and emit the photon while returning to the collective ground state. The retrieval efficiency of the AFC protocol is given by [40]

$$\eta_0^{AFC} = e^{-d_0} e^{-7/F^2} e^{d/F} \left(\frac{d}{F}\right)^2, \tag{2.25}$$

where d is the optical depth of the medium, $F = \Pi/\Upsilon$ the finesse of the comb and d_0 is the residual optical depth caused by left-over atoms that were not correctly transferred to the auxiliary state during the creation of the comb. The first factor in (2.25) thus captures imperfections in the AFC preparation. The second factor represents loss due to dephasing while the last two terms represent losses due to re-emission and re-absorption. There is various possibilities and proposals of how to improve theses efficiency, such as embedding the memory in an optical cavity [43].

However, there is an additional fundamental limitation of the protocol. The excited level used for storage only has a finite coherence time T_c. This causes the retrieval efficiency to degrade with time as

$$\eta^{AFC}(t) = \eta_0^{AFC} \times e^{-t/T_c}. \tag{2.26}$$

Storage times for AFC based quantum memories of the order of seconds have been shown [23], while other results show their multi-mode capabilities [44] and close unit input-output fidelity $F_{IO} \approx 93 \pm 2\%$ of the retrieved photons [45]. The large inhomogeneous broadening of rare-earth doped crystals makes them an ideal technology to be extended to even higher multi-mode capacity [15]. This makes them a very promising candidate for multiplexed quantum repeater architectures.

However if one wants to accurately investigate the scalability of a repeater protocol using AFC memories it is clear that the underlying model needs to be able to correctly capture the time dependence in (2.26) which also becomes much less trivial once one considers a modified version of the AFC model which allows for on-demand retrieval of photons and is explained in 6.2.

This concludes our discussion of a real physical implementation of a quantum repeater protocol using atomic ensembles.

2.9 Secret-key rate

From the previous section it is clear that promising candidates for the required components of a quantum repeater protocol exist. However if one wants to make any prediction about how their performance scales in an actual quantum network the underlying model needs to capture their various imperfections such as multi-photon emission and time-dependent efficiency. This will be one of the key contributions of this thesis.

In order to analyze scalability we also need to define a figure of merit we want to investigate. To this end we choose the **secret key rate (SKR)** obtainable for Quantum Key Distribution using the BB84 protocol [6]. It is the rate at which secret key can be distributed and it is a compelling figure of merit as it combines the rate of entanglement generation and the fidelity of the created end-to-end state. In the BB84 protocol a secret key is constructed by performing measurements in two orthogonal bases, typically X and Z. In each round, the two parties Alice and Bob independently and randomly pick one

of these two bases to measure their photons in. The measurement outcome is stored as a single classical bit. After a certain number of rounds they communicate their basis choices via classical communication. The secret key is then extracted by comparing the measurement outcomes of the rounds in which Alice and Bob measured in the same basis, after they have performed error correction and privacy amplification.

In case of time-bin encoding, measurements in the Z basis are performed by measuring the photons in both time bins separately. After successful entanglement generation between the end-nodes the expected shared state will be either $|\Psi^+\rangle$ or $|\Psi^-\rangle$ (see Fig. 2.12), such that measurements in the Z basis should always be anti-correlated. This implies that if Alice measures a photon in the early time bin, Bob should measure a photon in the late time bin.

If we want to perform measurements in the X (or Y) basis, we will need to be able to interfere the two time bins. For a more detailed discussion of how this is done see section 3.4.3. Measurements in the X basis can be both correlated or anti-correlated, depending on the BSM outcomes a long the repeater chain. This is due to $|\Psi^+\rangle$ an $|\Psi^-\rangle$ having different eigenvalues in the X basis.

We can now compare the actual measurement outcomes of Alice and Bob with these expected correlations. The fraction of wrong bits among the measurement outcomes in each basis is called the **Quantum Bit Error Rate (QBER)** and is determined individually for X and Z.

From this we then compute the secret key rate R_{SK} as

$$R_{SK} = R_{succ} \times max(0, 1 - H(Q_X) - H(Q_Z)), \tag{2.27}$$

where $H(x)$ is the binary entropy, Q_X, Q_Z are the QBERs in X and Z basis and R_{succ} is the rate of successful end-node measurements.

There have been a number of analytical investigation on the secret key rates of atomic ensemble based quantum repeater protocols and we will discuss them in detail in Chapter 4.

To conclude this chapter let us quickly summarize what we have learned. We started out by identifying exponential losses and the quantum no-cloning theorem as the fundamental problem of quantum communications. We then found a simple way of dealing with this problem with quantum repeaters called the DLCZ protocol. Among the various protocol that were developed from it we identified multiplexed protocols to be the most promising candidates. Therefore we then introduced a very promising new approach which is under active development within the Quantum Internet Alliance. Through the example of this protocol we investigated the physical processes involved in real components and already hinted at important noise parameters they introduce. We closed the chapter with an introduction to the main figure of merit we will be using for the rest of this thesis.

Chapter 3

Simulation

3.1 Introduction

Having the necessary physical background we now want to give a detailed description of how we implement this in our simulation. We start by first motivating the need for a simulation by showing the effects of multi photon emission as a major source of error in atomic ensemble repeater protocols. We then introduce our main tool, the NetSquid Simulator and proceed by going over the modeling of the different components. We finish the chapter by giving a detailed account of how we implemented the multi-photon events mentioned in the motivation.

3.2 Motivation: Multi-photon errors

In any protocol that relies on linear optical BSMs the probability of emitting multiple pairs from the source will be a cause of error. Most analytical discussions so far avoid this by assuming small emission probabilities p_e such that the multi-photon emission is sufficiently suppressed. However, working with such low emission probabilities has a large negative impact on the achievable rate.

Guha et al. [46] present an exact numerical calculation of the secret key rate including two-pair emission and show that even a small amount of multi pair emission probability can be detrimental to the usability of the protocol. Fig. 3.1 shows the secret key rate for a fixed set of parameters, where only the probability to emit two photon pairs $p(2)$ is varied from plot to plot. Starting at the top left plot one can see the typical behavior expected for perfect photon pair sources. The secret key rate is a graph with three distinct sections:

1. The first part of the graph is flat. This is the region where the number of modes used make successful entanglement over the elementary link (almost) deterministic.

2. In the second part the number of modes is no longer sufficient to compensate for the losses along the fiber due to the finite attenuation length. The number of attempts necessary for a successful entanglement generation increases while the rate drops exponentially.

3. In the third section, the probability of having a dark count in the detector becomes comparably to the probability of having a successful Bell state measurement at the midpoint. The errors introduced by the dark counts on the detectors rapidly drop the secret key rate to zero.

Adding repeaters decreases the rate at $L = 0$ as each swap is probabilistic, but the added repeater increases the flat part of the rate curve thus allowing the secret key rate to surpass

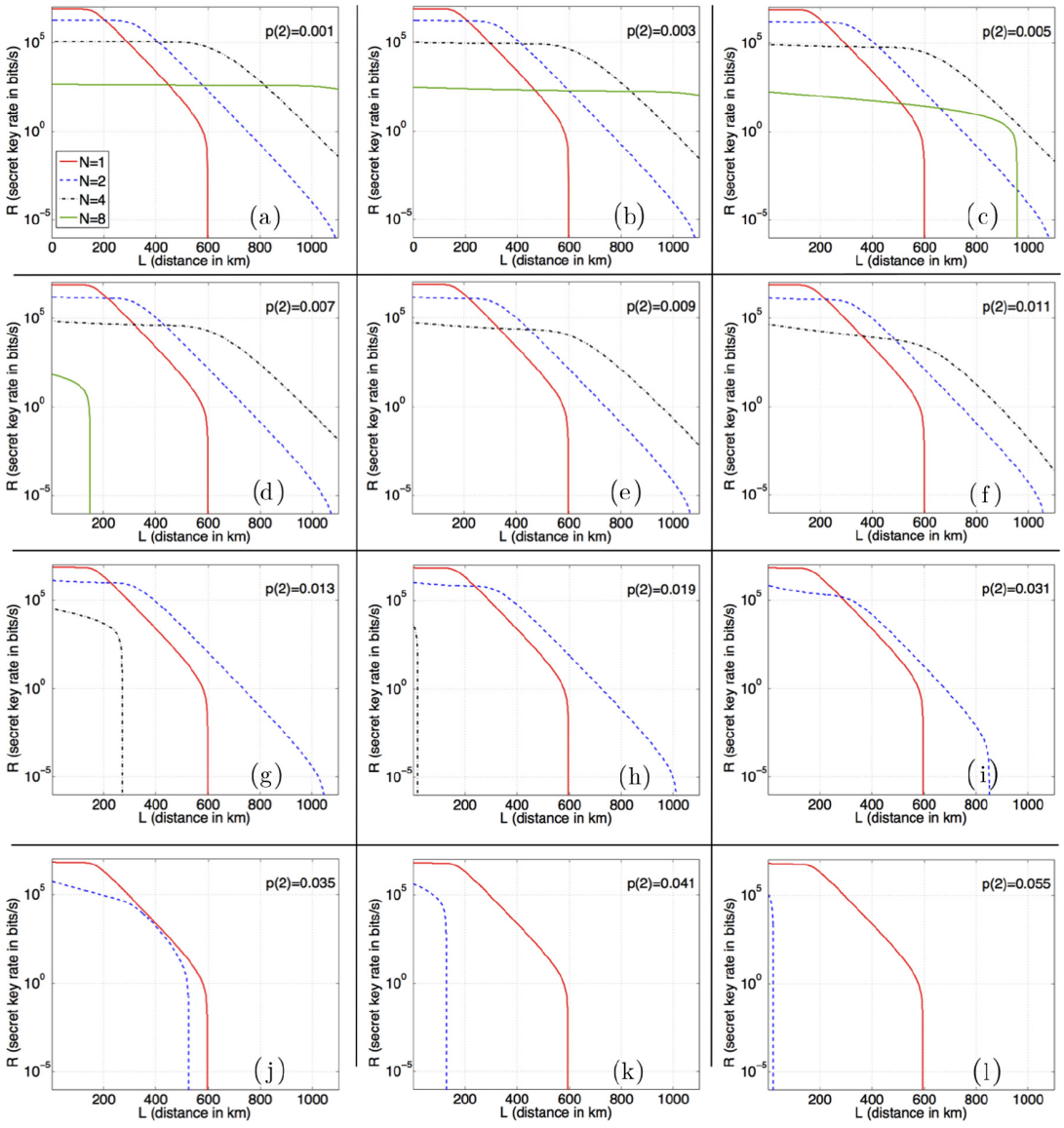

Figure 3.1: Numerical analysis of the Secret-key rate R_N over the total distance L for $N = 1, 2, 4, 8$ elementary links and two-pair emission probability $p(2)$ varied from 0.001 (top left) to 0.055 (bottom right). The parameters used are: clock rate of 20 MHz, dark count probabilities and efficiencies of all detectors of $P_{dc} = 10^{-6}$ and $\eta_d = 0.9$, $M = 1000$ frequency modes, attenuation of $\alpha = 0.15$dB/km and memory loss of 1 dB. For any given value of $p(2)$ there is a certain number N_{max} of elementary links up until which the secret-key rate remains almost identical to the perfect $p(2) = 0$ case. For $N > N_{max}$ the rate drops to zero at any distance L. It is clearly shown in (j)-(l) that for $p(2) \geq 0.035$ it is better to have a single elementary link between the end nodes than any number of repeaters. This figure is directly taken from [46].

the elementary link performance after a certain length.
However it is now interesting to observe what happens once one increases the probability of emitting a second pair. It is easy to see that between a probability of $p(2) = 0.001$ and $p(2) = 0.007$ (plots (a)-(d)) the secret key rate of 1,2 and 4 elementary links barely changes, while it comes crashing down for $N = 8$ links. As soon as the $N = 8$ curve has disappeared, the $N = 4$ curve begins to disappear as well (plots (e)-(h)) and the same happens to the $N = 2$ curve in plots (i) to (l). At a two-pair emission probability of $p(2) = 0.055$ the secret-key rate for the a single repeater has almost completely disappeared.
It is clear from this numerical analysis, that multi-pair emission poses a most serious problem to any repeater architecture relying on imperfect photon-pair sources with $p(n > 1) \neq 0$. For a more detailed discussion of the effects of multi-photon emission see section 5.2.

All near-term repeater experiments, such as the ones currently ongoing within QIA, employ probabilistic sources.

This leads us to two main conclusions:

- It is extremely interesting and important to have a way to accurately simulate multi-pair emission. Since the model by Guha et al. [46] only takes into account two pair emission it is crucial to expand this model also to higher photon numbers and different distributions. **This is one of the main goals of this thesis.**

- It is worth investigating ways to improve our repeater protocol, such that multi-photon errors are suppressed as much as possible.

As for the second point there is a significant research effort going into the development of quasi-deterministic photon pair sources, such as quantum dots [47] and there are also proposals of protocols using number-resolving detectors which can be used to further reduce multi-photon errors and have been investigated by Krovi et al. [48].

Nonetheless it is of great importance to offer a framework to investigate the effect of multi-photon emission accurately.

This is where our simulation comes in:
It enables us not only to accurately model multi-photon emissions (see 3.5), but also to take into account other sources of noise which are analytically difficult to treat. These currently also include time-dependent efficiency of the memory and photon-indistinguishability (see Chapter 5). Future plans also include simulations of e.g. timing jitters between the nodes.

Such a detailed simulation can be used to (a) **simulate the performance of current hardware in a large repeater experiment** as we do in Chapter 6, (b) run **optimizations to determine the influence of improving certain parameters**, see Chapter 7. This can then guide future experimental efforts.

With this clear motivation in mind we now turn towards the technical implementation and start with introducing our simulation software.

3.3 The NetSquid Simulator

For our simulations we use the purpose built '**Net**work **S**imulator for **Q**uantum **I**nformation using **D**iscrete events', or short **NetSquid** [49].

NetSquid is based on DynAA [50]–[52], a computer-aided analysis and design tool for the development of large, distributed, adaptive, and networked systems [13]. It is currently under active development at QuTech and will soon be released under public license.
NetSquid comes with many benefits.
On the one hand the front end is entirely written in Python, which makes it very easy to use. On the other hand the discrete event paradigm that is also known from classical

network simulators [53], [54] allows NetSquid to efficiently simulate the transmission and decay of quantum information in combination with the complex and stochastic nature of repeater protocols. It is able to perform arbitrary quantum operations and its modularity in terms of components and protocols allows us to easily investigate networks containing many nodes and different component technologies. This makes it a perfect tool for our purpose.

However NetSquid only provides very general base components and models. For our simulation we need components and models that are more specific to the actual physical setup described in the previous chapter. Therefore we had to make a number of additional components and features that can now be found in the atomic ensemble Netsquid Snippet NetSquid-AE [55].

3.4 Components

The aforementioned modularity allows us to easily swap out any component in our simulation and exchange it for another. In the following we will go over the basic implementation of the components needed to simulate atomic ensemble based repeater protocols before going into more detail about how we implemented in the individual components.

3.4.1 Source

Any repeater protocol will need a source of the photons used to carry information. There are however a multitude of different available sources of entangled photons with different properties. Common to all sources is their ability to emit a certain photon state with a distinct emission probability distribution at a certain frequency. We therefore designed an abstract quantum source class which includes all these features and allows accurate simulations of many available technologies.

In the case of a perfect single photon-pair source, an emission probability p_e must be provided by the user. The source will then construct the correct state and schedule an emission event at a frequency specified by the user. Every time an emission is scheduled in the discrete event simulator a random number is drawn to determine whether a photon is emitted or not (using the specified emission probability). To allow for simulation of both single-click and double-click protocols the source supports dual-rail (e.g. time-bin) or single-rail (presence-absence) encoding.

For multi-photon emission, the user can either specify a mean photon-pair number μ for the probability distribution of a SPDC Source (2.23) or give a list $\{p(0), p(1), p(2), p(3)\}$ containing the individual probabilities of emitting no, one, two or three photon pairs respectively. This allows to quickly change between different kinds of sources with different distribution without needing to change any code of the component. For a more detailed description of the emitted state see 3.5.1.

For multiplexed operation this state can be independently and simultaneously emitted in any number of modes.

3.4.2 Channel

Both for classical and quantum channels we use the standard components supplied by NetSquid. These allow for different delay, loss and noise models to be applied to the transmitted items. This can be coupling loss of the photons , length-dependent attenuation, depolarizing or dephasing noise or Gaussian delay models. Any of these models can be switched out independently, thus allowing us to analyze the performance of a quantum network under any number of different scenarios for transmission.

For our analysis we generally assume that classical channels are noiseless and separate from the quantum channel. However classical channels also allow for arbitrary noise that can be specified by the user e.g. bit flip.

Channels can have arbitrary length therefore allowing for perfect flexibility in setting up any desired network topology. While in this work we always assume that the elementary link BSM station is positioned at the middle of the link this is a simple choice not a limitation given by the simulation.

3.4.3 Detectors

The next component common to all repeater protocols are detectors. In our simulation they are used for the midpoint BSM of the elementary links, the entanglement swapping at the repeater nodes and the measurement in different bases at the end nodes.

All detectors have detection efficiency η_{det} and dark count probability p_{dark} as parameters and the linear optical BSM also includes photon indistinguishability. The BSM is implemented by applying a set of POVMs to the arriving qubits and then classically adding dark counts and efficiency to the measurement outcomes. This allows us to easily implement number- and non-number-resolving BSMs. For a detailed derivation of the POVMs see 3.5.3.

The end node detectors support measurement in X,Y and Z basis. This enables us to not only perform the BB84 but in principle also the six-state protocol [56]. While the measurement in the Z basis is simply implemented as a threshold detector counting photons (in each time bin), the other basis measurements are slightly more difficult. For presence-absence encoding we apply a scheme as shown in Fig. 2.6 of interfering two repeater chains and simply use our regular BSM detectors together with an appropriate phase shift to change from X to Y basis. For time-bin encoding we need to interfere the two time-bins with one another. This can be achieved in two ways: either actively with an optical switch, or passively with an additional beam splitter. Both setups use threshold detectors and are shown in Fig. 3.2

Our component supports both modes of operation. Ultra-fast optical switches have been experimentally demonstrated but have a rather low efficiency of 1% [57]. However it is computationally much faster as for the passive setup the quantum state needs to be expanded which becomes slow when using the multi photon implementation detailed in 3.5. Additionally, for the passive implementation we need to use a squashing model as detailed in [58] to map the clicks in bins b_1, b_3, b_4 and b_6 onto click patterns in the interference bins b_2 and b_5. The active setup only has the two interference bins and therefore all click patterns can immediately be used without using squashing maps. In the end it is up to the user to choose between the two implementations, however in our simulation we use the computationally faster active switching. For future analysis of timing jitters we plan to also include detection time windows in our detectors.

3.4.4 Memory

Any scalable quantum repeater protocol will also need a quantum memory. For our abstract implementation of such a device we use the QuantumMemory class in NetSquid as a base. This means we can initialize a certain number of memory positions and for each of these positions choose a noise, loss or emission model.
In our simulation of AFC and EIT memories the main source of 'noise' in the memory is photon loss. Therefore we put a loss model on each of the memory positions similar to the one used on the quantum channel. It takes a maximum memory efficiency $\eta_{mem}(t = 0)$ and the coherence time τ_c of the state the photon is stored in. Once the qubit is taken

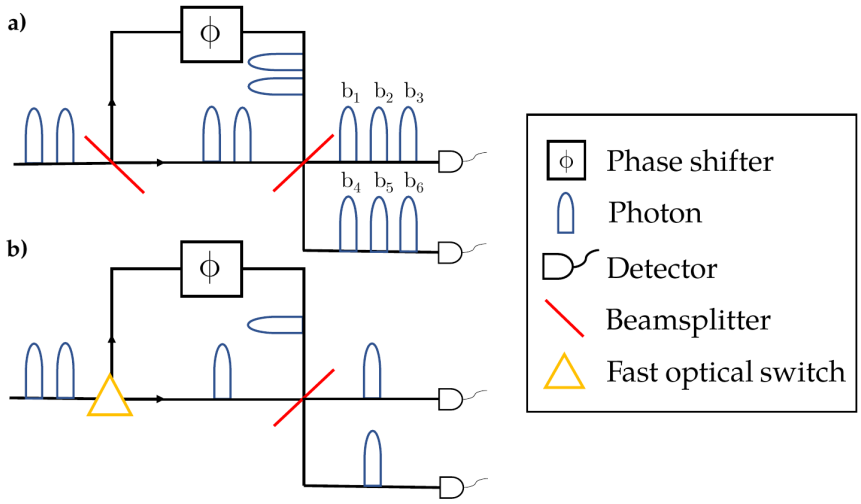

Figure 3.2: Schematic of the end node detector for time-bin encoding. The time-bins are interfered to perform a measurement in the X basis. A phase shift by $\pi/2$ on one of the arms allows for measurements in the Y basis. **a)** Passive setup with two beam splitters, in which the photon ends up in one of six detection bins $b1, \ldots, b6$, while we are only interested in clicks in bins b2 or b5 for our QKD measurements, since interference has occurred only in these bins. **b)** Active setup in which the early (late) photon is always routed through the long (short) arm by a fast optical switch, such that the time-bins will always correctly interfere at the beam splitter [38].

from the memory the probability of losing the qubit is calculated as

$$p_{loss} = 1 - \left(\eta_{mem}(t=0) \times e^{-\frac{t}{\tau_c}}\right) \tag{3.1}$$

where t is the time spent on the memory. Using this probability it then applies a generalized amplitude damping channel as detailed in 3.5.2. The qubit can be retrieved at any time, while in real AFC memories the photons will only be re-emitted once all the states in the Dicke state (eq. 2.24) rephase. (On demand memories are of course an exception) This needs to be accounted for by the protocols accessing the memory. Since in an experiment the storage time can be pre-programmed to the correct duration, it is equivalent to access the qubit only at this given time or having the memory emit it automatically.
With the flexibility given by the different noise models that can be put onto our memory component we want to make even more detailed simulations in the future, e.g. by modeling noise introduced by the read-out laser.

3.4.5 Magic

Though strictly speaking not a component of the simulation, there is one additional important concept that needs to be introduced. When analyzing long repeater chains or even more complex network topologies, simulating every single photon and every single quantum operations in every link becomes unfavorable. To enable an efficient simulation of such large scale networks we introduce a sampling method for our elementary links which we termed **"Magic"**. This simply means that the elementary link is not fully simulated but states are inserted into the memories "magically" and has nothing to do with "magic states" known in the context of error correction [59].

We distinguish between two kinds of Magic: analytical and sampled. For analytical Magic we implement a fully analytical model of the elementary link with a number of different states with corresponding probabilities calculated from the simulation parameters. This can for example be the model proposed by Guha et al. in [46]. The state is then

"magically" put into the memories of an elementary link after a certain generation time sampled from the probabilities, rather than simulating the full emission, loss, noise and measurement of the entangled-photon pairs. This is a very quick way to generate data, however it is not always possible to derive an exact analytical model, especially when combining many different sources of noise.

Therefore in this work we use the so called **sampled Magic**. This means we run the full simulation many times to generate a large set of sampled elementary link states with their corresponding midpoint outcomes and number of attempts it took to generate them. This can be done for a single elementary link or the end-to-end states of an arbitrary portion of a network for even larger simulations. This way we keep the full power of our simulation while allowing for arbitrary scalability.

However, this way of resampling states introduces additional statistical errors due to the finite size of the data set. This is known as a bootstrapping problem and we will be looking to quantify this in the future. It also means that for each set of parameters one needs to run the sampling again, making optimization a slow process. We are currently working on a way to make the sampling much more efficient which we will use for future optimization efforts.

This concludes the discussion of the basic building blocks used in our simulation. In the next section we will go into more detail about how we simulate multi-photon emission.

3.5 Simulation of Multi-photon Emission

As explained in the beginning of this chapter multi-photon emission is one of the largest sources of error in current repeater protocols. It is therefore of great importance to simulate this accurately. Unfortunately at the time of writing this thesis NetSquid does not offer the possibility to use qu-d-its, so we have to work with qubits to represent a multi-photon state.
A simple way of encoding a multiple-photon state with qubits is mapping the number of the Fock state to its binary representation:

$$\begin{aligned} |0\rangle &\rightarrow |00\rangle \\ |1\rangle &\rightarrow |01\rangle \\ |2\rangle &\rightarrow |10\rangle \\ |3\rangle &\rightarrow |11\rangle \end{aligned} \tag{3.2}$$

A multi-photon state $|n\rangle$, for $n \leq 3$, is therefore represented by two qubits in the simulation. Consequently the time-bin encoded state $|early, late\rangle = |n, m\rangle$, for $n, m \leq 3$, is represented by four qubits. Creating a pair of such states obviously doubles that number.
This change requires all our components to be able to handle such multi-qubit states. In the following we will go over each of the individual components in our simulation and describe in detail how they handle multi-photon emission.

3.5.1 Source - Multi-Photon Emission

Using binary encoding requires two main changes in our source component:
It needs to be able to emit groups of more than one qubit correctly representing a multi-photon state and it needs to correctly model the photon-number distribution of the physical source.
In the following we describe theses changes, both for time-bin and presence-absence encoding.

Time-bin encoding

The general state that a source generates for n time-bin encoded photons is given by [48]

$$|\psi\rangle = \sum_{n=0}^{\infty} \sqrt{p(n)}\,|\psi_n\rangle\,, \tag{3.3}$$

where

$$|\psi_n\rangle = \frac{1}{\sqrt{n+1}} \sum_{m=0}^{n} (-1)^m\,|n-m,m;n-m,m\rangle\,. \tag{3.4}$$

Note that (3.4) differs from what is used in [48], since for time-bin encoding the number of photons per time bin should be perfectly correlated, while the expression in [48] describes the anti-correlation between the polarization modes in the case of polarization encoding. For $n \leq 3$ photons, we therefore obtain the state

$$\begin{aligned}|\psi\rangle_{\text{time-bin}} = \sqrt{p(0)}\,|0,0;0,0\rangle &+ \sqrt{\frac{p(1)}{2}}\,(|1,0;1,0\rangle - |0,1;0,1\rangle) \\ &+ \sqrt{\frac{p(2)}{3}}\,(|2,0;2,0\rangle - |1,1;1,1\rangle + |0,2;0,2\rangle) \\ &+ \frac{\sqrt{p(3)}}{2}\,(|3,0;3,0\rangle - |2,1;2,1\rangle + |1,2;1,2\rangle - |0,3;0,3\rangle)\,,\end{aligned} \tag{3.5}$$

This state can be rewritten in binary representation as

$$\begin{aligned}|\psi\rangle_{\text{time-bin}} = \sqrt{p(0)}\,|00,00;00,00\rangle &+ \sqrt{\frac{p(1)}{2}}(|01,00;01,00\rangle - |00,01;00,01\rangle) \\ &+ \sqrt{\frac{p(2)}{3}}(|10,00;10,00\rangle - |01,01;01,01\rangle + |00,10;00,10\rangle) \\ &+ \frac{\sqrt{p(3)}}{2}(|11,00;11,00\rangle - |10,01;10,01\rangle \\ &\qquad + |01,10;01,10\rangle - |00,11;00,11\rangle).\end{aligned}$$

As noted before we therefore need 8 qubits to describe this state (4 in each half of the pair of which pairs of 2 describe the number of photons per time-bin).
Truncating the state after $n \leq 3$ photons also requires us to truncate the probability distribution for the SPDC source (2.23) accordingly, such that

$$\begin{aligned}p(0) &= \frac{1}{(\mu+1)^2} \\ p(1) &= \frac{2\mu}{(\mu+1)^3} \\ p(2) &= \frac{3\mu^2}{(\mu+1)^4} \\ p(3) &= 1 - \sum_{n=0}^{2} p(n) \\ &= \frac{\mu^3(\mu+4)}{(\mu+1)^4}\end{aligned} \tag{3.6}$$

Presence-absence encoding

For presence-absence encoding, the coherence of the state is embedded in the number of photons that are created by the pump photon. In the case of at most single photon events, we can thus resort to an emission probability that now denotes the probability of generating a perfect single photon pair, i.e.

$$|\psi\rangle_{\text{pa,s}} = \sqrt{1-p_e}\,|00\rangle + \sqrt{p_e}\,|11\rangle\,,$$

where the state $|ii\rangle$ now denotes i photons traveling to both directions with equal polarization and always emitted at the same time.
Now moving to the case of allowed multi-photon emission, we get the state

$$\begin{aligned}|\psi\rangle_{\text{pa,m}} &= \sqrt{p(0)}\,|00\rangle + \sqrt{p(1)}\,|11\rangle + \sqrt{p(2)}\,|22\rangle + \sqrt{p(3)}\,|33\rangle \\ &= \sqrt{p(0)}\,|00,00\rangle + \sqrt{p(1)}\,|01,01\rangle + \sqrt{p(2)}\,|10,10\rangle + \sqrt{p(3)}\,|11,11\rangle\,,\end{aligned} \tag{3.7}$$

where we can again use the truncated probability distribution (3.6). We also note that this encoding only requires 4 qubits per state (2 per half traveling in each direction) making it computationally lighter.

3.5.2 Photon Loss - Generalized Amplitude Damping

Photon loss, as it for example occurs in an optical fibre or a quantum memory, can be described by an amplitude damping channel. In the general case losing exactly k photons can be expressed by the following non-unitary Kraus operators describing both photon loss and the effects of amplitude decay [60]

$$A_k = \sum_{n=k}^{\infty} \sqrt{\binom{n}{k}} \sqrt{(1-\gamma)^{n-k}\gamma^k}\,|n-k\rangle\langle n|\,, \tag{3.8}$$

where γ is the probability of losing a photon. Specifically, γ depends on the time t the qubits spend on the memory (and the memory's maximum efficiency) or the length L of the quantum channel.

$$\gamma_{mem}(t) = 1 - (1-\gamma_{mem}(0))e^{-t/\tau} \tag{3.9}$$

$$\gamma_{chan}(L) = 1 - (1-\gamma_{chan}(0))e^{-L/L_\alpha}, \tag{3.10}$$

where τ is the memory lifetime and L_α the attenuation length of the channel.
The Kraus operators A_k satisfy $\sum_{k=0}^{\infty} A_k^\dagger A_k = \mathbb{1}$ and $A_k \geq 0$. The loss channel is therefore a completely-positive trace-preserving map.
In our case of having $n \leq 3$ photons the Kraus operators in binary encoding are simply

$$\begin{aligned}A_0 &= |00\rangle\langle 00| + \sqrt{1-\gamma}\,|01\rangle\langle 01| + (1-\gamma)\,|10\rangle\langle 10| + (1-\gamma)^{3/2}\,|11\rangle\langle 11| \\ A_1 &= \sqrt{\gamma}\,|00\rangle\langle 01| + \sqrt{2(1-\gamma)\gamma}\,|01\rangle\langle 10| + (1-\gamma)\sqrt{3\gamma}\,|10\rangle\langle 11| \\ A_2 &= \gamma\,|00\rangle\langle 10| + \gamma\sqrt{3(1-\gamma)}\,|01\rangle\langle 11| \\ A_3 &= \gamma^{3/2}\,|00\rangle\langle 11|\,.\end{aligned} \tag{3.11}$$

The action of the generalized amplitude damping channel on an arbitrary input state ρ_i is then described by

$$\rho_f = \sum_{k=0}^{3} A_k \rho_i A_k^\dagger. \tag{3.12}$$

For time-bin encoding the Kraus operators are simply $A_{ij} = A_i \otimes A_j$ with $i, j \in (0, 1, 2, 3)$.

3.5.3 Bell State measurement

Here we describe the modeling of our optical Bell state measurement setup (see Fig. 3.3) for multiple photons, that are not perfectly indistinguishable, coming from each side. If photons hitting the beam-splitter are distinguishable the beam-splitter will not perfectly erase the which-way-information and therefore no photon bunching, as described by the Hong-Ou-Mandel effect [61] , will occur (see section 5.4). This can be detected in the experiment and change the BSM outcome.
In the following we will derive the effective POVM operators for the Bell state measurement in terms of the photon indistinguishability / visibility ν and describe how dark-counts and detector efficiency are implemented. We will follow the derivation in [13] very closely but generalize it to arbitrary photon numbers.

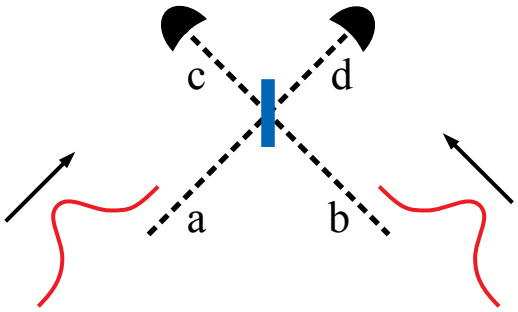

Figure 3.3: Schematics of the heralding station with input arms a and b, 50:50 beam-splitter (blue), output arms c and d and photon detectors (black). The two incident photons (red) interfering at the beam-splitter have visibility $0 \leq \nu \leq 1$.

Figure 3.3 shows a 50:50 beam splitter with input arms a and b, output arms c and d and photon detectors at the end of them. We will assume here that the photon detectors can count photons, i.e. there are different measurement outcomes for each number n of detected photons on a detector. From there it is then trivial to derive the corresponding POVMs for detectors which can not resolve different photon numbers, as we will demonstrate later.

Basis states

When modeling multi-photon emission, we can describe the state before the beam-splitter as a state living in the 4-qubit Hilbert space spanned by the 16 basis vectors:

$$|n, m\rangle_{ab} \tag{3.13}$$

with $n, m \in \{0, 1, 2, 3\}$ being the number of photons coming in through input arms a and b respectively. Describing the state solely by the number of photons hides the fact, that each photon can have a multitude of other degrees of freedom, such as polarization, spectral and temporal properties. Following [13], we will focus on spectral properties in the following, though this is easily generalizable to other degrees of freedom. A single photon in arm a with a spectral amplitude function ϕ can be modeled as

$$|1\rangle_a = \int d\omega \phi(\omega) a^\dagger(\omega) |0\rangle_a \tag{3.14}$$

where $a^\dagger(\omega)$ is the creation operator of a single photon in arm a of frequency ω and $|0\rangle_a$ is the vacuum. The state is properly normalized, such that

$$\int d\omega |\phi(\omega)|^2 = 1. \tag{3.15}$$

Consequently, we can then describe a single photon in arm b as

$$|1\rangle_b = \int d\omega \psi(\omega) b^\dagger(\omega) |0\rangle_b , \tag{3.16}$$

where we capture the fact, that the photons arriving at the beam-splitter can have different spectral properties by having different ϕ and ψ.
Therefore the basis states before the beam-splitter can be written as

$$|n,m\rangle_{ab} = \frac{1}{\sqrt{n!m!}} \left(\prod_{i=1}^{n} \int d\omega_i \phi_i(\omega_i) a^\dagger(\omega_i) \right) \left(\prod_{j=n+1}^{n+m} \int d\omega_j \psi_j(\omega_j) b^\dagger(\omega_j) \right) |00\rangle_{ab} . \tag{3.17}$$

The normalization factor in front comes from the property of the creation operator that $a^\dagger |n\rangle = \sqrt{n+1}\,|n+1\rangle$, or put differently $|n\rangle = \frac{1}{\sqrt{n}} a^\dagger |n-1\rangle$.
A temporal shift τ between the arrival times of the photons can be easily integrated into the basis state as well, by simply introducing the following action on the creation operators

$$b^\dagger(\omega) \to b^\dagger(\omega) e^{-i\omega\tau}, \tag{3.18}$$

but this will be omitted in the following for simplicity.

Beam-splitter

Let's now look at the next part of the BSM: the 50:50 beam-splitter. Its action on the creation operators is described by

$$\begin{aligned} a^\dagger(\omega) &\to \frac{1}{\sqrt{2}} (c^\dagger(\omega) + d^\dagger(\omega)) \\ b^\dagger(\omega) &\to \frac{1}{\sqrt{2}} (c^\dagger(\omega) - d^\dagger(\omega)). \end{aligned} \tag{3.19}$$

Thus, the basis states described by (3.17) of n, m photons arriving from a, b will after the beam-splitter become

$$\begin{aligned} |n,m\rangle_{cd} = &\frac{1}{\sqrt{n!m!}} \times \left(\prod_{i=1}^{n} \int d\omega_i \phi_i(\omega_i) \frac{1}{\sqrt{2}} \big(c^\dagger(\omega_i) + d^\dagger(\omega_i)\big) \right) \times \\ &\left(\prod_{j=n+1}^{n+m} \int d\omega_j \psi_j(\omega_j) \frac{1}{\sqrt{2}} \big(c^\dagger(\omega) - d^\dagger(\omega)\big) \right) |00\rangle_{cd} . \end{aligned} \tag{3.20}$$

With this, we can now define an isometry $U_{ab\to cd}$ describing the action of the beam-splitter on the basis states as

$$|n,m\rangle_{ab} \to |n,m\rangle_{cd} \tag{3.21}$$

for all n, m.
In our case of up to 3 photons coming from each input arm this will therefore by given by

$$U_{ab\to cd} = \sum_{n=0}^{3} \sum_{m=0}^{3} |n,m\rangle_{cd} \langle n,m|_{ab} . \tag{3.22}$$

Obviously a similar expression holds for arbitrary incoming photon numbers.
Since the states $|n,m\rangle$ are mutually orthogonal it can be easily checked, that $U_{ab\to cd}$ is indeed an isometry with

$$(U_{ab\to cd})^\dagger U_{ab\to cd} = \mathbb{1}. \tag{3.23}$$

With the beam-splitter unitary in hand we now have a look at the detectors.

Detectors

We assume that the detectors have a flat frequency response. The event that the detector at the end of arm c detected k photons and the detector at the end of arm d detected l photons can be described by the projector

$$P_{k,l} = \frac{1}{k!l!}\left(\prod_{i=1}^{k}\int d\omega_i c^\dagger(\omega_i)\right)\left(\prod_{j=k+1}^{k+l}\int d\omega_j c^\dagger(\omega_j)\right)\times \\ \times |00\rangle\langle 00|_{cd}\left(\prod_{i=1}^{k} c(\omega_i)\right)\left(\prod_{j=k+1}^{k+l} c(\omega_j)\right). \tag{3.24}$$

The six projectors for up to a single photon coming from each side, as described in [13], follow from this much more general expression. In our case of up to three photons coming from each side we get a total of 28 projectors $P_{k,l}$ with $0 \leq k+l \leq 6$.

Effective POVMs

Lets assume we have an arbitrary state $|n,m\rangle_{ab}$ and want to calculate the probability of obtaining a measurement outcome corresponding to the projector $P_{k,l}$ for the state after the beam-splitter $U_{ab\to cd}|n,m\rangle_{ab}$. Following Born's rule, this probability is

$$\langle n,m|_{ab}(U_{ab\to cd})^\dagger P_{k,l} U_{ab\to cd}|n,m\rangle_{ab} = \mathrm{tr}\Big[(U_{ab\to cd})^\dagger P_{k,l} U_{ab\to cd}|n,m\rangle\langle n,m|_{ab}\Big]. \tag{3.25}$$

From this equation we find that the effective POVM on ab of the BSM described by Fig. 3.3 is given by

$$M_{kl} = (U_{ab\to cd})^\dagger P_{k,l} U_{ab\to cd}. \tag{3.26}$$

The resulting expressions are fairly simple to evaluate using:

- The commutation relations of the creation/annihilation operators

$$\Big[a(\omega(w_i)), a^\dagger(\omega_j)\Big] = \delta(\omega_i - \omega_j), \tag{3.27}$$

  with all other commutators equal to zero.

- The properties of the δ-function

$$\int d\omega_j f(\omega_j)\delta(\omega_i - \omega_j) = f(\omega_i) \tag{3.28}$$

- The indistinguishability / visibility ν given by

$$\nu = \left|\left(\int d\omega \phi^*(\omega)\psi(\omega)\right)\right|^2. \tag{3.29}$$

  Note that the probability that incident photons on the beam-splitter go to different output arms is $\chi = \frac{1}{2}(1-\nu)$.

An explicit calculation of the POVMs for the single photon case can be found in the appendix of [13].
For the case of up to three photons the calculation involves a large amount of different combinations and is thus tedious to do by hand. Therefore, we used a script to calculate the full set of POVMs using a symbolic linear algrebra python module for quantum mechanics named QuAlg [62]. In the simulation the POVM operators are then converted to

Kraus operators by taking the matrix square root.
For detectors that can not resolve the exact photon number, but are instead simple threshold detectors the POVMs can be derived from the full set of POVMs by summation:

$$M(no-click) = M_{00} \tag{3.30}$$

$$M(c-clicked) = \sum_{i=1}^{n} M_{i0} \tag{3.31}$$

$$M(d-clicked) = \sum_{i=1}^{m} M_{0i} \tag{3.32}$$

$$M(both-clicked) = \sum_{i=1}^{n}\sum_{j=1}^{m} M_{ij}, \tag{3.33}$$

with n, m the maximum number of clicks in the detectors at the end of arms c and d respectively.

Dark-Counts and Detection Efficiency

After obtaining a click-pattern from applying the full set of POVMs (number or non-number resolving) dark-counts and detection-efficiency are applied classically:

- Each click of the 'perfect' measurement outcome can be lost with a probability of $p_{lost} = 1 - \eta_{det}$, where η_{det} is the detection efficiency. This for example means that if there were n photons on the detector the probability of having no click is p_{lost} for the non-number resolving but p_{lost}^n for the number resolving detector.
- With probability $p_{dc} = 1 - e^{-R_{dc}\tau_{det}}$ one dark count occurred during the detection time window and a click is added. Here R_{dc} is the dark count rate of the detector and τ_{det} is the detection time-window.

In that way we fully implement the entire linear optical Bell state measurement shown in Fig. 3.3, including photon-indistinguishability, dark-counts and detector efficiency for up to three photons coming from each side.

This way we show how we can correctly simulate multi-photon emission in every part of our simulation. Before we move on to the validation of our model let us briefly discuss how we collect our data.

3.6 Data collection

In order to calculate our figure of merit, the secret key rate (see section 2.9), we need to collect measurement data from our simulation. To this end every time after all the swaps and end node measurements are performed we collect all measurement outcomes and the basis the end-nodes measured in. We then determine the expected end-to-end Bell state from the measurement outcomes of the midpoint and swap BSMs along the repeater chain. From the expected end-to-end state we determine the expected correlation of measurement outcomes in the basis the end nodes measured in, given they both chose the same one. We then compare the actual measured correlation with the expected correlations to determine the QBER for each basis. Using (2.27) we then calculate the secret key rate.

For our error bars we use the standard deviation for the QBERs and the average number of attempts necessary to generate a successful end node measurement. However since the secret-key rate is not a smooth function we here simple give the minimal and maximal rate calculated from the minimal/maximal QBERs within their respective error bars. This

leads to the error bars of the secret key rate to sometimes drop to zero when the QBERs exceed certain threshold of $\sim 13\%$. Since we plot the secret key rate on a logarithmic scale this makes it appear as if we have really large error bars. This is however not reflecting large statistical uncertainty but rather the behavior of the secret-key rate that is calculated from binary entropies.

With a clear idea of how we obtain our figure of merit let us now turn to validating our model against existing models.

Chapter 4

Verification

4.1 Introduction

In order to verify our simulation, we follow the historical development of the spectral multiplexing approach. Therefore, we focus on three models in particular:

Sinclair et al. [32] introduces spectral multiplexing using AFC memories. In the supplemental material an analytical calculation for the probability and rate of end-to-end entanglement generation over n elementary links with m spectral modes is presented. A perfect photon pair source and negligible dark counts are assumed, thus arriving at a very simple closed form analytical expression. This seems like a logical starting point for the validation, as this is the most basic model and therefore well suited for finding any fundamental errors in our simulation.

Guha et al. [46] present an analytical solution of the secret key rate including dark counts and imperfect detectors, but again only for a perfect photon pair source.

Finally, to investigate multi-pair emission, Guha et al. [46] also finds numerical solutions for the secret key rate (see Fig. 3.1) that incorporates up to two-pair emission. This enables us to compare our implementation of multi-pair emission against their results.

This way all aspects of our simulation setup will be verified against the literature it was based on. At this point we would like to note that shortly before the end of this project first experimental data using atomic ensembles was published in Nature [63]. Due to the short time left we have not yet tried to reproduce their results with our simulation but this will be very interesting to look at in future work.

4.2 Validation of end-to-end entanglement rate

Here we will briefly remind ourselves of the setup that is assumed by Sinclair et al. [32]. Then the derivation of the analytical expression for the end-to-end entanglement rate is explained and finally we present the results of our simulation and how they compare to the prediction.

4.2.1 Setup

The setup used by Sinclair et al. [32] assumes a lossy quantum channel of length L with attenuation α. This total distance is then divided into n elementary links of length L/n. At each side of the elementary link is a spectrally multimode quantum memory with constant efficiency η_{mem}. Next to each memory is a source that generates entangled photon pairs in many spectral modes simultaneously, with the probability of emitting an entangled pair denoted by ρ. These different spectral modes are generated independent of each other.
Of each pair, one photon is immediately stored in the memory, while the other one travels

through the channel to a double-click midpoint bell state measurement. This linear optics BSM is performed on each spectral mode, using one photon from each source and has a success probability of maximally 1/2. Additionally the detectors have an efficiency of η_{d1} and are assumed to be noiseless (dark counts are thus neglected). The central station containing the detectors then sends a classical signal to the ends of the elementary link, heralding the successful spectral mode (multiple simultaneous successes are ignored).
To extend the entanglement over multiple elementary links , neighboring links must perform entanglement swapping. This is again done using a linear optic BSM, this time between two neighboring memories of different elementary links. To make the photons indistinguishable the frequency of both modes is converted to a pre-agreed upon common frequency. If all BSMs succeed entanglement between the end nodes of the quantum channel is established [32].

4.2.2 Analytical expression for rate of entanglement generation

With this information the success probability of end-to-end entanglement generation can be calculated.
Starting with a single elementary link the probability for a single spectral mode to trigger a successful BSM is given by

$$\begin{aligned} P_{success}(1mode) &= P_{successfulBSM} \times (P_{PhotonNotLost})^2 \\ &= \frac{1}{2} \times (\eta_{d1} \times \rho \times 10^{-\alpha L/2n})^2 \end{aligned} \tag{4.1}$$

where the square appears as two photons need to be detected at the central station. It has been assumed here that the two photons are perfectly indistinguishable (visibility $\nu = 1$). For m spectral modes the probability that all modes fail to generate entanglement over the elementary link is simply

$$\begin{aligned} P_{allFail} &= (1 - P_{success}(1mode))^m \\ &= (1 - \frac{1}{2}(\eta_{d1}\rho 10^{-\alpha L/2n})^2)^m. \end{aligned} \tag{4.2}$$

Therefore the probability for at least one spectral mode top be successful and thus the probability to generate entanglement over a single elementary link is

$$P_{link} = (1 - P_{allFail}) = 1 - \left(1 - \frac{1}{2}(\eta_{d1}\rho 10^{-\alpha L/2n})^2\right)^m \tag{4.3}$$

From this equation it is obvious that by choosing the number of spectral modes m sufficiently high, the probability of elementary link entanglement generation success can be brought arbitrarily close to 1.
To now swap entanglement between two links two photons need to be retrieved from their memories (η_{mem}^2) and then successfully detected (η_{d2}^2) at the BSM (50% success).

The probability to distribute entanglement over the entire distance with n elementary links ($n-1$ swaps) is therefore

$$\begin{aligned} P_{total} &= P_{SuccessfulSwap}^{(n-1)} \times P_{link}^n \\ &= \left(\frac{1}{2}\eta_{mem}^2\eta_{d2}^2\right)^{(n-1)} \left(1 - \left(1 - \frac{1}{2}\eta_{d1}^2\rho^2 10^{-\alpha L/n}\right)^m\right)^n \end{aligned} \tag{4.4}$$

It is worth noting that all deviation from deterministic success - again assuming sufficiently large m - is contained in the first term, describing the success of all swaps. Finally the actual rate of entanglement generation is simply

$$R_{success} = \frac{P_{total}}{\Delta t} \tag{4.5}$$

with Δt the time between successive attempts to generate entanglement [32]

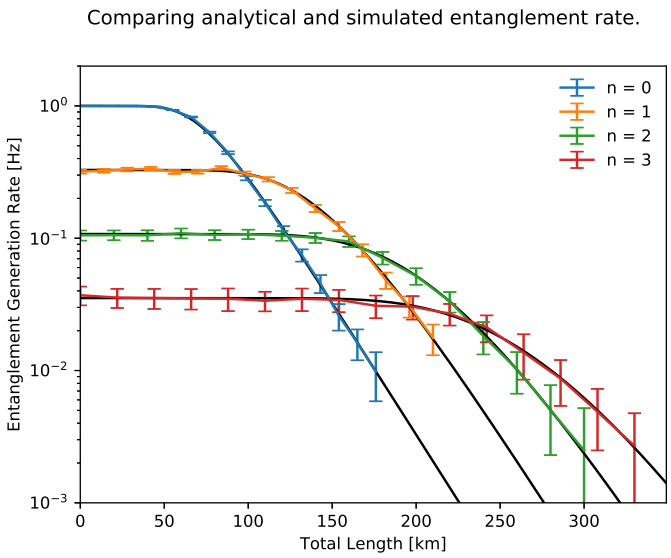

Figure 4.1: Entanglement distribution rate in Hz for $m = 100$ modes and varied for $0 \leq n \leq 3$ repeater nodes. The black lines are the respective analytical curves. The rate of the source is set to 1 Hz.

4.2.3 Results

To compare our simulation with the results from [32] we used the same parameters: $\eta_{mem} = \eta_{d1} = \eta_{d2} = \rho = 0.9$ and $\alpha = 0.2dB/km$.
While Sinclair et al. assume a memory that is able to store multiple qubits in each spectral mode simultaneously, resulting in a really high rate, we limited our simulation to a single photon per spectral mode. However this does not influence the comparability of the models as we can just insert the same rate used in our simulation into the analytical model.
For simplicity the time between attempts was set to 1s, while the maximum rate is achieved for $\Delta t = t_{cycle} = L/(n \times c)$. For the channel lengths considered in the following this would be much larger than $1Hz$.

We see very good agreement between the analytical results and our simulation both when varying the number of elementary links n (see Fig. 4.1) and the number of modes m (see Fig. 4.2).
Our simulation can therefore accurately model this simplest of models for a repeater chain of atomic ensembles.
Since this model does not include any of the interesting noise parameters like dark counts, we will now move on to a more sophisticated analytical model including these parameters and investigate whether our simulation can also reliably replicate those results.

4.3 Validation of more sophisticated model

Here we will briefly go over some important results presented by Guha et al. in [46] presenting a model that now also includes dark counts and imperfect detectors. We will again mention some details about the used repeater protocol and then go over the main results for perfect photon pair sources. Finally we will get into imperfect sources with the probability to emit multiple photon pairs and how the introduced multi-photon errors influence the secret key rate in the next section.

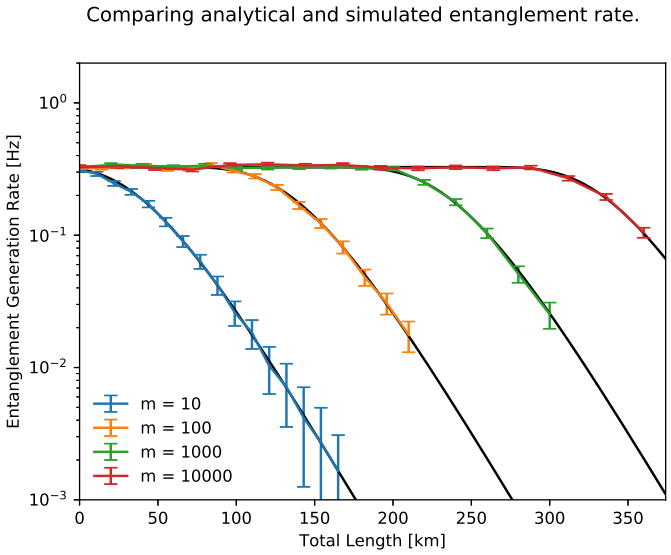

Figure 4.2: Entanglement distribution rate in Hz for $n = 1$ repeater nodes and varied over the number of modes m for $m = 10$, $m = 100$, $m = 1000$ and $m = 10000$. The black lines are the respective analytical curves. The rate of the source is set to 1 Hz.

4.3.1 Setup

The setup used is essentially the same as in the previous paper, where a double-click scheme is employed and the chain is built up from elementary links containing two sources of entangled photon pairs, two quantum memories and a central station with a beam splitter and detectors to perform the linear optic BSM. Entanglement is swapped simultaneously on all repeater nodes with linear optical BSMs and a universal synchronized clock is assumed.

4.3.2 Analytical results for perfect photon pair source

We will now give a brief overview of the main analytical results of Guha et al. used to verify our setup. All detailed derivations can be found in the paper [46] and here we will instead try to give some intuition about why the equations make sense. First the full expression is presented and we will then go over all the different factors one by one.
For a perfect photon pair source [46] derives an exact expression for the secret-key rate achievable by this setup. It is given by:

$$R = P_1 P_{succ} R_2(Q_{n+1})/2T_q \quad \text{secret-key bits/s} \tag{4.6}$$

with P_1 the sift probability, P_{succ} the overall success probability of the connection, $R_2(Q) = 1 + 2(1-Q)log_2(1-Q) + 2Qlog_2(Q)$ the secret-key rate of BB84 in bits per sifted symbol, Q the error probability of the sifted bit and T_q^{-1} the clock rate of the system. The factor of 2 in the denominator accounts for the probability that Alice and Bob use the same basis choice.

The sift probability P_1,

$$P_1 = (q_1 + q_2 + q_3)^2 \tag{4.7}$$

is the probability, that neither Alice nor Bob gets zero clicks on their detectors, given they both measure in the same basis. This is important as we again use a double-click scheme with time-bin encoding. Here $q_1 = (1 - P_d)A_d$, $q_2 = (1 - A_d)P_d$, $q_3 = P_d A_d$, $A_d = \eta_d + (1 - \eta_d)P_d$ and η_d, P_d are detector efficiency and dark count probability respectively. This can be interpreted as follows:

- q_1 is the probability that the outcome is detected correctly.
  $|01\rangle$ as (no-click, click) and $|10\rangle$ as (click, no-click)
- q_2 is the probability that the noisy detector 'flips' the outcome.
  $|01\rangle$ as (click, no-click) and vice versa
- q_3 is the probability that, no matter whether the state is $|01\rangle$ or $|10\rangle$, the noisy detector generates (click, click).

All three probabilities are symmetric in the inputs and each half of the state has exactly one photon, therefore the probability of a successful sift is simply the probability of both Alice and Bob getting one of the above three events (no-flip, flip, double-click) as described in eq. (4.7).

For the overall success probability P_{succ} [46] derive an expression similar to eq. (4.4),

$$P_{succ} = (4s)^{2n-1}[1-(1-4s_1)^m]^{2n} \sim P^{N-1}_{SuccessfulSwap} \times P^N_{link} \tag{4.8}$$

where m the number of modes, $2n$ the number of elementary links and $4s$, $4s_1$ success probabilities of the swap and the elementary link BSM (per mode) respectively. It is worth noting that the swap probability now actually depends on the quantum state which is being tracked.

The QBER is recursively calculated to be

$$Q_i = \frac{1}{2}\left(1 - \frac{t_d}{t_r}(t_r t_e)^{2^{i-1}}\right) \tag{4.9}$$

where t_e, t_r, t_d are functions of the loss-noise parameters of the detectors in the elementary link, repeater nodes and end node detectors respectively. For zero dark-count probability $P_x = 0$ they become $t_x = 1$, while they can still have imperfect detection efficiency $\eta_x \neq 1$. For the exact derivation, which requires solving a variant of the chaotic logistic map, we again point to the original paper [46].

Qualitatively the result is easy to understand: In this very simple model the only quantum bit error comes from the detectors. Detection efficiency will not lead to a flipped bit, but only to a reduced rate, as some successful events are just not detected. Dark counts however can flip the outcome of a detector in the sense as above (e.g. $|01\rangle$ detected as $|10\rangle$). This leads to a different end-to-end state being heralded as a success and therefore introduces quantum bit error. In the repeater chain there are N midpoint BSMs, $N-1$ swapping BSMs and one end node detection combining to the term $(t_d/t_r)(t_r t_e)^{2^{i-1}}$ in the recursion. The factor $\frac{1}{2}$ accounts for the maximum QBER being $\frac{1}{2}$, indicating complete randomness of Alice and Bobs measurement results.

This model produces a curve for the secret key rate with three distinct region as shown and in Fig. 4.3 and explained in section 3.2.

4.3.3 Simulation results for perfect photon pair source

In the following we will investigate how well our simulation results agree with the analytical expression for the secret-key rate (4.6) presented above.
This investigation was done by Julian Rabbie using the same simulation and can be found in his thesis [38]. Fig. 4.4 shows the results for different numbers of elementary links N.

We see that there is good agreement between the analytical results and the simulation data for all N. While the elementary link stays below the theoretical capacity bound for all lengths, with a single repeater the secret-key rate crosses the bound after $\sim 250km$.
Once again we demonstrate that our simulation can accurately reproduce the analytical results for a perfect photon pair source, even when dark counts and detector efficiencies

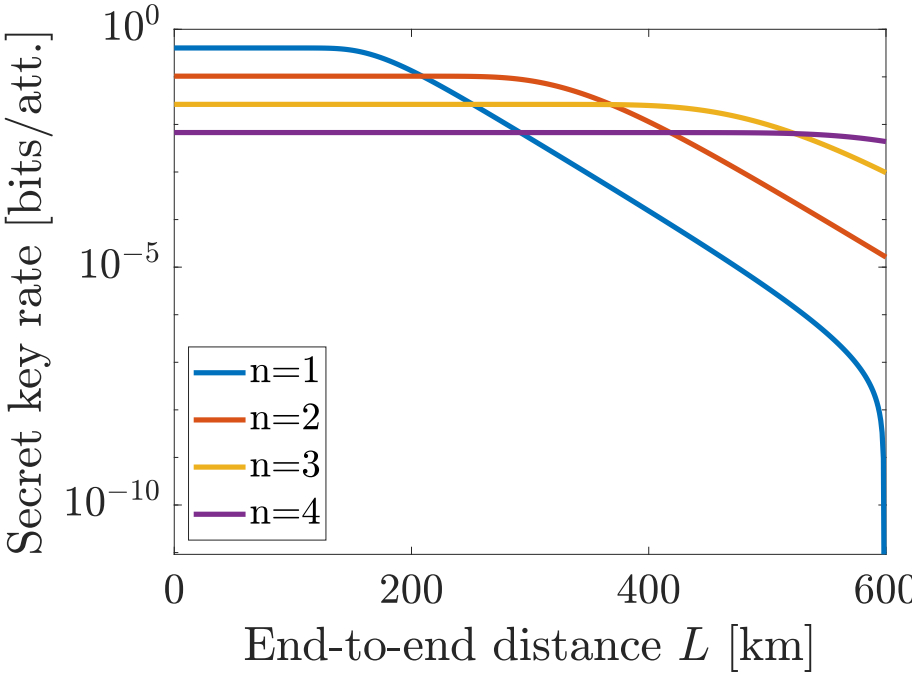

Figure 4.3: Analytical calculation of the secret key rate as in [46] for different numbers of elementary links N. Qualitatively each curve has a similar shape consisting of three distinct regions as described in section 3.2. This is the purely analytical model without inclusion of multi-photon emission.

are included.
This concludes our verification of analytical results, as we now want to start moving beyond analytical predictions and investigate our implementation of multi-photon errors.

4.4 Validation of multi-pair implementation

In order to validate our full implementation we turn to the numerical analysis done by Guha et al. [46]. As shown in Fig. 3.1 they analyse the effect of different multi-photon emission probabilities on the secret key rate. Since our source (see section 3.5.1) allows us to input the individual emission probabilities $p(n)$, where n is the number of emitted pairs, we take a couple of values for $p(2)$ and compare our simulation to the plots in [46]. In the current implementation the computation time required to create the necessary data increases with the number of attempts needed for end-to-end entanglement. Therefore we limit our analysis to the regime where the elementary link still provides near-deterministic entanglement generation. This way we get a good idea whether our implementation of the multi-photon POVMs is correct while the loss and dark counts responsible for the exponential decrease in rate have already been validated in the previous section. From Fig. 3.1 it is clear that even for this region we can expect significant changes in behavior when introducing multi-pair emission.

For our comparison we use the same parameters that are specified in the caption of Fig. 3.1. Each datapoint represents 1000 successful end node measurements.

We first start by using a source which has no probability of emitting a second photon pair as shown in Fig. 4.5. In analogy to Guha et al. we set the other probabilities to $p(1) = 0.9$, $p(2) = p(3) = 0$ and $p(0) = 1 - p(1) - p(2)$.

We then start turning on the two-pair emission probability and set $p(2) = 0.013$ in Fig. 4.6.

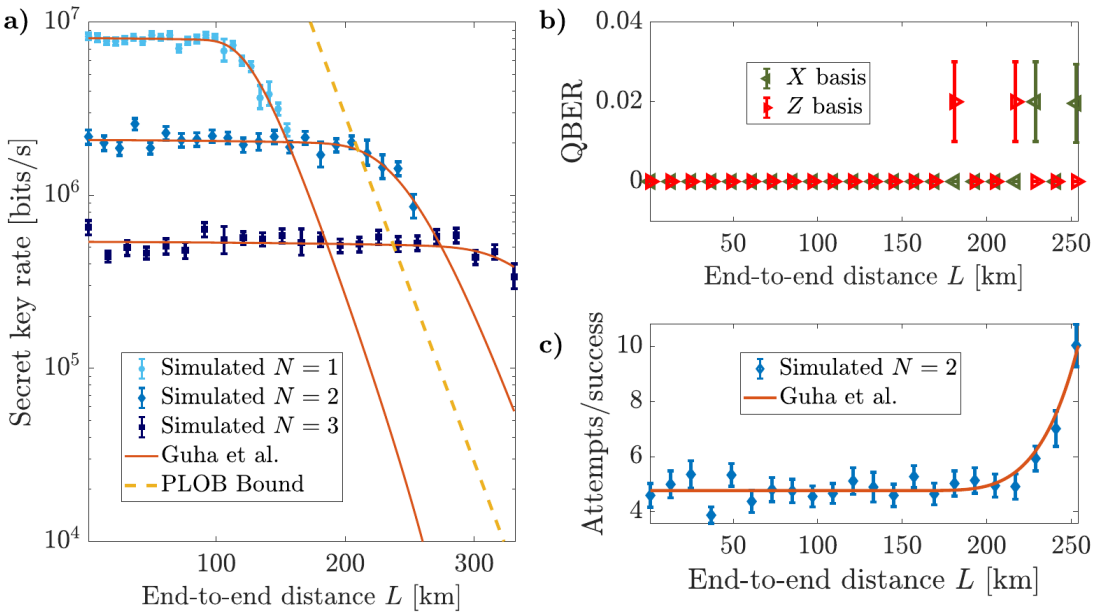

Figure 4.4: Validation of our simulation model against the more sophisticated analytical model of Guha et al. [46] performed by J. Rabbie [38]. Each datapoint corresponds to only 100 successful measurement outcomes. **a)** Secret key rate for a single elementary link (N = 1), one (N = 2) and two repeaters (N = 3), plotted with the theoretical PLOB bound [64]. The error bars represent minimal and maximal values calculated from the QBER. Solid red lines represent the analytic model and dots the data obtained from our simulation. We see good agreement between the two for all values of N. **b)** QBER for N = 2. While the secret key rate is constant both QBERs remain zero since the model assumes a perfect photon pair source. Once the elementary link success probability starts to become smaller than 1 dark counts start to give a small amount of false positives leading to a non-zero QBER. **c)** For the same reason the number of required attempts needed to successfully generate entanglement increases exponentially beyond a range of 200km Qualitatively similar behavior for QBER and number of attempts can be observed for other values of N. The parameters used to generate this are an attenuation coefficient $\alpha = 0.2$dB/km, a source with frequency $f = 2$MHz and perfect single pair emission ($p(1) = 1$, $p(0) = p(2) = p(3) = 0$), $M = 1000$ spectral modes, dark count probability $P_{dark} = 3 \cdot 10^{-5}$, detector efficiency $\eta_{det} = 0.9$, visibility $v = 1$ and fixed memory efficiency $\eta_{mem} = 0.8$.

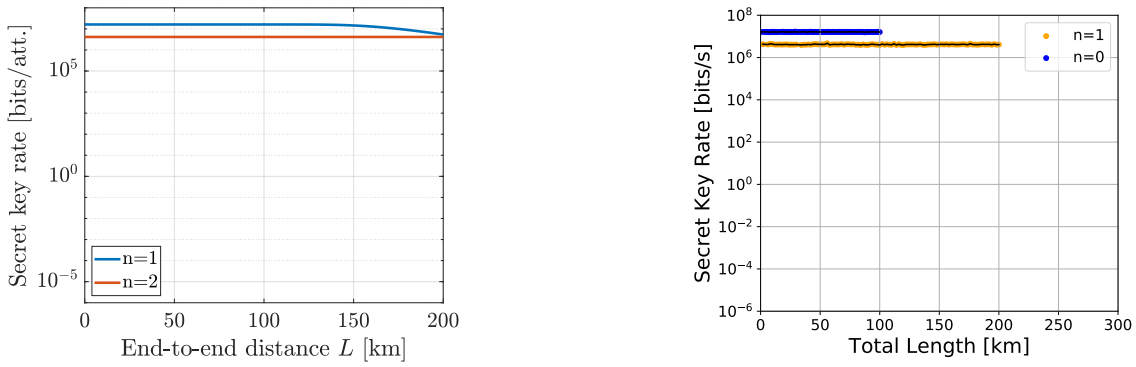

Figure 4.5: Comparison of the analytical secret key rate obtained in [46] (left) and our simulation for two-pair emission probability $p(2) = 0$. **Left:** Analytical results for elementary link (blue) and single repeater (red). **Right:** Simulation results for elementary link (blue) and single repeater (orange). The black line is the secret key rate calculated from a linear fit to the QBER in both basis and is given as a visual aid. For the simulated range our simulation agrees perfectly with the analytical model. Each datapoint represents 1000 successful end node measurements.

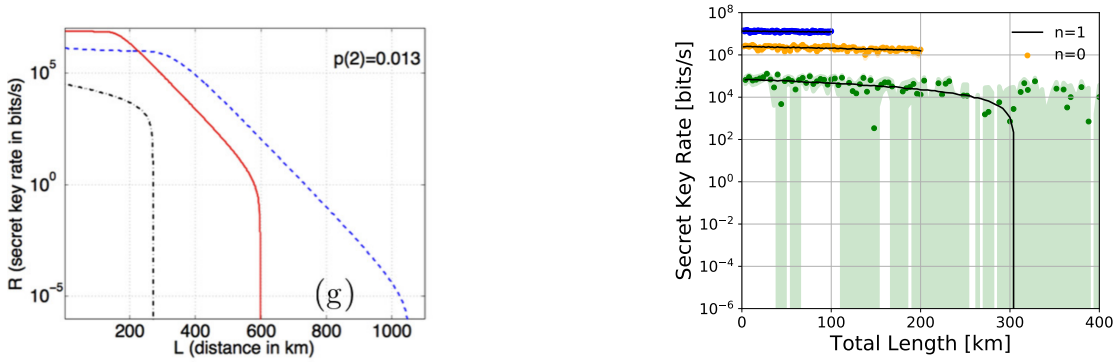

Figure 4.6: Comparison of the numerical secret key rate obtained in [46] (left) and our simulation for two-pair emission probability $p(2) = 0.013$. **Left:** Numerical results for elementary link (red), single repeater (dashed-blue) and three repeaters (dashed-black). **Right:** Simulation results for elementary link (blue),single repeater (orange) and three repeaters (green). The black line is the secret key rate calculated from a linear fit to the QBER in both basis and is given as a visual aid. For the simulated range our simulation agrees perfectly with the analytical model. For the three repeater experiment the fit might seem like it does not agree with the datapoints, however most datapoints in the region $\sim 280 - 400km$ are at 0 and therefore not visible in the logarithmic plot shown. This also shows that our simulation is able to simulate repeater chains for distances of hundreds of kilometers efficiently. Each datapoint represents 1000 successful end node measurements.

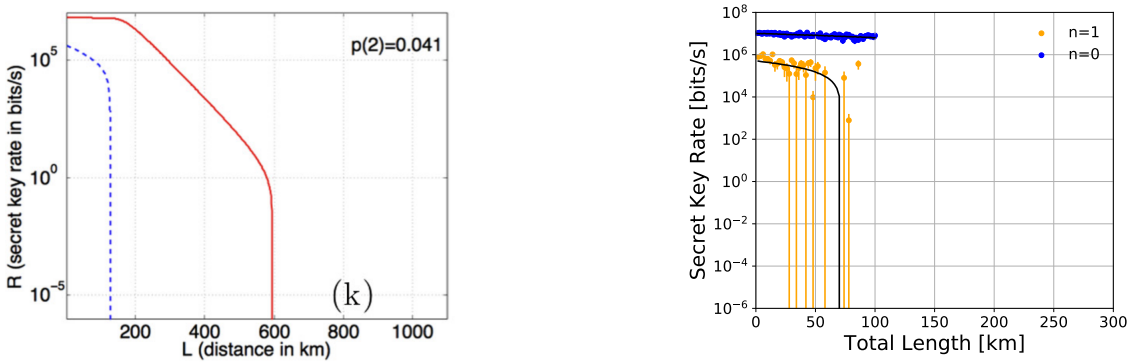

Figure 4.7: Comparison of the numerical secret key rate obtained in [46] (left) and our simulation for two-pair emission probability $p(2) = 0.041$ (right). **Left:** Numerical results for elementary link (red) and single repeater (blue). **Right:** Simulation results for elementary link (blue) and single repeater (orange). The error bars indicate minimal and maximal secret key rate calculated from the standard deviation of the measured QBER. For some datapoints the maximal QBER passes the threshold at which the secret key rate drops to zero. The black line is the secret key rate calculated from a linear fit to the QBER in both basis and is given as a visual aid. Qualitatively our results agree with the numerical calculation. However our rate drops to zero earlier (at $\approx$ 75km instead of $\approx$ 125km). This is caused by the fact that we run the entire experiment with noisy end node detectors, therefore our results have a slightly higher QBER than the numerical investigation which calculated the QBER directly from the obtained end state. This results in our simulation crossing the threshold for zero secret key slightly earlier. Each datapoint represents 1000 successful end node measurements.

Finally we set $p(2) = 0.41$ and show the results in Fig. 4.7.

In all cases we see good agreement between our simulation and the analysis by Guha et al. [46]. However we run a full QKD experiment and obtain slightly higher QBER in both bases due to our noisy end node detection compared to the numerical results where the QBER is directly calculated from the end-to-end state.

We can thus conclude that our simulation can correctly reproduce all previous analytical

and numerical work done on atomic ensemble based repeater architectures. Figure 4.6 also shows that our simulation is capable of simulating repeater chains of hundreds of kilometers efficiently as the 1000 successful measurements took only about 10 core-hours per simulated distance.

Let us now move beyond those limits and explore the full potential of our simulation by analyzing a number of previously neglected noise parameters in the next chapter.

Chapter 5

Analysis of different noise parameters

5.1 Introduction

So far we have explained the details of our simulation and tested it against available analytical models. The aim of this chapter is to now use the additional capabilities of our simulation to investigate various noise parameters previously excluded from analysis.

To demonstrate this we will first run our simulation with the same parameters as detailed in the caption of Fig. 3.1 for a source with $p(0) = 0.1$ and $p(1) = 0.9$ and then investigate the influence of the different noise parameters on the results.

Fig. 5.1 shows the results of that simulation replicating the analytical model [46]. We show the case of zero and one repeater node for an elementary link length of up to 100km. This is the regime where elementary link entanglement generation happens deterministically. Therefore both the elementary link and the single repeater exhibit constant secret key rate and zero QBER in both basis.

This will be our starting point for first analyzing multi-photon emission, time-dependent memory noise and photon distinguishability one-by-one before showing the accumulated difference of our simulation over the analytical model.

5.2 Multi-photon emission

We have already mentioned the importance of multi-photon emission a couple of times in this thesis. Let us now have a closer look at how it affects the secret key rate.

Figure 5.2 shows the same simulation as before but now with a non-zero probability of emitting two-photon pairs of $p(2) = 0.013$.

Already for the elementary link we see a difference compared to the purely analytical model without multi-photon emission. The second photon pair that can be emitted will introduce false positives at the midpoint BSM such introducing errors in both X and Z basis resulting in a non-zero QBER. These false positives are easy to understand as the detectors for the midpoint BSM can not resolve different photon numbers and can therefore not discern between measuring one or multiple photons. Thus they will mistake a two-photon measurement for a successful one-photon detection and wrongly herald success. However the Rate still stays constant which is at least qualitatively captured by the analytical model.

The difference to the analytical model becomes more drastic in the single repeater scenario. Not only does the QBER in both basis increase again due to the additional BSMs introducing further probability of false positive measurements, but now also the secret key rate starts to drop slightly.

The effect is even more drastic for higher $p(2)$ as can be seen in Fig. 4.7 where the rate drops to zero because of the introduced QBER.

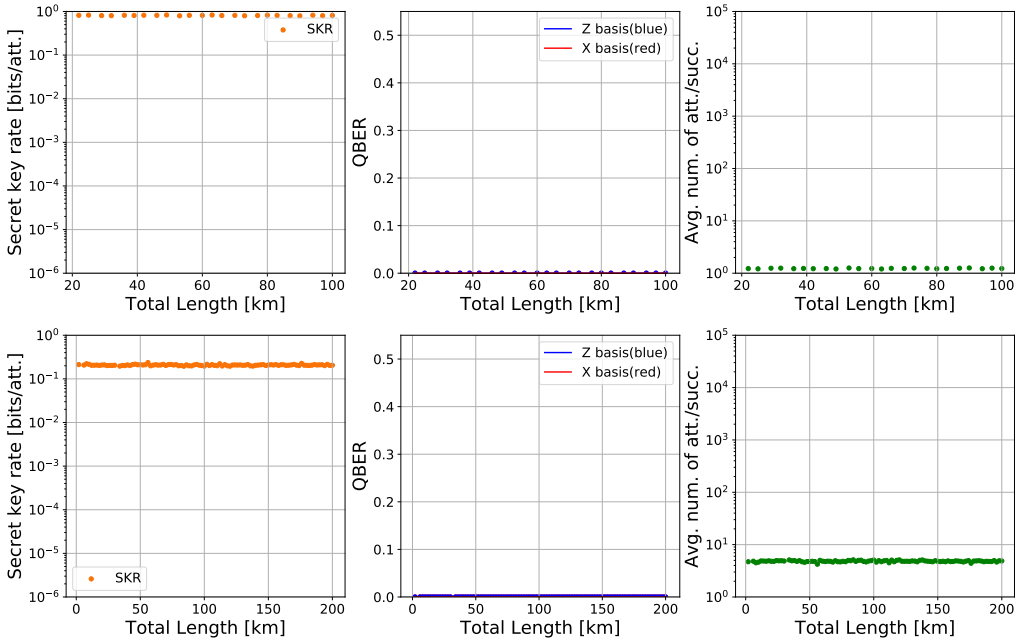

Figure 5.1: Simulation of the analytical model in [46] without any additional noise parameters for zero (top) and one (bottom) repeater for elementary link length up to 100km. The secret key rate (left) stays constant for both scenarios as the elementary link has success probability 1. In both cases the QBER (middle) in both X and Z basis is 0 and the reduced secret key rate in the one repeater scenario is caused by the increased number of attempts (right) necessary to obtain a successful measurement. This is due to the probabilistic swap at the repeater node.

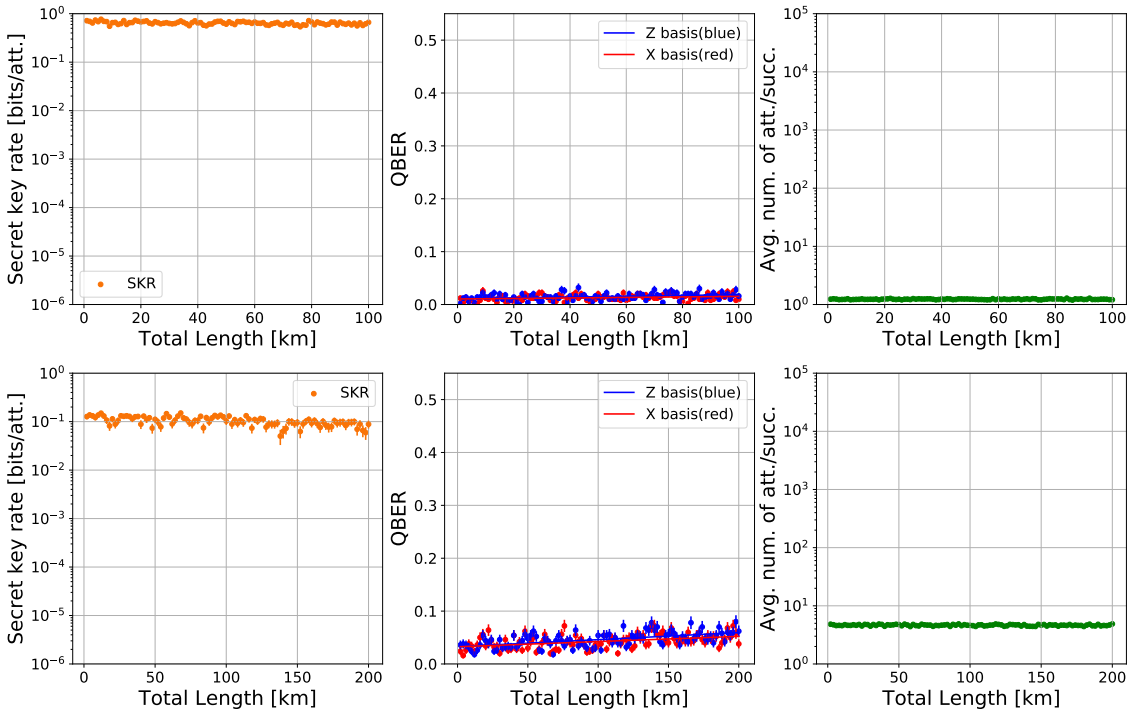

Figure 5.2: Simulation of the analytical model in [46] with two-pair emission probability $p(2) = 0.013$ for zero (top) and one (bottom) repeater. Both scenarios were simulated up to an elementary link length of 100km. Compared to the analytical model the secret key rate (left) is slightly reduced for the elementary link while for the single repeater it now drops slightly. In both cases the QBER (middle) in both X and Z basis is now non-zero. For the single repeater this effect is stronger since more BSMs are involved.

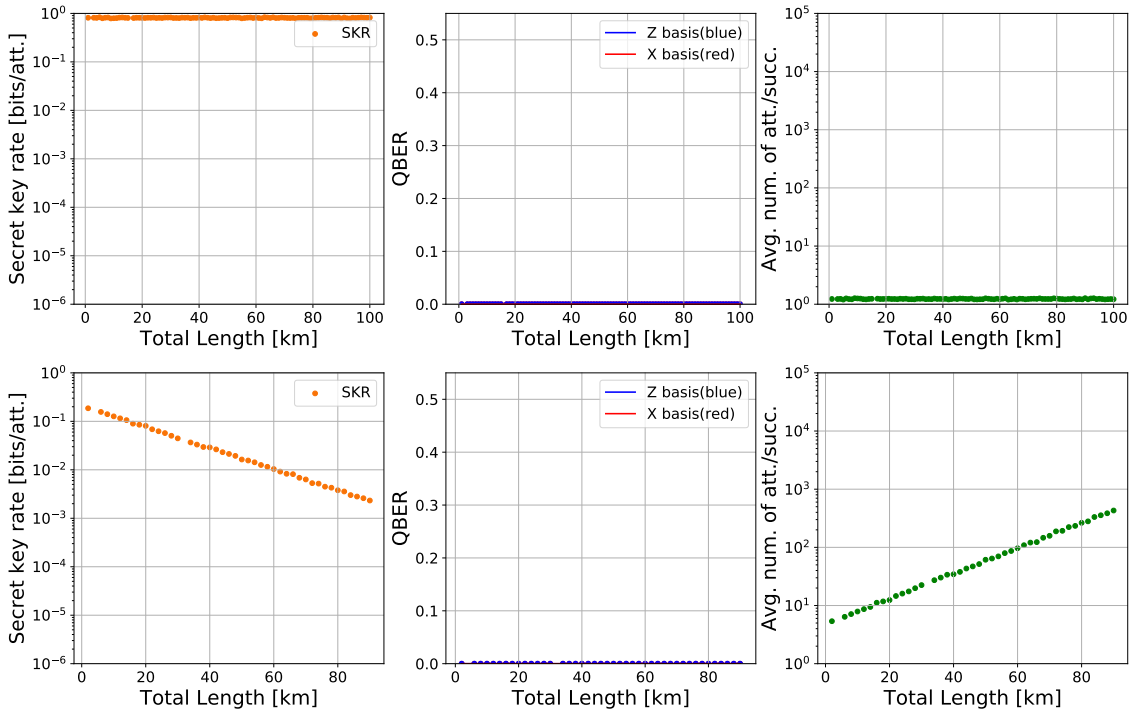

Figure 5.3: Simulation of the analytical model in [46] with time-dependent memory efficiency and a memory coherence time $T_c = 100\mu s$ for zero (top) and one (bottom) repeater. The elementary link is simulated for up to 100km while the single repeater simulation was stopped after only 90km because the exponentially dropping rate leads to exponentially increasing computation time. Compared to the analytical model there is no change for the elementary link as we measure qubits directly while for the single repeater the secret key rate (left) now drops exponentially due to the increasing average number of attempts (right) caused by the photon loss. In both cases the QBER (middle) in both X and Z basis stays unchanged.

5.3 Time-dependent memory efficiency

Since NetSquid is a discrete event simulator is inherently well suited to investigate effects related to time. In current analytical work memory efficiency is always assumed to have a constant value η_{mem}. However for real quantum memories such as AFC based memories (see 2.8.2) this efficiency decreases exponentially with time.

$$\eta_{mem} \rightarrow \eta_{AFC}(t) = \eta_{AFC}(0)e^{-t/T_c} \tag{5.1}$$

We therefore expect the average number of attempts per measurement success to increase exponentially as soon as we introduce one or more repeaters. Since in our QKD experiment we measure qubits directly at the end nodes they are not stored in the memory for the elementary link scenario and we expect the secret key rate to stay the same. This behavior can nicely be observed in Fig. 5.3.

5.4 Photon distinguishability / visibility

Bell state measurements are a fundamental part of any repeater architecture. In Chapter 2 we already discussed that a BSM performed with linear optics has a maximum success probability of 50%. However even when a measurement was successful the quality of the measurement / swap also depends on whether or not the photons arriving at the beam splitter were indistinguishable or not. Any photons arriving at the beam splitter 3.3 should be identical in all degrees of freedom, i.e. frequency, spectral shape, arrival time, phase

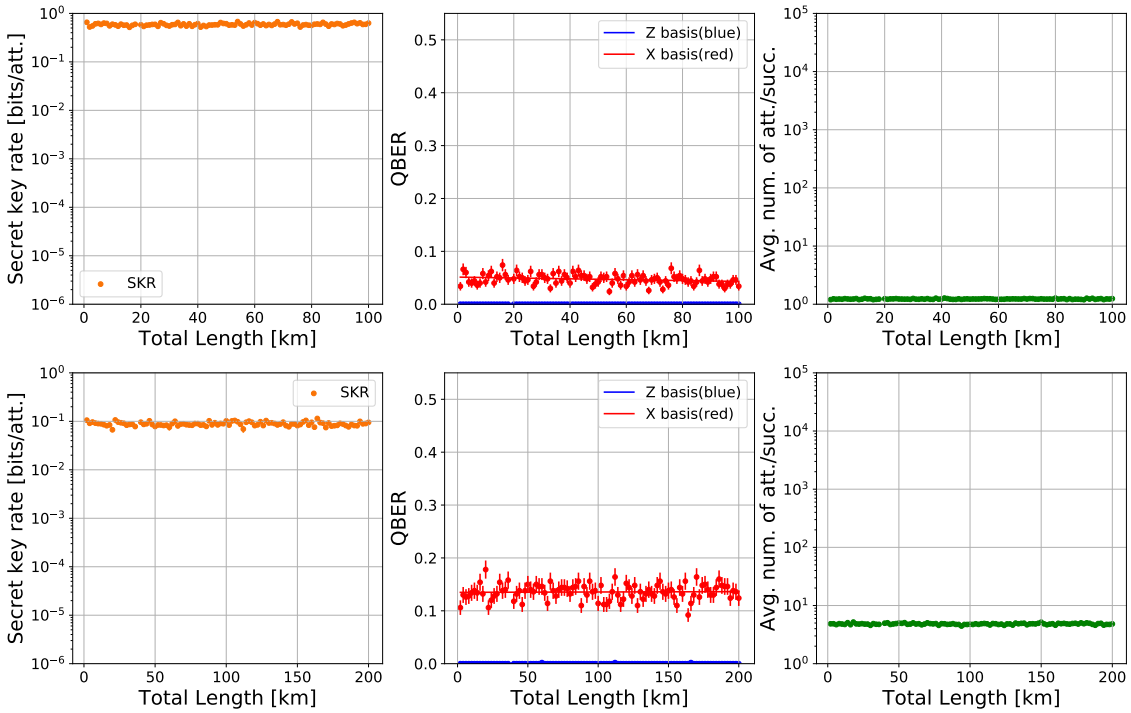

Figure 5.4: Simulation of the analytical model in [46] with imperfect photon indistinguishability / visibility $\nu = 0.9$ for zero (top) and one (bottom) repeater. The average number of attempts for a successful measurement (right) remains unchanged. Due to the loss of phase coherence introduced by the distinguishability of the photons the QBER (middle) in X basis increases significantly for both scenarios. This is results in a corresponding drop in secret key rate (left).

and polarization, in order to be free of any 'which-way' information. If this is not the case, one could (partially) determine where the photon came from, which degrades the quality of the projected entangled state.

The effects of decreasing the visibility from $\nu = 1$ (perfectly indistinguishable photons) to $\nu = 0.9$ are shown in Figure 5.4. We can see a clear drop in the absolute value of the secret key rate and larger statistical uncertainty of our datapoints. This is caused by a large increase of QBER in the X basis. The distinguishability of the incoming photons causes a loss of phase coherence which will not show up for measurements in the Z basis but will introduce errors in the X basis. The same would hold for a measurement in the Y basis. If we were to perform our BB84 protocol by measuring in X and Y instead of X and Z we would not be able to extract any key since the QBER in both basis would be above the threshold. The average number of attempts per successful measurement stays unchanged thus also confirming that non-unit visibility ν just introduces false positives.

5.5 Total improvement over analytical models

To conclude this chapter we now have a look at the cumulative effects of all previously mentioned sources of noise. Figure 5.5 shows our simulation results for elementary link and single repeater.

Figure 5.6 shows the secret key rate of a single repeater experiment for the same parameters and compares them to the analytical model of Guha et al. [46]. For the elementary link the difference between the analytical model and the simulation is only a slight decrease in rate due to the increased QBER caused by visibility and multi-photon emission.

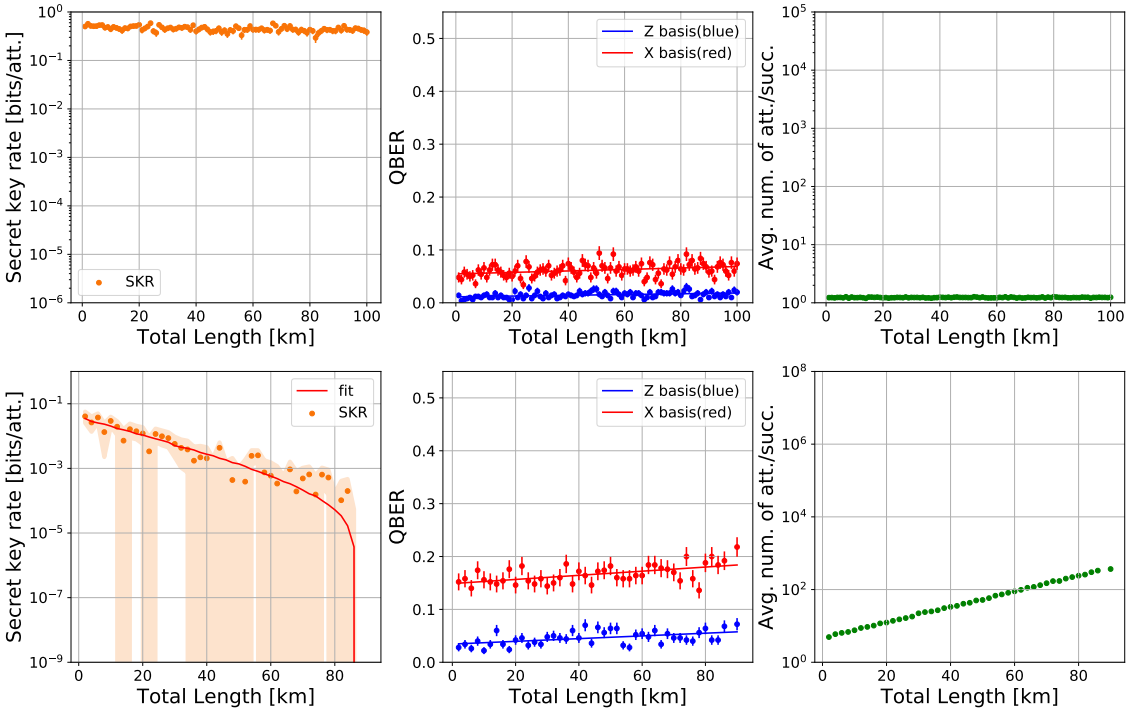

Figure 5.5: Simulation of the analytical model in [46] with imperfect photon pair source with $p(2) = 0.013$, time-dependent memory noise with $T_c = 100\mu s$ and imperfect photon indistinguishability / visibility $\nu = 0.9$ for zero (top) and one (bottom) repeater. We see a drop in rate caused by the increased QBER for the elementary link compared to Fig. 5.1. For the single repeater we see both and exponential increase in number of attempts (green) as well as an increase of QBER in both basis leading to a significantly lower rate. For a direct comparison to the analytical model see Fig 5.6.

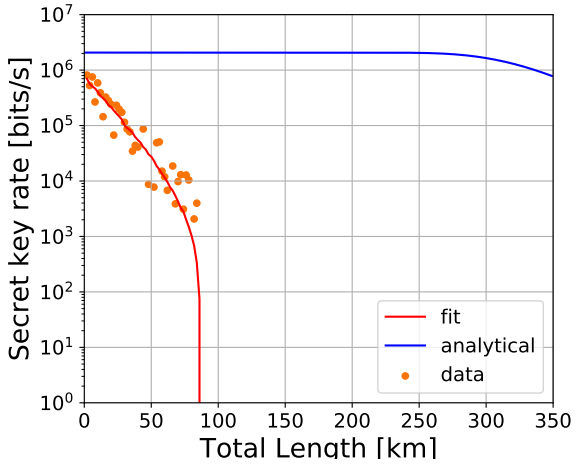

Figure 5.6: Direct comparison of single repeater secret key rate calculated from the analytical model of Guha et al. (blue) and obtained from our simulation including all additional noise parameters as in Fig 5.5. It is clear that our simulation provides a inherently larger amount of information about the physical system. Any meaningful future scalability analysis of atomic ensemble system should such use our simulation over the analytical model.

However as soon as we include a single repeater the behavior changes drastically. While the analytical model predicts the rate to stay constant over more than 200km, our simulation shows that the rate in fact drops to zero at only $\approx$ 90km. Already at 20km the simulated rate is an order of magnitude lower than predicted by the analytical model.

This clearly shows that there is a large gain in information by using our simulation. Any meaningful scalability analysis of atomic ensemble architectures needs an accurate way of including such significant sources of noise. Our simulation offers an efficient way for such an analysis while at the same time offering absolute modularity. This will be demonstrated in the next chapter, where we compare different setups using different components to showcase the flexibility of the simulation.

Chapter 6

Comparison of different QIA nodes

6.1 Introduction

Within the Quantum Internet Alliance there are currently a number of experimental efforts concentrating on realizing the hardware needed for a repeater protocol using atomic ensembles and linear optics. They all fall within the class of multiplexed protocols, but still use slightly different hardware and setups. There have been significant improvements in performance over the last years e.g. reported memory efficiencies of over 70% [24], storage times of the order of seconds [23] or close unit input-output fidelity $F_{IO} \approx 93 \pm 2\%$ of the retrieved photons [45] Still, all of the groups are working on the individual components and none of them have a complete repeater experiment as of the time of writing this thesis.
It is therefore extremely interesting to take the parameters of the individual components, plug them into our simulation and investigate how the actual experimental hardware would perform in a repeater experiment.
This will be the goal of this chapter. We will start by giving a short overview of the differences of the individual setups outlining their core differences and then present the comparison for a number of different scenarios.

6.2 QIA Nodes

Currently four groups within QIA are working on atomic ensemble based quantum repeaters:

1. A group at QuTech in **Delft** lead by Wolfgang Tittel,
2. one at University of **Geneva** lead by Mikael Afzelius,
3. one at ICFO in **Barcelona** lead by Hugue de Riedmatten,
4. and a group at Sorbonne University in **Paris** lead my Julien Laurat.

We will now briefly describe the different protocols and hardware they use before showing the results of our simulation.

6.2.1 Delft

The group in Delft employs an entanglement scheme based on spectral multiplexing using AFC quantum memories and SPDC sources. We already described the setup and used components at the end of Chapter 2.
The benefit of this particular hardware is its multiplexing capability. However the memory

efficiency is currently still very low. It is important to point out that this is a **double-click** protocol (e.g. based on successful detection of two photons at the BSM).

6.2.2 Geneva

In Geneva they use a modified version of the original DLCZ protocol (see section 2.4), where source and memory are one component, using solid-state ensembles [22]. This novel approach makes the protocol inherently multi-mode. They create an AFC on the optical transition of their DLCZ level scheme to employ inhomogeneous dephasing control to counteract the weak oscillator strength of their rare-earth ions. This would otherwise lead to very low read-out efficiencies. Using an AFC memory and encoding their spin-excitation in a Dicke state (2.24) makes their protocol inherently multimode in time. The foundation for this is that the detection of time-separated Stokes photons leads to distinguishable spin waves, thus resulting in a **temporally multiplexed DLZC scheme** [22] Since the produced photon needs to be converted to telecom wavelength their protocol has large conversion losses. However, these losses can be more easily compensated by the protocol since it only depends on a single photon being detected at the BSM (**single-click** protocol).

6.2.3 Barcelona

In Barcelona they also run a temporally multiplexed DLCZ protocol, however they separate their source (SPDC) and their memory (AFC) [44]. This way they aim to reach a large number of total modes by combining temporal, spectral and spatial multiplexing. They are currently still experimenting with different memory protocols. In addition to the regular AFC protocol described in section 2.8.2 they also experiment with so called **on-demand** AFC memories. This is a slightly modified version where instead of having just two levels one adds an extra spin level, between the excited and the ground state, to the protocol to obtain a so called **lambda-scheme**. This is motivated by the fact that coherence times of the excited level used for storage are usually quite small [23]. The coherence time of the spin-level is significantly larger thus allowing for longer storage times.

The memory protocol then works as follows. Just like in the original protocol a comb is created on the optical transition and the incoming photon is stored in the Dicke state (2.24) where it starts to dephase. After a time $t_1 \geq 0$ the whole state is then pumped to the spin state with a laser pulse. As there is no comb on the spin-level the phase of the stored state is "frozen" while on this level. When one wants to retrieve the state e.g. after retrieving the classical communication from the midpoint the state is pumped back to the excited level. The Dicke state than continues to dephase and rephases after a time $t_2 = t_{rephase} - t_1$ at which point the photon is re-emitted from the memory. The total time on the memory is therefore $t_{storage} = t_1 + t_{spin} + t_2 = t_{rephase} + t_{spin}$, where t_{spin} is the time spent on the spin-level.

This not only allows for longer storage times due to the longer coherence time of the spin-level but also enables on-demand retrieval of the stored photon. By varying t_{spin} the storage time can in principle be set to any desired value. This is also very useful when trying to match temporal modes in neighboring elementary links, as modes can easily spend different times on the memory and are not simply emitted after a fixed time as in the original AFC protocol.

In the following comparison we used the regular two-level AFC memory as storage times of the three-level AFC are still quite low and also to make setups more comparable. However the event-based nature of our simulator makes the simulation of such more complicated time-dependence very simple and this will certainly be part of our future research.

Barcelona has a really flexible setup promising high efficiencies as photons from the source do not need to be frequency converted and also promises very high multiplexing capabilities [44]. Just like Geneva this is a **single-click** protocol.

6.2.4 Paris

The main focus of the Paris group is developing a memory based on **electromagnetically-induced transparency (EIT)** [24]. As of now they have no apparent plan of setting up their own repeater experiment. However it is still interesting to see how their memory would perform in such an experiment. Since the group does not have a source component we had to improvise a little and just substituted the photon pair source with the Delft source as their memory also requires an encoding equivalent to time-bin encoding. [24]. This choice is somehow arbitrary as the EIT memory has quite different restrictions than an AFC based memory, e.g. due to the extremely narrow bandwith of the EIT memory no spectral multiplexing is possible. Nonetheless we think that this very interesting component technology should be investigated and integrating it is a nice way to demonstrate the modularity and flexibility of our simulation. Another important difference is that the decay in efficiency over time of the EIT memory is gaussian instead of exponential [1].

6.3 Comparison of elementary links experiments

To compare the different setups we asked each of the four groups to submit three different sets of parameters:

1. Already measured in the laboratory now (**measured 2020**).
2. Expected to achieve in the laboratory this year (**expected 2020**).
3. Projected to achieve three years from now (**projected 2023**).

The full list of used parameters with a short description of how they are used can be found in Appendix A. In this section we will start by comparing how the different parameter sets perform on a single elementary link. We will first investigate the two DLCZ-like single-click protocols Barcelona (Fig. 6.1) and Geneva (Fig. 6.2) and then present the two double-click protocols Delft (Fig. 6.3) and Paris (Fig. 6.4) that follow the setup presented in section 2.7.

It is worth pointing out that these are two conceptually quite different approaches that are differently affected by noise parameters. For the physical implementation refer to section 2.4, 2.7 and for the implementational differences see Chapter 3. In particular note the differences between presence-absence (corresponding to single-click protocols) and time-bin encoding (corresponding to double-click protocols).

Figures 6.1 - 6.4 show nicely that our simulation is able to simulate all four different repeater architectures. All protocols promise increases in achievable rate of several orders of magnitude over the next three years. The rates here are given in bits per entanglement attempt, thus if one would be interested in the rate in bits per second one would have to multiply this with the actual rate of the source which ranges from 10^4 to 10^8 Hz but also depends on e.g. the pump power of the laser.

It is nice to observe the difference between the single- and double-click protocol. Comparing for example the expected and projected performance of the Delft and the Geneva protocol in Figures 6.3 and 6.2 we see very similar rates from 10^{-2} to 10^{-4} and 10^{-1} to 10^{-3} for expected and projected respectively. However, this same drops happens over 100km in

[1] From private correspondence with F. Hoffet from the Paris group.

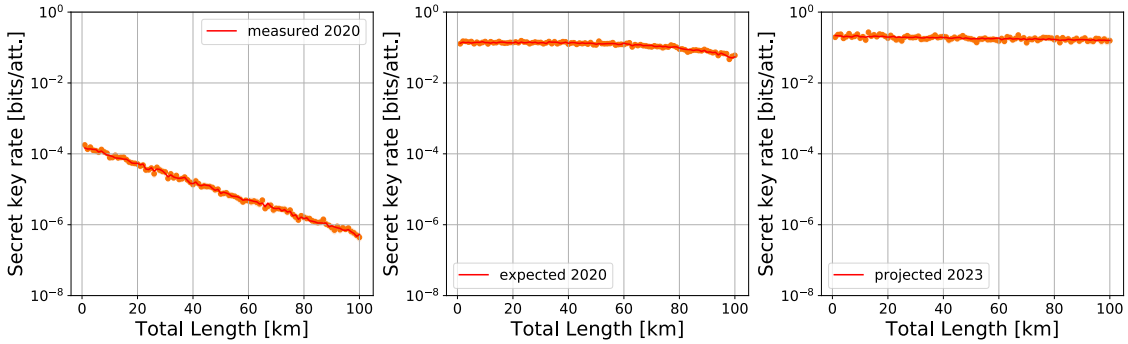

Figure 6.1: **Barcelona:** Secret key rate generated over an elementary link for up to 100km. The secret key rate is given in bits per entanglement attempt. Within this year the expected parameters increase the achievable rate by several orders of magnitude. This is caused by massively increasing the amount of multiplexing and various efficiencies. In three years the submitted parameters achieve deterministic entanglement generation over more than 100km. It is worth noting that it is not clear how such optimistic parameters are to be reached in such a short time.

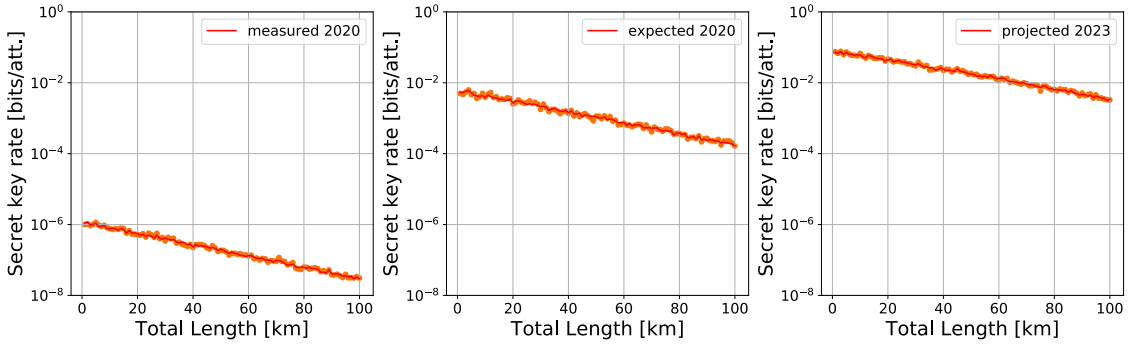

Figure 6.2: **Geneva:** Secret key rate generated over an elementary link for up to 100km. The secret key rate is given in bits per entanglement attempt. Within this year the expected parameters increase the achievable rate by several orders of magnitude. This is caused by increasing the amount of multiplexing and greatly improving various efficiencies. Within three years the rate is projected to increase another order of magnitude.

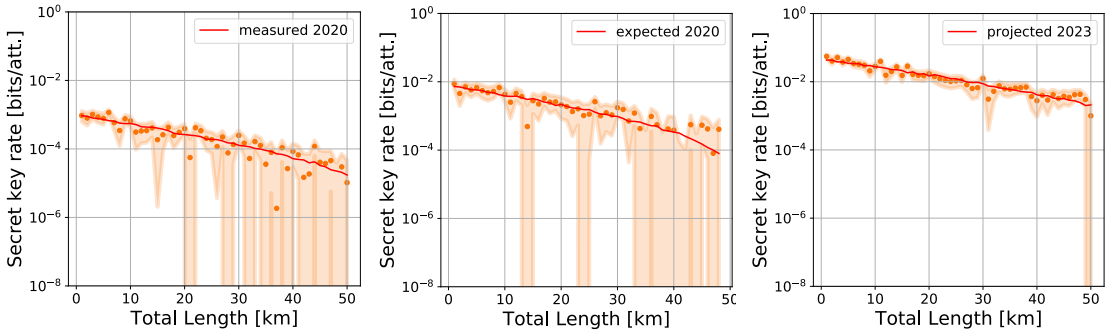

Figure 6.3: **Delft:** Secret key rate generated over an elementary link for up to 50km. The secret key rate is given in bits per entanglement attempt. Within this year the expected parameters increase the achievable rate by approximately one order of magnitude. This is caused by slightly increasing the amount of multiplexing and various efficiencies. Within three years the rate is projected to increase another order of magnitude. It is worth noting that for the leftmost plot the number of modes is 1 as this group is the only one taking into account that the midpoint detectors can limit the amount of multiplexing. This is due to the fact that distinguishing $m > 1$ spectral modes is experimentally not trivial.

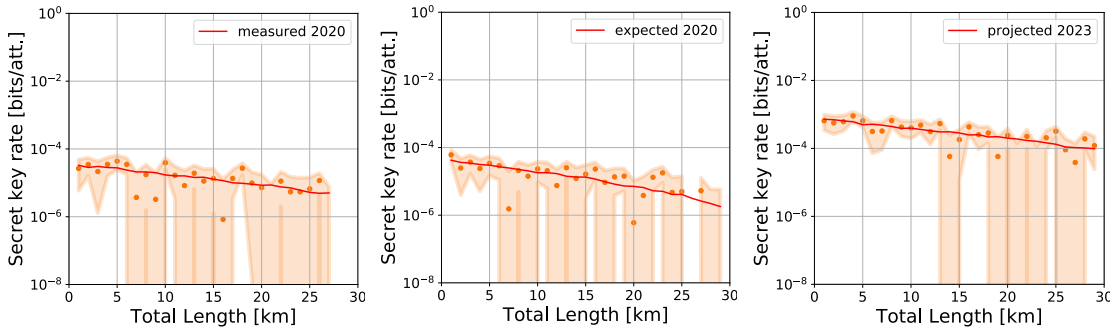

Figure 6.4: **Paris:** Secret key rate generated over an elementary link for up to $\sim$ 25km. The secret key rate is given in bits per entanglement attempt. As this group does not have their own photon pair source we used a dummy source with similar parameters as the one in Delft. They achieve much lower rate than the Delft group as their midpoint detector has severely lower quality, however all data points still exhibit non-zero rate. Since this is a double-click protocol this has an especially large effect on the protocol. It would be interesting to investigate the performance of this memory technology in a more comparable setup.

the Geneva protocol and only 50km in the Delft protocol. This is exactly what we would expect: While the double-click protocol does not require interferometric stability it does rely on the correct detection of two photons instead of one. Therefore the double-click protocol is hit twice as hard by any imperfections in photon transmission and detection thus leading to the same drop in rate in half the distance compared to the single-click protocol.

It is worth pointing out that the simulation of the expected or projected parameter sets of the different groups is not a fair comparison, as the groups submitted vastly different parameter prognoses. For a detailed list of the submitted parameters see Appendix A, but as a quick example let us look at the total number of modes the groups expect to achieve. While the three groups from Delft, Geneva and Paris expect their total number of modes to grow by roughly one order of magnitude (e.g. from 1 to up to 50 modes in Delft) over three years, the group in Barcelona expects to improve this number by two orders of magnitude in just this year alone (from 33 to 1200 modes). It is not clear how such a quick increase is achievable even when combining spectral, temporal and spatial multiplexing. Therefore the simulation data here should not be seen as an exact evaluation of which setup is superior over others in the future but should rather emphasize that our simulation is able to simulate different protocols with different components and parameters accurately.

6.4 Comparison of single-repeater experiments

After having investigated the performance over elementary links we are now interested in what happens when we add a repeater to our experiment. The performance of the single repeater experiment is quite encouraging (especially keeping the high possible repetition rates of real sources in mind). Remembering Chapter 5 and especially Fig. 5.5 however, we were much more affected by the additional imperfections in the single repeater setup. Thus we expect much worse performance. Let us now investigate how real parameters perform in such an experiment.

Qualitatively representative for the performance of all four setups Fig. 6.5 shows the secret key rate generated over a single repeater for the projected parameters in Geneva. It is clear that the accumulated effects of the additional noise parameters in our simulations drop the secret key rate to zero for all distances. Multi-photon emission of the source causes quantum bit errors in both basis, while the non-unit visibility ν further increases the QBER in the X basis as described in 5.4. This pushes the QBER over the threshold

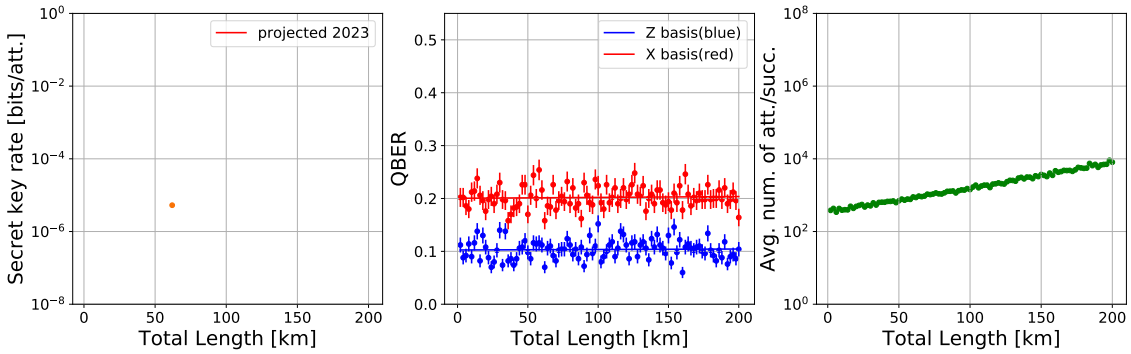

Figure 6.5: Secret key rate generated over a **single repeater** for up to 200km in bits per entanglement attempt. The parameter set shown is from the Geneva group, but qualitatively all four parameter sets show similar behavior. Rate (left) is 0 for all simulated distances due to the high QBER (middle) in both basis while the number of attempts (right) grows exponentially. The rate is zero for all length except for a few statistical outliers resulting in a small non-zero rate calculated from the minimal QBER values for 5 of the 100 data points.

where the secret key rate drops to zero for all length. Similar behavior can be observed for all four setups and all submitted parameter sets.

This teaches us two main lessons:

1. The additional noise profoundly influences the performance of the protocol, not allowing for any secret key being transmitted over a single repeater even for optimistic parameters.

2. Any scalability analysis not taking those noise parameters into account is meaningless for current physical devices.

Additionally it is worth noting that some points are actually close to crossing the threshold of producing non-zero rate. Therefore it might be interesting for further research to actually investigate other figures of merit such as rate of transmission of end-to-end states with certain fidelity.

Chapter 7

Parameter Exploration

7.1 Introduction

After using our simulation to show the performance of certain sets of parameters for different setups we now want to get a glimpse of what we can do with our simulation framework in the future. An important future application will be the exploration of parameter space for different architectures in order to give experimentalists valuable input.

As a first step we start by exploring the scaling with number of modes. The results here will not be very surprising as the scaling is fairly simple, however this is intended as a proof of concept and an outlook onto future research.

7.2 Exploring number of modes

As a first step for our exploration of parameter space, we investigate the number of modes. As we already pointed out in Chapter 2 multiplexing is one of the main advantages of atomic ensemble protocols. Remembering equations (2.20) or (4.4) the probability to distribute entanglement over an elementary link is

$$p_{link} = 1 - (1 - p_{single})^M. \tag{7.1}$$

where M is the number of modes.
It is therefore trivial that the optimum number of modes for maximizing the probability is $m \to \infty$. However it is still interesting to look at the scaling of different protocols.

Figure 7.1 confirms the expected scaling very well. It is also worth observing the significantly better rate of the double-click protocol in the right-most plot.

Figure 7.2 shows another interesting but not surprising detail. If the parameters improve over a certain threshold the secret key rate normalized by the number of modes m has a peak at relatively low values of m for the given length. Increasing the number of modes above this point has diminishing returns. This is also expected since the maximum success probability for the elementary link is of course 1. If we are already extremely close to this maximum value there is not much to gain by further increasing the number of modes.

This is a nice proof of concept of how our detailed simulation can produce helpful information for future experimental efforts. Of course this is only a the simplest of examples and it will be much more interesting to investigate the impact of other parameters. This brings us to our final chapter, where we want to point out possible future research enabled by our simulation.

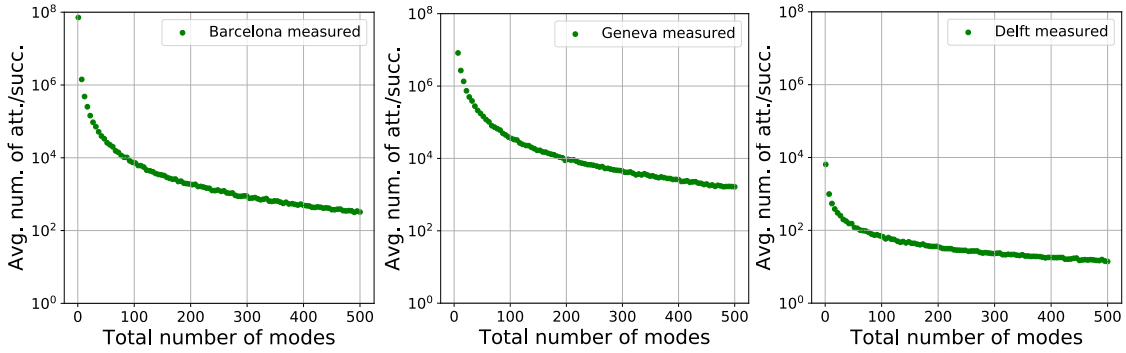

Figure 7.1: Average number of attempts per entanglement success for an elementary link of 50km. From left to right we compare the protocols from Barcelona, Geneva and Delft with current measured parameters. We see similar behavior for all the setups. Increasing the number of modes up to 100 has the most significant effect of improving the rate by several orders of magnitudes. Further increasing the number still improves the rate and no real saturation is observable for up to 500 modes. There is also a significant difference in absolute rates between the two single-click protocols (Barcelona, Geneva) and the double-click protocol (Delft).

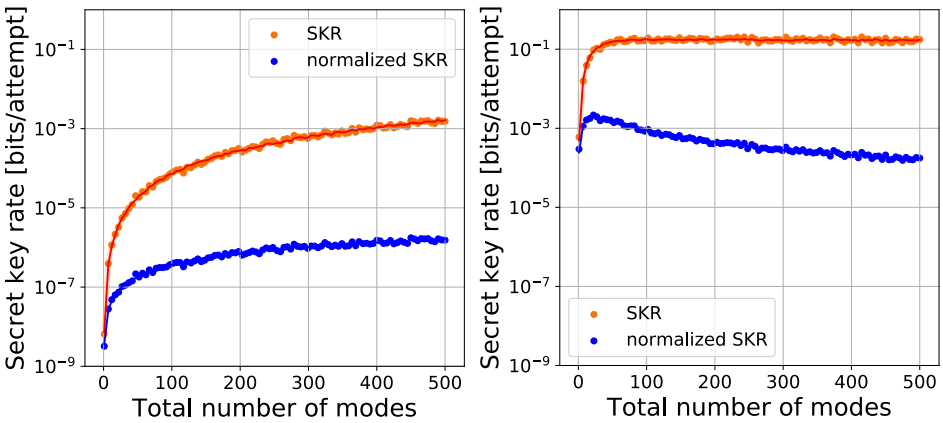

Figure 7.2: Comparison of secret key rate and secret key rate normalized by the number of modes for the Barcelona setup with measured parameters (left) and 2023 projected parameters (right) for an elementary link of length 50km. For the current parameters we see that both the raw and the normalized secret key rate are monotonously increasing for up to 500 total modes. For the highly improved, projected parameters we see a qualitatively very different behavior. After a relatively small amount of modes (< 100 modes) the raw secret key rate becomes constant. The normalized secret key rate however peaks around ~ 20 modes and then monotonously decreases. It indicates there is a parameter threshold after which increasing the number of modes further does not lead to significant improvements on the possible secret key rate. This is not unexpected since the maximum p_{link} is of course one and at some point adding more modes will just not improve this probability further.

Chapter 8

Future research

In the previous chapters we showed how different noise parameters influence the performance of repeaters protocols, how the parameters of actual physical setups perform and demonstrated how our simulation can be used for parameter exploration. It is now time to wrap up this thesis by looking at possible future research goals enabled by this work.

As briefly mentioned in Chapter 4 it would be interesting to replicate the first experimental results using an atomic ensemble based protocol published this year [63]. This would give as a first chance to validate our simulation against actual experimental data which was previously impossible.

We also already mentioned in Chapter 3, that due to the large size of our quantum states our full simulation is computationally quite heavy. The use of "Magic" significantly speeds up the simulation, however generating the sampling data still needs the full simulation. We are currently working on significantly improving the time to generate the sampling data by keeping track of the full quantum state and all probabilistic events in our simulation (e.g. which POVM outcome was successful). This way we expect to be able to recreate the full quantum state of the simulation efficiently.

With this highly optimized simulation we then aim to start exploring parameter space for different repeater protocols in much greater detail than done in Chapter 7. This way we will be able to make valuable predictions about the behavior of different protocols in large scale quantum networks. It will enable us to define lower bounds on component technologies required for a certain performance, e.g. in the form "parameters x, y of component z must be improved by $i\%$ in order to reach end-to-end fidelity F at rate R".

Additionally we plan to use a greatly reduced set of more abstract parameters in addition with sophisticated optimization methods, such as genetic algorithms, to run a full optimization that will also be able to compare different repeater technologies such as trapped ions or nitrogen-vacancy centers.

Further optimizations and interesting parameters to include in our simulation model are a detailed analysis of timing issues such as timing jitters between nodes, detector time windows and detailed investigation of different memory components such as on-demand AFC memories as mentioned in 6.2.

We also plan on investigating **hybridization**, the connection of different repeater technologies. As atomic ensembles provide high rates but do not allow for complicated quantum operations such as a complete set of quantum gates it is very interesting to investigating the possibility of e.g. connecting an atomic ensemble based repeater chain to a nitrogen-vacancy end node with full processing power.

From this brief discussion it is clear that there are many interesting research topics that are enabled by our work and we are very excited to further contribute to the development of a future Quantum Internet.

Appendix A

QIA Parameters

In this section we will first go over the different parameters submitted by the QIA groups (see Chapter 6) and how they are utilized in our simulation. Then we will list the individual parameters used to obtain the results in Chapter 6. For a detailed discussion of the implementation we refer to Chapter 3.

A.1 Source

Let us start our discussion of the parameters with the source component. The relevant parameters here are:

- **Source spectral modes**. Number of spectral modes that can be generated by the source.
- **Source spatial modes**. Number of spatial modes that can be generated by the source. Both the number of spectral and spatial modes are used to determine the total number of modes of the protocol as explained later.
- **Mean photon (pair) number**. Mean number of photon (pairs) μ emitted by the source in presence-absence (time-bin) encoding. This number is then used to determine the emission probabilities $p(n)$ for n photons (photon pairs) and create the correct quantum state as in Eq. (3.6).

A.2 Memory

The next component is the memory. Here the relevant parameters are:

- **Memory spectral modes**. Number of spectral modes that the memory can store.
- **Memory spatial modes**. Number of spatial modes that the memory can store.
- **Memory temporal modes**. Number of temporal modes that the memory can store. The number of spectral, spatial and temporal modes are used to determine the total number of modes of the protocol as explained later.
- **Maximum memory efficiency**. Maximum retrieval efficiency η_0^{AFC} of the memory as described in Eq. (2.26).
- **Memory coherence time** T_c determining the time-dependence of the memory efficiency as described in Eq. (2.26).

A.3 Detectors

We split the detectors in **midpoint** (as in the midpoint of an elementary link) and **swap** detectors as they can be potentially different. However they both have the same set of free parameters:

- **Visibility.** Visibility ν of the photons arriving at the detector. Can be different depending on whether the photons come from the source (midpoint detector) or from the memories (swap detectors). Used in the effective POVMs of the measurements as explained in Sec. 3.5.3.

- **Detection time window** of the detectors.

- **Dark count rate** of the detectors. This together with the detection time window is used to calculate the dark count probability p_{dc} used on the detector component.

- **Detector efficiency** η_d which is used to determine the probability of not detecting a photon $p = 1 - \eta_d$.

- **Number-resolving**. Boolean indicating whether the used detector can resolve photon number or is merely a threshold detector.

- **Detector mode limit**. Limit for the number of modes that the detector introduces. It is e.g. experimentally hard to develop a detector that can resolve an arbitrary number of spectral modes. This parameter only applies to the midpoint detectors as the swap operation is performed on a single mode anyway.

More details about the implementation can be found in Section 3.5.3.

A.4 Fiber

The fiber only has **attenuation** α and **initial loss probability** as free parameters. The latter is the probability that the photon created in the source gets lost when put on the fiber and captures all losses due to e.g. frequency shifting or coupling of the telecom photon.

A.5 General

In this section we describe parameters that are not specific to a component but concern the entire protocol.

- **Encoding**. The encoding of the photons used in the protocol. This determines whether the protocols is single- or double-click.

- **Total number of modes**. This is determined by taking the minimum value of modes between memory and source for each type of multiplexing and then upper-bounding it with the mode limit introduced by the midpoint detectors. For example for the Delft 'Expected 2020' parameter set the source can generate 50 spectral modes while the memory can only hold 26 and the detector limits to 10. Therefore the total number of modes is set to 10.

A.6 Parameter values

Here we just give a table with the parameters used to produce the results in Chapter 6. M2020, E2020, P2023 denote the parameter sets Measured 2020, Expected 2020 and Projected 2023 respectively. MD and SD are short for midpoint and swap detectors. The $*$ denotes that this parameter was not supplied by the group but filled in by us as an educated guess, while $**$ indicates a choice we made from a number of provided parameters.

We will start with the two single-click protocols from Geneva and Barcelona in Table A.1 and then provide the parameters for the two double-click protocols from Delft and Paris in Table A.2.

When looking at some of the values (e.g. total number of modes) it is clear that some groups have been more optimistic than others about their predictions. This makes a fair comparison difficult and it is worth noting that it is not clear how these parameters can be reached in such a short time.

It is also worth noting that one important parameter, the **source frequency**, has been omitted so far. Since we are only comparing rates in bits per attempt this is not really relevant. For completeness we would like to mention them anyway. The values provided are different quantities and thus difficult to compare. Delft provided their **rate of coincidence** of 10kHz, which is the rate of having a coincident detection of both the signal and the idler photon emitted by the source. This is not the source frequency we would use in our simulation as it already contains a number of other loss parameters such as detection efficiency and does not include the vacuum component.

Barcelona reports a rate of between 1 and 5 kHz per mW power of the pump laser. Geneva reports a rate of 20Hz but did not specify what rate that is exactly or how it was measured. Paris did not submit any number.

This shows us that in order to have a fair comparison of setups there still needs to be further communication to standardize the provided parameters, especially the source frequency.

Parameter Name	Geneva			Barcelona		
[Unit]	M2020	E2020	P2023	M2020	E2020	P2023
Encoding	presence-absence (single-click protocols)					
Source spectral modes	1			15	15	15**
Source spatial modes	1			2		
Mean photon (pair) number	0.001**	0.01**	0.01**	3e-3**	0.005**	0.05**
Memory spectral modes	1			1	30	100
Memory spatial modes	1			1	3	100
Memory temporal modes	12	50	100	33	40	40
Maximum memory efficiency	0.025	0.1	0.3	0.3	0.4	0.84
Memory coherence time [ns]	1e6	100e6	1e9**	34000	27500	27500
MD visibility	0.9*	0.9	0.95	0.9	0.95	0.95
MD detection time window [ns]	1000			300		
MD dark count rate [Hz]	0.1			10		
MD detection efficiency	0.6	0.6	0.9	0.1	0.8	0.8
MD number-resolving	False					
MD mode limit	None					
SD visibility	0.9*	0.9	0.95	0.9*	0.95*	0.95*
SD detection time window [ns]	1000			300		
SD dark count rate [Hz]	0.1			10		
SD detection efficiency	0.6	0.6	0.9	0.5	0.5	0.8
SD number resolving	False					
Fiber attenuation [dB/km]	0.16			0.25	0.25	0.17
Fiber Initial loss probability	0.9	0.8	0.8	0	0	0
Total number of modes	12	50	100	33	1200	1200

Table A.1: Parameters used for the single-click setups from Geneva and Barcelona.

Parameter Name	Delft			Paris		
[Unit]	M2020	E2020	P2023	M2020	E2020	P2023
Encoding	time-bin (double-click protocols)					
Source spectral modes	3	50	50	1	1	14
Source spatial modes	1			1	1	14
Mean photon (pair) number	0.05**			0.05*		
Memory spectral modes	26	26	50	1		
Memory spatial modes	1	1	5	2	2	14
Memory temporal modes	1			1		
Maximum memory efficiency	0.005	0.12	0.1	0.9		
Memory coherence time [ns]	1e5	5e5	1e6	1e4		
MD visibility	0.9*	0.9*	0.95	0.9*	0.9*	0.95*
MD detection time window [ns]	10			10		
MD dark count rate [Hz]	10			50		
MD detection efficiency	0.75	0.75	0.9	0.5		
MD number-resolving	False					
MD mode limit	1	10	50	None		
SD visibility	0.9*	0.9*	0.95	0.9*	0.9*	0.95 *
SD detection time window [ns]	10			10		
SD dark count rate [Hz]	10			50		
SD detection efficiency	0.75	0.75	0.9	0.5		
SD number resolving	False					
Fiber attenuation [dB/km]	0.2			0.2*		
Fiber Initial loss probability	0.03			0.03*		
Total number of modes	1	10	50	2	2	14

Table A.2: Parameters used for the double-click setups from Delft and Paris.

Bibliography

[1] F. Arute, K. Arya, R. Babbush, *et al.*, "Quantum supremacy using a programmable superconducting processor," *Nature*, vol. 574, no. 7779, pp. 505–510, Oct. 2019, ISSN: 0028-0836, 1476-4687. DOI: 10.1038/s41586-019-1666-5. [Online]. Available: http://www.nature.com/articles/s41586-019-1666-5 (visited on 02/16/2020).

[2] QuantumFlagship. (). Quantum Technology | The future is Quantum, [Online]. Available: https://qt.eu/ (visited on 02/16/2020).

[3] Horizon2020. (). What is Horizon 2020? [Online]. Available: https://ec.europa.eu/programmes/horizon2020/en/what-horizon-2020 (visited on 02/16/2020).

[4] QIA. (). Quantum Internet Alliance, [Online]. Available: http://quantum-internet.team/ (visited on 02/16/2020).

[5] qiaflagship. (). QIA - Quantum Internet Alliance, [Online]. Available: https://qt.eu/understand/projects/qia-quantum-internet-alliance/ (visited on 02/16/2020).

[6] C. H. Bennett and G. Brassard, "Quantum cryptography: Public key distribution and coin tossing," *Theoretical Computer Science*, vol. 560, pp. 7–11, Dec. 2014, ISSN: 03043975. DOI: 10.1016/j.tcs.2014.05.025. [Online]. Available: https://linkinghub.elsevier.com/retrieve/pii/S0304397514004241 (visited on 02/17/2020).

[7] A. Broadbent, J. Fitzsimons, and E. Kashefi, "Universal blind quantum computation," *2009 50th Annual IEEE Symposium on Foundations of Computer Science*, pp. 517–526, Oct. 2009. DOI: 10.1109/FOCS.2009.36. arXiv: 0807.4154. [Online]. Available: http://arxiv.org/abs/0807.4154 (visited on 02/17/2020).

[8] D. Gottesman, T. Jennewein, and S. Croke, "Longer-Baseline Telescopes Using Quantum Repeaters," *Physical Review Letters*, vol. 109, no. 7, p. 070 503, Aug. 16, 2012, ISSN: 0031-9007, 1079-7114. DOI: 10.1103/PhysRevLett.109.070503. [Online]. Available: https://link.aps.org/doi/10.1103/PhysRevLett.109.070503 (visited on 02/17/2020).

[9] T. B. Bahder, "Quantum Positioning System," Jun. 17, 2004. arXiv: quant-ph/0406126. [Online]. Available: http://arxiv.org/abs/quant-ph/0406126 (visited on 02/17/2020).

[10] D. Dieks, "Communication by EPR devices," *Physics Letters A*, vol. 92, no. 6, pp. 271–272, Nov. 1982, ISSN: 03759601. DOI: 10.1016/0375-9601(82)90084-6. [Online]. Available: https://linkinghub.elsevier.com/retrieve/pii/0375960182900846 (visited on 12/31/2019).

[11] W. K. Wootters and W. H. Zurek, "A single quantum cannot be cloned," *Nature*, vol. 299, no. 5886, pp. 802–803, Oct. 1982, ISSN: 0028-0836, 1476-4687. DOI: 10.1038/299802a0. [Online]. Available: http://www.nature.com/articles/299802a0 (visited on 12/29/2019).

[12] H.-J. Briegel, W. Dür, J. I. Cirac, and P. Zoller, "Quantum Repeaters: The Role of Imperfect Local Operations in Quantum Communication," *Physical Review Letters*, vol. 81, no. 26, pp. 5932–5935, Dec. 28, 1998, ISSN: 0031-9007, 1079-7114. DOI: 10.1103/PhysRevLett.81.5932. [Online]. Available: https://link.aps.org/doi/10.1103/PhysRevLett.81.5932 (visited on 12/29/2019).

[13] A. Dahlberg, M. Skrzypczyk, T. Coopmans, *et al.*, "A Link Layer Protocol for Quantum Networks," *Proceedings of the ACM Special Interest Group on Data Communication - SIGCOMM '19*, pp. 159–173, 2019. DOI: 10.1145/3341302.3342070. arXiv: 1903.09778. [Online]. Available: http://arxiv.org/abs/1903.09778 (visited on 12/04/2019).

[14] L.-M. Duan, M. D. Lukin, J. I. Cirac, and P. Zoller, "Long-distance quantum communication with atomic ensembles and linear optics," *Nature*, vol. 414, no. 6862, pp. 413–418, Nov. 2001, ISSN: 0028-0836, 1476-4687. DOI: 10.1038/35106500. pmid: 11719796. [Online]. Available: http://www.nature.com/articles/35106500 (visited on 12/31/2019).

[15] N. Sangouard, C. Simon, H. de Riedmatten, and N. Gisin, "Quantum repeaters based on atomic ensembles and linear optics," *Reviews of Modern Physics*, vol. 83, no. 1, pp. 33–80, Mar. 21, 2011. DOI: 10.1103/RevModPhys.83.33. pmid: 22854447. [Online]. Available: https://link.aps.org/doi/10.1103/RevModPhys.83.33 (visited on 12/16/2019).

[16] M. A. Nielsen and I. L. Chuang, *Quantum Computation and Quantum Information*, 10th anniversary ed. Cambridge ; New York: Cambridge University Press, 2010, 676 pp., ISBN: 978-1-107-00217-3.

[17] J. S. Bell, "On the Einstein Podolsky Rosen paradox," *Physics Physique Fizika*, vol. 1, no. 3, pp. 195–200, Nov. 1, 1964. DOI: 10.1103/PhysicsPhysiqueFizika.1.195. [Online]. Available: https://link.aps.org/doi/10.1103/PhysicsPhysiqueFizika.1.195 (visited on 12/30/2019).

[18] M. Żukowski, A. Zeilinger, M. A. Horne, and A. K. Ekert, ""Event-ready-detectors" Bell experiment via entanglement swapping," *Physical Review Letters*, vol. 71, no. 26, pp. 4287–4290, Dec. 27, 1993, ISSN: 0031-9007. DOI: 10.1103/PhysRevLett.71.4287. [Online]. Available: https://link.aps.org/doi/10.1103/PhysRevLett.71.4287 (visited on 12/29/2019).

[19] C. H. Bennett, G. Brassard, C. Crépeau, R. Jozsa, A. Peres, and W. K. Wootters, "Teleporting an unknown quantum state via dual classical and Einstein-Podolsky-Rosen channels," *Physical Review Letters*, vol. 70, no. 13, pp. 1895–1899, Mar. 29, 1993, ISSN: 0031-9007. DOI: 10.1103/PhysRevLett.70.1895. [Online]. Available: https://link.aps.org/doi/10.1103/PhysRevLett.70.1895 (visited on 12/29/2019).

[20] M. D. Lukin, "*Colloquium* : Trapping and manipulating photon states in atomic ensembles," *Reviews of Modern Physics*, vol. 75, no. 2, pp. 457–472, Apr. 9, 2003, ISSN: 0034-6861, 1539-0756. DOI: 10.1103/RevModPhys.75.457. [Online]. Available: https://link.aps.org/doi/10.1103/RevModPhys.75.457 (visited on 12/31/2019).

[21] C. H. Bennett, G. Brassard, S. Popescu, B. Schumacher, J. A. Smolin, and W. K. Wootters, "Purification of Noisy Entanglement and Faithful Teleportation via Noisy Channels," *Physical Review Letters*, vol. 76, no. 5, pp. 722–725, Jan. 29, 1996, ISSN: 0031-9007, 1079-7114. DOI: 10.1103/PhysRevLett.76.722. [Online]. Available: https://link.aps.org/doi/10.1103/PhysRevLett.76.722 (visited on 01/01/2020).

[22] C. Laplane, P. Jobez, J. Etesse, N. Gisin, and M. Afzelius, "Multimode and Long-Lived Quantum Correlations Between Photons and Spins in a Crystal," *Physical Review Letters*, vol. 118, no. 21, p. 210 501, May 24, 2017, ISSN: 0031-9007, 1079-7114. DOI: 10.1103/PhysRevLett.118.210501. [Online]. Available: http://link.aps.org/doi/10.1103/PhysRevLett.118.210501 (visited on 01/21/2020).

[23] M. F. Askarani, T. Lutz, M. G. Puigibert, N. Sinclair, D. Oblak, and W. Tittel, "Persistent atomic frequency comb based on Zeeman sub-levels of an erbium-doped crystal waveguide," Jul. 19, 2019. arXiv: 1907.07780 [quant-ph]. [Online]. Available: http://arxiv.org/abs/1907.07780 (visited on 01/13/2020).

[24] P. Vernaz-Gris, K. Huang, M. Cao, A. S. Sheremet, and J. Laurat, "Highly-efficient quantum memory for polarization qubits in a spatially-multiplexed cold atomic ensemble," *Nature Communications*, vol. 9, no. 1, p. 363, Dec. 2018, ISSN: 2041-1723. DOI: 10.1038/s41467-017-02775-8. [Online]. Available: http://www.nature.com/articles/s41467-017-02775-8 (visited on 02/28/2020).

[25] N. Lütkenhaus, J. Calsamiglia, and K.-A. Suominen, "Bell measurements for teleportation," *Physical Review A*, vol. 59, no. 5, pp. 3295–3300, May 1, 1999, ISSN: 1050-2947, 1094-1622. DOI: 10.1103/PhysRevA.59.3295. [Online]. Available: https://link.aps.org/doi/10.1103/PhysRevA.59.3295 (visited on 01/08/2020).

[26] L. Jiang, J. M. Taylor, and M. D. Lukin, "Fast and robust approach to long-distance quantum communication with atomic ensembles," *Physical Review A*, vol. 76, no. 1, p. 012 301, Jul. 2, 2007, ISSN: 1050-2947, 1094-1622. DOI: 10.1103/PhysRevA.76.012301. [Online]. Available: https://link.aps.org/doi/10.1103/PhysRevA.76.012301 (visited on 12/31/2019).

[27] Z.-B. Chen, B. Zhao, Y.-A. Chen, J. Schmiedmayer, and J.-W. Pan, "Fault-tolerant quantum repeater with atomic ensembles and linear optics," *Physical Review A*, vol. 76, no. 2, p. 022 329, Aug. 23, 2007, ISSN: 1050-2947, 1094-1622. DOI: 10.1103/PhysRevA.76.022329. [Online]. Available: https://link.aps.org/doi/10.1103/PhysRevA.76.022329 (visited on 12/29/2019).

[28] C. Simon, H. de Riedmatten, M. Afzelius, N. Sangouard, H. Zbinden, and N. Gisin, "Quantum Repeaters with Photon Pair Sources and Multimode Memories," *Physical Review Letters*, vol. 98, no. 19, p. 190 503, May 11, 2007, ISSN: 0031-9007, 1079-7114. DOI: 10.1103/PhysRevLett.98.190503. pmid: 17677612. [Online]. Available: https://link.aps.org/doi/10.1103/PhysRevLett.98.190503 (visited on 12/31/2019).

[29] N. Sangouard, C. Simon, J. Minář, H. Zbinden, H. de Riedmatten, and N. Gisin, "Long-distance entanglement distribution with single-photon sources," *Physical Review A*, vol. 76, no. 5, p. 050 301, Nov. 9, 2007, ISSN: 1050-2947, 1094-1622. DOI: 10.1103/PhysRevA.76.050301. [Online]. Available: https://link.aps.org/doi/10.1103/PhysRevA.76.050301 (visited on 12/29/2019).

[30] N. Sangouard, C. Simon, B. Zhao, Y.-A. Chen, H. de Riedmatten, J.-W. Pan, and N. Gisin, "Robust and efficient quantum repeaters with atomic ensembles and linear optics," *Physical Review A*, vol. 77, no. 6, p. 062 301, Jun. 2, 2008, ISSN: 1050-2947, 1094-1622. DOI: 10.1103/PhysRevA.77.062301. [Online]. Available: https://link.aps.org/doi/10.1103/PhysRevA.77.062301 (visited on 12/31/2019).

[31] M. Afzelius, C. Simon, H. de Riedmatten, and N. Gisin, "Multimode quantum memory based on atomic frequency combs," *Physical Review A*, vol. 79, no. 5, p. 052 329, May 21, 2009. DOI: 10.1103/PhysRevA.79.052329. [Online]. Available: https://link.aps.org/doi/10.1103/PhysRevA.79.052329 (visited on 12/13/2019).

[32] N. Sinclair, E. Saglamyurek, H. Mallahzadeh, *et al.*, "Spectral Multiplexing for Scalable Quantum Photonics using an Atomic Frequency Comb Quantum Memory and Feed-Forward Control," *Physical Review Letters*, vol. 113, no. 5, p. 053 603, Jul. 29, 2014. DOI: 10.1103/PhysRevLett.113.053603. [Online]. Available: https://link.aps.org/doi/10.1103/PhysRevLett.113.053603 (visited on 10/04/2019).

[33] R. Valivarthi, I. Lucio-Martinez, A. Rubenok, *et al.*, "Efficient Bell state analyzer for time-bin qubits with fast-recovery WSi superconducting single photon detectors," *Optics Express*, vol. 22, no. 20, p. 24 497, Oct. 6, 2014, ISSN: 1094-4087. DOI: 10.1364/OE.22.024497. [Online]. Available: https://www.osapublishing.org/oe/abstract.cfm?uri=oe-22-20-24497 (visited on 01/08/2020).

[34] A. Lamas-Linares, J. C. Howell, and D. Bouwmeester, "Stimulated emission of polarization-entangled photons," *Nature*, vol. 412, no. 6850, pp. 887–890, Aug. 2001, ISSN: 0028-0836, 1476-4687. DOI: 10.1038/35091014. arXiv: quant-ph/0110048. [Online]. Available: http://arxiv.org/abs/quant-ph/0110048 (visited on 02/25/2020).

[35] "Nonlinear Optics (Third Edition)," in *Nonlinear Optics (Third Edition)*, R. W. Boyd, Ed., Burlington: Academic Press, Jan. 1, 2008, pp. vii–xi, ISBN: 978-0-12-369470-6. DOI: 10.1016/B978-0-12-369470-6.00016-2. [Online]. Available: http://www.sciencedirect.com/science/article/pii/B9780123694706000162 (visited on 03/03/2020).

[36] S. Tanzilli, H. De Riedmatten, H. Tittel, H. Zbinden, P. Baldi, M. De Micheli, D. Ostrowsky, and N. Gisin, "Highly efficient photon-pair source using periodically poled lithium niobate waveguide," *Electronics Letters*, vol. 37, no. 1, pp. 26–28, Jan. 2001, ISSN: 0013-5194. DOI: 10.1049/el:20010009.

[37] J. A. Armstrong, N. Bloembergen, J. Ducuing, and P. S. Pershan, "Interactions between Light Waves in a Nonlinear Dielectric," *Physical Review*, vol. 127, no. 6, pp. 1918–1939, Sep. 15, 1962, ISSN: 0031-899X. DOI: 10.1103/PhysRev.127.1918. [Online]. Available: https://link.aps.org/doi/10.1103/PhysRev.127.1918 (visited on 03/09/2020).

[38] J. Rabbie, "Simulation Model for Atomic Ensemble based Quantum Repeaters and the Optimization of their Positioning," p. 62, 2020.

[39] K. Kowalski, V. C. Long, and K. D. Xuan, "Electromagnetically Induced Transparency," p. 15,

[40] M. Falamarzi Askarani, "Telecom-wavelength quantum memories in rare earth ion-doped materials for quantum repeaters," 2019. DOI: 10.4233/uuid:d418a98b-f2aa-4af3-b0e0-864875fcad2b. [Online]. Available: https://repository.tudelft.nl/islandora/object/uuid%3Ad418a98b-f2aa-4af3-b0e0-864875fcad2b (visited on 02/07/2020).

[41] G. Liu and B. Jacquier, Eds., *Spectroscopic Properties of Rare Earths in Optical Materials*, Springer Series in Materials Science, Berlin Heidelberg: Springer-Verlag, 2005, ISBN: 978-3-540-23886-7. DOI: 10.1007/3-540-28209-2. [Online]. Available: https://www.springer.com/gp/book/9783540238867 (visited on 02/25/2020).

[42] R. H. Dicke, "Coherence in Spontaneous Radiation Processes," *Physical Review*, vol. 93, no. 1, pp. 99–110, Jan. 1, 1954. DOI: 10.1103/PhysRev.93.99. [Online]. Available: https://link.aps.org/doi/10.1103/PhysRev.93.99 (visited on 12/13/2019).

[43] M. Afzelius and C. Simon, "Impedance-matched cavity quantum memory," *Physical Review A*, vol. 82, no. 2, p. 022 310, Aug. 11, 2010, ISSN: 1050-2947, 1094-1622. DOI: 10.1103/PhysRevA.82.022310. [Online]. Available: https://link.aps.org/doi/10.1103/PhysRevA.82.022310 (visited on 02/25/2020).

[44] A. Seri, D. Lago-Rivera, A. Lenhard, G. Corrielli, R. Osellame, M. Mazzera, and H. de Riedmatten, "Quantum Storage of Frequency-Multiplexed Heralded Single Photons," *Physical Review Letters*, vol. 123, no. 8, p. 080 502, Aug. 22, 2019, ISSN: 0031-9007, 1079-7114. DOI: 10.1103/PhysRevLett.123.080502. arXiv: 1902.06657. [Online]. Available: http://arxiv.org/abs/1902.06657 (visited on 01/13/2020).

[45] M. l. G. Puigibert, M. F. Askarani, J. H. Davidson, *et al.*, "Entanglement and non-locality between disparate solid-state quantum memories mediated by photons," May 21, 2019. arXiv: 1905.08184 [quant-ph]. [Online]. Available: http://arxiv.org/abs/1905.08184 (visited on 01/13/2020).

[46] S. Guha, H. Krovi, C. A. Fuchs, Z. Dutton, J. A. Slater, C. Simon, and W. Tittel, "Rate-loss analysis of an efficient quantum repeater architecture," *Physical Review A*, vol. 92, no. 2, p. 022 357, Aug. 31, 2015. DOI: 10.1103/PhysRevA.92.022357. [Online]. Available: https://link.aps.org/doi/10.1103/PhysRevA.92.022357 (visited on 10/04/2019).

[47] A. Dousse, J. Suffczyński, A. Beveratos, O. Krebs, A. Lemaître, I. Sagnes, J. Bloch, P. Voisin, and P. Senellart, "Ultrabright source of entangled photon pairs," *Nature*, vol. 466, no. 7303, pp. 217–220, Jul. 2010, ISSN: 0028-0836, 1476-4687. DOI: 10.1038/nature09148. [Online]. Available: http://www.nature.com/articles/nature09148 (visited on 01/26/2020).

[48] H. Krovi, S. Guha, Z. Dutton, J. A. Slater, C. Simon, and W. Tittel, "Practical Quantum Repeaters with Parametric Down-Conversion Sources," *Applied Physics B*, vol. 122, no. 3, p. 52, Mar. 2016, ISSN: 0946-2171, 1432-0649. DOI: 10.1007/s00340-015-6297-4. arXiv: 1505.03470. [Online]. Available: http://arxiv.org/abs/1505.03470 (visited on 10/04/2019).

[49] NetSquid. (). NetSquid – The Network Simulator for Quantum Information using Discrete events, [Online]. Available: https://netsquid.org/ (visited on 12/03/2019).

[50] J. O. de Filho, Z. Papp, R. Djapic, and J. Oosteveen, "Model-based Design of Self-adapting Networked Signal Processing Systems," in *2013 IEEE 7th International Conference on Self-Adaptive and Self-Organizing Systems*, Sep. 2013, pp. 41–50. DOI: 10.1109/SASO.2013.16.

[51] J. O. de Filho, T. Vogel, and J. de Gier, "Runtime Services and Tooling for Reconfiguration," in *Runtime Reconfiguration in Networked Embedded Systems: Design and Testing Practices*, ser. Internet of Things, Z. Papp and G. Exarchakos, Eds., Singapore: Springer, 2016, pp. 69–92, ISBN: 978-981-10-0715-6. DOI: 10.1007/978-981-10-0715-6_3. [Online]. Available: https://doi.org/10.1007/978-981-10-0715-6_3 (visited on 12/04/2019).

[52] C. van Leeuwen, J. de Gier, J. O. de Filho, and Z. Papp, "Model-Based Architecture Optimization for Self-Adaptive Networked Signal Processing Systems," in *2014 IEEE Eighth International Conference on Self-Adaptive and Self-Organizing Systems*, Sep. 2014, pp. 187–188. DOI: 10.1109/SASO.2014.37.

[53] ns3. (). Ns-3 Network Simulator. Library Catalog: www.nsnam.org, [Online]. Available: / (visited on 03/09/2020).

[54] NetSim. (). NetSim-Network Simulator & Emulator | Home, [Online]. Available: https://www.tetcos.com/index.html (visited on 03/09/2020).

[55] NetSquid. (). Snippets – NetSquid. Library Catalog: netsquid.org, [Online]. Available: https://netsquid.org/snippets/ (visited on 03/09/2020).

[56] H. Bechmann-Pasquinucci and N. Gisin, "Incoherent and coherent eavesdropping in the six-state protocol of quantum cryptography," *Physical Review A*, vol. 59, no. 6, pp. 4238–4248, Jun. 1, 1999, ISSN: 1050-2947, 1094-1622. DOI: 10.1103/PhysRevA.59.4238. [Online]. Available: https://link.aps.org/doi/10.1103/PhysRevA.59.4238 (visited on 03/09/2020).

[57] T. Volz, A. Reinhard, M. Winger, A. Badolato, K. J. Hennessy, E. L. Hu, and A. Imamoğlu, "Ultrafast all-optical switching by single photons," *Nature Photonics*, vol. 6, no. 9, pp. 605–609, Sep. 2012, ISSN: 1749-4885, 1749-4893. DOI: 10.1038/nphoton.2012.181. [Online]. Available: http://www.nature.com/articles/nphoton.2012.181 (visited on 02/09/2020).

[58] O. Gittsovich, N. J. Beaudry, V. Narasimhachar, R. R. Alvarez, T. Moroder, and N. Lütkenhaus, "Squashing model for detectors and applications to quantum-key-distribution protocols," *Physical Review A*, vol. 89, no. 1, p. 012 325, Jan. 23, 2014, ISSN: 1050-2947, 1094-1622. DOI: 10.1103/PhysRevA.89.012325. [Online]. Available: https://link.aps.org/doi/10.1103/PhysRevA.89.012325 (visited on 02/09/2020).

[59] S. Bravyi and A. Kitaev, "Universal Quantum Computation with ideal Clifford gates and noisy ancillas," *Physical Review A*, vol. 71, no. 2, p. 022 316, Feb. 22, 2005, ISSN: 1050-2947, 1094-1622. DOI: 10.1103/PhysRevA.71.022316. arXiv: quant-ph/0403025. [Online]. Available: http://arxiv.org/abs/quant-ph/0403025 (visited on 02/09/2020).

[60] I. L. Chuang, D. W. Leung, and Y. Yamamoto, "Bosonic quantum codes for amplitude damping," *Physical Review A*, vol. 56, no. 2, pp. 1114–1125, Aug. 1, 1997, ISSN: 1050-2947, 1094-1622. DOI: 10.1103/PhysRevA.56.1114. [Online]. Available: https://link.aps.org/doi/10.1103/PhysRevA.56.1114 (visited on 12/14/2019).

[61] C. K. Hong, Z. Y. Ou, and L. Mandel, "Measurement of subpicosecond time intervals between two photons by interference," *Physical Review Letters*, vol. 59, no. 18, pp. 2044–2046, Nov. 2, 1987. DOI: 10.1103/PhysRevLett.59.2044. [Online]. Available: https://link.aps.org/doi/10.1103/PhysRevLett.59.2044 (visited on 12/14/2019).

[62] QuAlg. (). QuAlg - A Symbolic Linear Algebra Python Package for Quantum Mechanics, [Online]. Available: https://acksld.github.io/QuAlg/ (visited on 01/26/2020).

[63] Y. Yu, F. Ma, X.-Y. Luo, *et al.*, "Entanglement of two quantum memories via fibres over dozens of kilometres," *Nature*, vol. 578, no. 7794, pp. 240–245, Feb. 2020, ISSN: 0028-0836, 1476-4687. DOI: 10.1038/s41586-020-1976-7. [Online]. Available: http://www.nature.com/articles/s41586-020-1976-7 (visited on 02/23/2020).

[64] S. Pirandola, R. Laurenza, C. Ottaviani, and L. Banchi, "Fundamental limits of repeaterless quantum communications," *Nature Communications*, vol. 8, no. 1, p. 15 043, Apr. 2017, ISSN: 2041-1723. DOI: 10.1038/ncomms15043. [Online]. Available: http://www.nature.com/articles/ncomms15043 (visited on 02/23/2020).

Declaration

Hiermit erkläre ich, die vorliegende Arbeit selbständig verfasst zu haben und keine anderen als die in der Arbeit angegebenen Quellen und Hilfsmittel benutzt zu haben.

München, den 11.03.2020

I hereby declare that I am the sole author of this master thesis and that I have not used any sources other than those listed in the bibliography and identified as references.

Munich, the 11th of March 2020

Signature _____